
Electronic Theses and Dissertations, 2004-2019

2006

Polarization-independent Liquid Crystal Devices

Yi-Hsin Lin
University of Central Florida

 Part of the [Electromagnetics and Photonics Commons](#), and the [Optics Commons](#)
Find similar works at: <https://stars.library.ucf.edu/etd>
University of Central Florida Libraries <http://library.ucf.edu>

This Doctoral Dissertation (Open Access) is brought to you for free and open access by STARS. It has been accepted for inclusion in Electronic Theses and Dissertations, 2004-2019 by an authorized administrator of STARS. For more information, please contact STARS@ucf.edu.

STARS Citation

Lin, Yi-Hsin, "Polarization-independent Liquid Crystal Devices" (2006). *Electronic Theses and Dissertations, 2004-2019*. 924.
<https://stars.library.ucf.edu/etd/924>

POLARIZATION-INDEPENDENT LIQUID CRYSTAL DEVICES

by

YI-HSIN LIN

BS in Physics, National Tsing Hua University, 1998

MS in Institute of Electro-optical Engineering, National Chiao Tung University, 2000

A dissertation submitted in partial fulfillment of the requirements
for the degree of Doctor of Philosophy
in the College of Optics and Photonics
at the University of Central Florida
Orlando, Florida

Spring Term
2006

Major Professor: Shin-Tson Wu

© 2006 Yi-Hsin Lin

ABSTRACT

Liquid crystal (LC) devices can be operated as amplitude modulators and phase modulators. LC amplitude modulation is commonly used in liquid crystal display (LCD) while phase-only modulation is useful for laser beam steering, tunable grating, prism, lens, and other photonic devices. Most LC devices are polarization dependent and require at least one polarizer. As a result, the optical efficiency is low. To enhance display brightness, a power hungry backlight has to be used leading to a high power consumption and short battery life. In a LC phase modulator, the polarization dependent property complicates the laser beam steering system. It is highly desirable to develop new operating mechanisms that are independent of the incident light polarization.

In this dissertation, we have developed eight polarization-independent liquid crystal operation principles: three of them are aimed for displays and the other five are for phase modulators. For amplitude modulations, a new polymer-dispersed liquid crystal (PDLC) and two new dye-doped LC gels are polarizer-free by combining light scattering with dye-absorption effects. In phase modulation, we explore five device concepts: PDLC and Polymer-Stabilized Cholesteric Texture (PSCT), homeotropic LC gels, thin polymer film separated double-layered structure, and double-layered LC gels. In the low voltage regime, both PDLC and PSCT have a strong light scattering. However, as the voltage exceeds a certain level, the phase modulation is scattering-free and is independent of polarization. The homeotropic LC gels do not require any biased voltage and the response time is still fast. Although the remaining phase in these devices is small, they

are still useful for micro-phonic device applications. To increase the phase change, thin polymer film separated double-layered structure is a solution. The orthogonal arrangement of top and bottom LC directors results in polarization independence. However, the response time is slow. Similarly, double-layered LC gels are not only polarization independent but also fast response due to the established polymer network.

To my Parents, Mao-Yuan Lin and Wen-Hua Ko

To my sister, Chin-Chia Lin and my brother, Young-Son Lin

To my Husband, Yung-Hsun Wu

ACKNOWLEDGMENTS

Thank my advisor, Professor Shin-Tson Wu, for his mentoring, guidance, and support during my PhD studies at the College of Optics and Photonics/CREOL/FPCE in the University of Central Florida. Without his support and help, I would not be able to have so many achievements in my research work and I can not be who I am. I would also like to express my thankfulness to my Ph.D. committee members, Prof. Nabeel A. Riza, Prof. Boris Y. Zeldovich, and Dr. Thomas X. Wu for being there for me in these four years to evaluate my candidacy, the proposal, and the dissertation. More appreciations also go to all of my colleagues and friends. Without their constant support, I can not succeed in my studies and research. Especially thank Dr. Hongwen Ren, Dr. Yung-Hsun Wu, Dr. Yun-Hsing Fan for their help on laboratory experiments, discussions, and the inspiration. I would like also thank Dr. Xiao Liang, Dr. Sebastian Gauza, Ms. Janet R. Wu, Mr. Zhibing Ge, and Ms Ying Zhou for material measurements and simulation. Besides, Prof. Jiyu Fang and Ms. Yue Zhao of department of Mechanical, Materials and Aerospace Engineering/ UCF did a great help in AFM image and useful discussions.

Moreover, thank Chi Mei Optoelectronics (Taiwan) for providing ITO glass substrates and Picvue Electronics (Taiwan) for providing empty LC cells. Especially thank Dr. Wang-Yang Li and Mr. Kun-Chou Lin for their great supports in my research work. During my graduate studies at UCF, the Defense Advanced Research Projects Agency (DARPA), the Air Force Office of Scientific Research(AFOSR), and Toppoly

(Taiwan) have been continuously providing funding resources. I sincerely thank these three organizations for their financial aid.

Finally, I want to express my sincere gratitude to my parents, Wen-Hua Ko and Mao-Yuan Lin, for their constant support; while most importantly, I want to thank my husband, Yung-Hsun Wu, for his love and encouragement on my research work to make all my achievements possible.

TABLE OF CONTENTS

| | |
|--|-------|
| LIST OF FIGURES | xiv |
| LIST OF PUBLICATIONS | xxiii |
| CHAPTER 1: INTRODUCTION..... | 1 |
| 1.1 Motivation: Liquid Crystals as Amplitude Modulators | 1 |
| 1.2 Motivation: Liquid Crystals as Phase Modulators..... | 2 |
| 1.3 Introduction of Liquid Crystal (LC) | 5 |
| 1.3.1 What is Liquid Crystal? | 5 |
| 1.3.2 Liquid crystals in Electric Fields | 6 |
| 1.4 Dual-frequency Liquid Crystals..... | 8 |
| 1.5 Polymer-dispersed Liquid Crystal (PDLC) | 9 |
| 1.6 Polymer Stabilized Cholesteric Texture (PSCT) | 10 |
| 1.7 Guest-host Liquid Crystal Displays (GH LCD)..... | 11 |
| CHAPTER 2: GENERAL PRINCIPLES OF A POLARIZATION INDEPENDENT LC DEVICES..... | 12 |
| 2.1 Natural Light..... | 12 |
| 2.2 Mechanisms for Designing a Polarization Independent LC Amplitude Modulator | 14 |
| 2.2.1 Absorption..... | 14 |
| 2.2.2 Scattering | 16 |
| 2.2.3 Reflection..... | 17 |
| 2.2.4 Combination of Different Effects | 19 |

| | |
|---|----|
| 2.3 Designing a Polarization Independent LC Phase Modulator | 20 |
| 2.3.1 Polarization Dependency and Spatial Symmetry of LC Structure..... | 21 |
| 2.3.2 Design a Polarization Independent LC Phase Modulator | 23 |
| 2.4 Conclusion | 32 |
| CHAPTER 3: POLARIZATION INDEPENDENT LIQUID CRYSTAL AMPLITUDE | |
| MODULATORS..... | 33 |
| 3.1 Polymer-dispersed liquid crystal in a 90 ⁰ twisted cell (TPDLC)..... | 33 |
| 3.1.1 Sample Preparation | 34 |
| 3.1.2 Experimental Setup..... | 34 |
| 3.1.3 Morphologies | 35 |
| 3.1.4 Electro-optical Properties..... | 36 |
| 3.1.5 Concentration Effect | 37 |
| 3.1.6 Response Time..... | 38 |
| 3.1.7 Reflective Mode TPDLC | 39 |
| 3.1.8 Reflective Dye-doped TPDLC..... | 40 |
| 3.1.9 Conclusion | 42 |
| 3.2 Surface Pinning Effect in Thin PDLCs..... | 43 |
| 3.2.1 Sample Preparation | 44 |
| 3.2.2 Surface Pinning Effect | 45 |
| 3.2.3 Thermal-induced Phase Separation of PDLC | 46 |
| 3.2.4 Dynamic Phase Separation of PDLC..... | 48 |
| 3.2.5 Cell Gap Effect | 51 |
| 3.2.6 Conclusion | 54 |

| | |
|--|----|
| 3.3 Reflective Dye-doped Dual-frequency LC Gels..... | 56 |
| 3.3.1 Operation Principle | 56 |
| 3.3.2 Sample Preparation | 58 |
| 3.3.3 Electro-optical Properties..... | 58 |
| 3.3.4 Reflectance Spectra..... | 61 |
| 3.3.5 Response Time..... | 62 |
| 3.3.6 Reflective Direct-View Displays Using a Dye-doped LC Gel | 64 |
| 3.3.7 Discussion and Conclusion | 65 |
| 3.4 Reflective Dye-doped Negative LC (NLC) gels..... | 67 |
| 3.4.1 Structure and Mechanism | 67 |
| 3.4.2 Sample Preparation | 68 |
| 3.4.3 Electro-optical Properties..... | 69 |
| 3.4.4 Response Time..... | 70 |
| 3.4.5 Reflective Dye-doped NLC gels..... | 72 |
| 3.4.6 Conclusion | 73 |
| CHAPTER 4: POLARIZATION INDEPENDENT LIQUID CRYSTAL PHASE | |
| MODULATORS..... | 74 |
| 4.1 Introduction..... | 74 |
| 4.2 Polarization Independent LC Phase Modulators Using PDLC..... | 75 |
| 4.2.1 Mechanism..... | 76 |
| 4.2.2 Sample Preparation | 77 |
| 4.2.3 Experimental Setup..... | 78 |
| 4.2.4 Electro-optical Properties..... | 78 |

| | |
|--|-----|
| 4.2.5 Phase Shift | 79 |
| 4.2.6 Response Time..... | 81 |
| 4.2.7 Application: Microlens Arrays using PDLC..... | 81 |
| 4.2.8 Discussion and Conclusion..... | 83 |
| 4.3 Polarization Independent LC Phase Modulators Using Polymer Stabilized Cholesteric Textures (PSCT) | 85 |
| 4.3.1 Mechanism..... | 85 |
| 4.3.2 Sample Preparation | 87 |
| 4.3.3 Electro-optical Properties..... | 87 |
| 4.3.4 Response Time..... | 88 |
| 4.3.5 Phase Change..... | 88 |
| 4.3.6 Application: Microlens Arrays | 91 |
| 4.3.7 Conclusion | 93 |
| 4.4 Polarization Independent LC Phase Modulators Using Homeotropic LC gels | 94 |
| 4.4.1 Mechanism..... | 94 |
| 4.4.2 Sample Preparation | 96 |
| 4.4.3 Electro-optical Properties..... | 97 |
| 4.4.4 Response Time..... | 99 |
| 4.4.5 Phase Change..... | 100 |
| 4.4.6 Conclusion | 102 |
| 4.5 Polarization Independent LC Phase Modulators Using a Thin Polymer-Separated Doubled-layered Structure | 104 |
| 4.5.1 Structure..... | 105 |

| | |
|---|-----|
| 4.5.2 Sample Preparation | 106 |
| 4.5.3 Surface Morphologies of an Anisotropic Polymer Film..... | 106 |
| 4.5.4 Experimental Setup..... | 108 |
| 4.5.5 Phase Change..... | 108 |
| 4.5.6 Discussion..... | 110 |
| 4.5.7 Conclusion | 112 |
| 4.6 Polarization Independent LC Phase Modulators Using Double-layered LC gels. | 113 |
| 4.6.1 Structure and Fabrication Process..... | 113 |
| 4.6.2 Phase Change..... | 115 |
| 4.6.3 Response Time..... | 117 |
| 4.6.4 Discussion..... | 118 |
| 4.6.5 Conclusion | 121 |
| CHAPTER 5: ANISOTROPIC POLYMER FILM | 122 |
| 5.1 Anisotropic Polymer Film..... | 122 |
| 5.1.1 Film Fabrication..... | 122 |
| 5.1.2 Surface Morphologies..... | 125 |
| 5.2 Applications: IPS-LCD Using a Glass Substrate and an Anisotropic Polymer Film | |
| | 129 |
| 5.2.1 Structure and sample preparation..... | 132 |
| 5.2.2 Images under Optical Microscope | 133 |
| 5.2.2 Experimental Setup..... | 134 |
| 5.2.3 Electro-optical properties..... | 135 |
| 5.2.4 Response Time..... | 136 |

| | |
|---|-----|
| 5.2.5 Discussion and Conclusion | 137 |
| 5.3 Hydrophobic Properties of Anisotropic Polymer Film..... | 140 |
| 5.4 Twisted Nematic Polymeric Film..... | 143 |
| CHAPTER 6: CONCLUSIONS | 146 |
| LIST OF REFERENCES | 148 |

LIST OF FIGURES

| | |
|--|----|
| Figure 1: Some applications of LC amplitude modulators. | 2 |
| Figure 2: A LC phase modulator is used as an optical phase grating. | 3 |
| Figure 3: Applications of LC phase modulators. (a) Directed energy weapon, and (b) airborne laser terminal. (http://www.raytheon.com/) | 4 |
| Figure 4: The nematic liquid crystal is an intermediate phase between crystalline phase and isotropic liquid phase. For thermotropic nematic liquid crystal, its nematic range exists between the melting and clearing temperatures..... | 5 |
| Figure 5: The chemical structure of nCB (4-cyano-4'-n-alkylbiphenyl) LC compound.... | 6 |
| Figure 6: The orientation of positive and negative LCs under an applied electric field..... | 8 |
| Figure 7: The dielectric constant as a function of frequency for a DFLC material. | 9 |
| Figure 8: The operation principle of PDLC..... | 10 |
| Figure 9: The operation principle of PSCT at (a) voltage-off state, and (b) voltage-on state. | 10 |
| Figure 10: The operation mechanism of the guest-host LCD..... | 11 |
| Figure 11: Schematic of positive dichroic dyes in a nematic liquid crystal host..... | 15 |
| Figure 12: (a) Double-layered GH LCD using a middle glass substrate, (b) similar structure but using a thin mylar film, and (c) A dashboard display using structure (a). | 16 |
| Figure 13: Schematic diagram of two scattering-type polymer stabilized liquid crystals. (a) Polymer-dispersed liquid crystals and (b) polymer network liquid crystals..... | 17 |

| | |
|---|----|
| Figure 14: The structures of cholesteric liquid crystals. (a) Planar texture, (b) focal conic texture, and (c) homeotropic texture..... | 18 |
| Figure 15: Schematic polarization independent phase modulator..... | 20 |
| Figure 16: (a) A homogeneous LC cell at voltage-off and voltage-on states. (b) The top view of the projection of the LC molecules in x-y plane at the voltage-off state..... | 22 |
| Figure 17: Spatial symmetry of the projected LC directors in x-y plane..... | 23 |
| Figure 18: Residual phase type of LC phase modulators at (a) voltage-off state and (b) voltage-on state. (c) The projected LC directors of (a) in x-y plane. (d) The projected LC directors of (b) in x-y plane | 24 |
| Figure 19: Double-layered type phase modulators. (a) Projected LC directors in x-y plane at difference voltages. (b) A doubled-layered homogeneous cell. (c) A doubled-layered π -cell. | 28 |
| Figure 20: A single TN cell as a polarization independent phase modulator. (a) The TN cell at (a) voltage-off state, (b) intermediate voltage state ($V > V_{th}$), and (c) High voltage state ($V \gg V_{th}$). | 31 |
| Figure21: Phase separation morphologies of (a) PDLC and (b) T-PDLC observed from a polarized optical microscope. NOA65:E48=30:70. Both devices have same cell gap $d \sim 8 \mu\text{m}$. The T-PDLC has a $\sim 1.5X$ smaller and more uniform droplet size than PDLC | 35 |
| Figure22: The voltage-dependent transmittance of T-PDLC (dark line) and PDLC (gray line). LC/polymer mixture: NOA65:E48=40:60; $\lambda = 633 \text{ nm}$ | 37 |
| Figure 23: Polymer concentration effect on device contrast ratio. Triangles are for the $6.5 \mu\text{m}$ T-PDLC cell and circles are for the $8 \mu\text{m}$ PDLC cell. | 38 |

Figure 24: The voltage dependent reflectance of T-PDLC (solid line; $d=6.5 \mu\text{m}$) and PDLC (dashed lines; $d=8 \mu\text{m}$). The inset shows the magnified scale for comparing the dark state. 40

Figure 25: The displayed image using a dye-doped T-PDLC reflective display. Black dye concentration: 2%, LC/polymer mixture: NOA65:E48=40:60, $d=6.7 \mu\text{m}$, and $V=20 V_{\text{rms}}$. A white paper was placed behind the bottom substrate to act as a diffusive reflector. 41

Figure 26: Phase separation morphologies of PDLC in (a) conventional cell, (b) PI cell without rubbing, (c) single-side rubbing (d) 90° -TN cell (anchoring energy $W\sim 3\times 10^{-4} \text{ J/m}^2$), (e) 45° -TN cell ($W\sim 3\times 10^{-4} \text{ J/m}^2$), (f) homogeneous cell ($W\sim 3\times 10^{-4} \text{ J/m}^2$), (g) homogeneous cell (weak rubbing, $W\sim 1\times 10^{-4} \text{ J/m}^2$), and (h) homogeneous cell with SiO_2 alignment layers ($W\sim 8\times 10^{-5} \text{ J/m}^2$) observed from a polarized optical microscope. LC/monomer mixture: 70 wt% E48 and 30 wt% NOA65. All the devices have the same cell gap $d\sim 8 \mu\text{m}$ 46

Figure 27: The dynamic phase separation morphologies of PDLC observed from a polarized optical microscope under different temperatures without UV illumination: (a) conventional PDLC cell, (b) PI without rubbing, (c) TN cell, and (d) homogeneous cell. 48

Figure 28: The dynamic phase separation morphologies of PDLC at $T=27^\circ\text{C}$ with UV exposure starting at $t=0$: (a) conventional cell without PI, and (b) PI cell without rubbing. The UV intensity is $I=60 \text{ mw/cm}^2$ 51

| | |
|--|----|
| Figure 29: The dynamic phase separation morphologies of PDLC at T=27°C with UV exposure starting at t=0: (a) TN cell, and (b) homogeneous cell. The UV intensity is I=60 mw/cm ² and cell gap d=8 μm..... | 51 |
| Figure 30: The morphologies of the homogeneous PDLC cells with various cell gaps at T=20°C observed from a polarized optical microscope. LC/monomer mixture: 70 wt% E48 and 30 wt% NOA65..... | 52 |
| Figure 31: When the cell gap is larger, the surface anchoring effect is weaker to the bulk. | 52 |
| Figure 32: PDLC in orthogonal-rubbed thin cell is polarization independent. The cell gap is 6.5 μm..... | 53 |
| Figure 33: Voltage-dependent transmittance of the 16-μm (black solid and dashed lines) and 4-μm (gray solid and dashed lines) homogeneous PDLC cells. Solid lines: the input polarization is parallel to the cell rubbing direction. Dashed lines: the input polarization is perpendicular to the rubbing direction. λ=633 nm and T=22°C. | 54 |
| Figure 34: Schematic representation of the operating principle. (a) Voltage-off state, (b) voltage-on state, and (c) voltage-on state and V ₂ > V ₁ . The PI has no rubbing treatment. | 57 |
| Figure 35 Voltage-dependent reflectance of dye-doped DF LC gel. P and C's polarizations of the incident light are orthogonal..... | 59 |
| Figure 36: Contrast ratio as a function of detector's distance from sample. | 60 |
| Figure 37: Voltage-dependent reflectance of dye-doped DF LC gel with different cell gaps. Dye and polymer concentrations are kept at 5 wt %. | 61 |

| | |
|---|----|
| Figure 38: Reflectance spectrum of dye-doped DF LC gel at 0 V_{rms} (black line) and at 20 V_{rms} (50 kHz) (gray line)..... | 62 |
| Figure 39: Measured response time of a 5- μ m dye-doped DF LC gel at $V=30V_{rms}$. The upper traces show the dual-frequency (50 kHz and 1 kHz) addressing and lower traces show the corresponding optical signals. (a) Rise time=0.55 ms and (b) decay time= 5.78 ms. $\lambda=532$ nm. | 63 |
| Figure 40: (a) Single pixel of the 5- μ m dye-doped DF LC reflective display at $V=0$ and 30 V_{rms} (50 kHz). (b) A device of the dye-doped DF LC reflective display. A diffusive reflector is laminated to the back of the bottom glass substrate. In the white segments, the ITO electrodes were etched away so that $V=0$. Cell gap=7 μ m..... | 64 |
| Figure 41: Operating principle of the dye-doped DF LC gel and dye-doped negative LC gel. (a) Voltage-off state, and (b) voltage-on state. The PI has no rubbing treatment. | 68 |
| Figure 42: The voltage-dependent reflectance of the dye-doped DF LC gel at $f=50$ kHz (gray line), and the dye-doped NLC gel at $f=1$ kHz (black line). $\lambda=532$ nm. | 70 |
| Figure 43: Response time of the dye-doped DF LC gel. | 71 |
| Figure 44: Response time of the dye-doped negative LC gel..... | 71 |
| Figure 45: Displayed images using a reflective dye-doped NLC gel. | 72 |
| Figure 46: The concept of a polarizer-free transfective GH LCD using dye-doped LC gels. | 73 |
| Figure 47: LC droplet orientations in a PDLC film at (a) $V=0$, (b) V_1 , and (c) $V_2>V_1$ | 77 |
| Figure 48: Voltage-dependent transmittance of a PDLC film. $\lambda=633$ nm and cell gap $d=22$ μ m. | 79 |

| | |
|--|----|
| Figure 49: Voltage-dependent transmittance of a PDLC cell between parallel (right ordinate) and crossed (left ordinate) polarizers. $f=1$ kHz, $\lambda=633$ nm, and cell gap $d=22$ μm . | 80 |
| Figure 50: Measured phase shift of the PDLC cell at different voltages. Cell gap $d=22\mu\text{m}$. | 81 |
| Figure 51: Microscope photos of (a) concave polymer microlens arrays, and (b) polymer/PDLC microlens arrays. | 83 |
| Figure 52: Measured CCD images of the 2D microlens arrays at different voltages: (a) $V=0$, (b) $V=70 V_{\text{rms}}$, and (c) $V=140 V_{\text{rms}}$. | 83 |
| Figure 53: The operation mechanism of PSCT at (a) $V=0$, (b) $V_1 \sim V_s$, and (c) $V_2 > V_1$. The residual phase between (b) and (c) can be used for phase modulator. | 86 |
| Figure 54: The voltage-dependant transmittance of a PSCT cell with increasing voltage (black line) and decreasing voltage (dotted line). | 88 |
| Figure 55: The voltage-dependant transmittance of a PSCT cell between crossed polarizers (black line, left ordinate) and parallel polarizers (dotted line, right ordinate). $f=1$ kHz, $\lambda=633$ nm, and cell gap $d=25$ μm . | 89 |
| Figure 56: Measured voltage-dependent phase shift of the E44 PSCT cell we prepared. Cell gap $d=25$ μm . | 90 |
| Figure 57: Measured CCD images of 2D microlens arrays at $V=0$ and $V=180 V_{\text{rms}}$. | 91 |
| Figure 58: Voltage-dependent focal length of the PSCT-based 2D microlens arrays. | 92 |
| Figure 59: Schematic diagrams of polymer and LC directors orientations of a homeotropic LC gel: (a) $V=0$, (b) $V=V_{\text{th}}$ where the LC directors reorientation starts, and (c) $V=V_s$ where the light scattering takes place. | 96 |

| | |
|--|-----|
| Figure 60: Voltage-dependent transmittance of the LC gel. $d=23\mu\text{m}$. An unpolarized He-Ne laser was used for this measurement. | 98 |
| Figure 61: Voltage-dependent transmittance of the LC gel between parallel (T_{\parallel}) and crossed (T_{\perp}) polarizers. Cell gap $d=23\mu\text{m}$, $f=1\text{ kHz}$, $\lambda=633\text{ nm}$, and $T\sim 21\text{ }^{\circ}\text{C}$ | 99 |
| Figure 62: Measured phase shift of the LC gel at different voltages. $d=23\text{ }\mu\text{m}$ and $\lambda=633\text{ nm}$ | 100 |
| Figure 63: The structure of a polarization-independent phase modulator using a thin polymer-separated double-layered structure..... | 106 |
| Figure 64: AFM images of the anisotropic polymer film surface. LC directors are aligned along the arrow. The color bars indicate the height..... | 107 |
| Figure 65: Mach-Zehnder interferometer for measuring the phase shift. M: dielectric mirror, and BS: beam splitter..... | 108 |
| Figure 66: (a) Interference patterns at various voltages and (b) intensity profiles at 0 (blue), 7 (green) and 9 V_{rms} (red). The two orthogonal LC cells are 12- μm E7 layers. $\lambda=633\text{ nm}$ from an unpolarized He-Ne laser. | 109 |
| Figure 67: Voltage-dependent phase shift of the polarization-independent LC phase modulator at $\lambda=633\text{ nm}$. Filled circles represent the measured data using our anisotropic polymeric films while open circles are the simulated results of the double-layered structure using a 0.3-mm-thick glass separator..... | 109 |
| Figure 68: A homogeneous LC gel: (a) single layer and (b) double layers..... | 114 |
| Figure 69: (a) Interference fringes of the LC gel and (b) intensity profile at different voltages. | 116 |

| | |
|--|-----|
| Figure 70: Measured phase shift of a 16- μm double-layered LC gel at different voltages. | 117 |
| Figure 71: The measured response time of the 16- μm LC gel between 0 and 100 V_{rms} bursts ($f=1$ kHz). (a) Rise time ~ 0.2 ms and (b) decay time ~ 0.5 ms at $T\sim 22$ $^{\circ}\text{C}$. The gray lines in each figure represent the applied voltage and the black lines represent the optical signals..... | 118 |
| Figure 72: (a) The compositions of liquid crystal E7. (b) The chemical structure of monomer RM257..... | 123 |
| Figure 73: Phase diagram of the E7/RM257 mixtures. All the mixtures have 1wt% IRG184 photo-initiator..... | 124 |
| Figure 74: Fabrication process of the anisotropic polymer film..... | 124 |
| Figure 75: The AFM images of (a) the rubbed PI film surface and (b) the anisotropic polymer film surface. The LC directors are aligned along the arrow. The color bars indicate the height..... | 126 |
| Figure 76: The AFM images of the anisotropic polymer film surface at different monomer concentrations. The curing temperature is 90°C . The LC directors are aligned along the arrow. The color bars indicate the height..... | 127 |
| Figure 77: The RMS roughness of the surfaces of anisotropic polymer films as a function of monomer concentration. The curing temperature is 90°C | 127 |
| Figure 78: The AFM images of the anisotropic polymer film surface at different curing temperatures. The monomer concentration is 80 wt%. The LC directors are aligned along the arrows. The color bars indicate the height..... | 129 |

| | |
|--|-----|
| Figure 79: The RMS roughness of the surfaces of anisotropic polymer films as a function of curing temperature. The monomer concentration is 80 wt%..... | 129 |
| Figure 80: The device structure and operation mechanism of an IPS LCD. (a) Voltage-off, and (b) Voltage-on. | 130 |
| Figure 81: The device structure of an IPS LC cell consisting of a top anisotropic polymeric film and a bottom ITO-glass substrate. The thickness of the top anisotropic film is 12 μm , and the cell gap is also 12 μm | 133 |
| Figure 82: Microscopic photos taken from a polarizing microscope at different voltages with crossed polarizers. (a) Our anisotropic film-glass IPS cell, and (b) the conventional IPS cell. The two black zigzags in the photos are TFT source lines. | 134 |
| Figure 83: Experimental setup for EO properties measurement of an IPS-LCD using a glass substrate and an anisotropic polymer film. | 135 |
| Figure 84: The voltage-dependent transmittance of our anisotropic-film-glass IPS cell (black line) and the conventional IPS cell (gray line)..... | 136 |
| Figure 85: The measured response time of our film-glass IPS cell. The rise time is ~ 8 ms and decay time ~ 63 ms. Cell gap $d \sim 12$ μm | 137 |
| Figure 86: The structure of contact angle measurement. | 140 |
| Figure 87: Contact angle measurement (a) 0 and (b) 200 V_{rms} . $f = 1$ kHz. The duration between 0 and 200 V_{rms} is 500 ms. | 141 |
| Figure 88: (a) The cosine of contact angle as a function of applied voltage. (b) The voltage dependent surface energy. | 142 |
| Figure 89: (a) The double layered structure using a TN anisotropic polymer film. (b) The voltage-dependent transmission. Wavelength=633nm. | 144 |

LIST OF PUBLICATIONS

1. H. Ren, Y. H. Lin, and S. T. Wu, "An adaptive lens using liquid crystal concentration redistribution", *Appl. Phys. Lett.* **88**, (April, 2006)
2. Y. H. Wu, Y. H. Lin, J. H. Lee, H. Ren, X. Nie , and S. T. Wu, "Axially-symmetric sheared polymer network liquid crystals and applications", *Mol. Cryst. Liq. Cryst.* (Accepted, 2006).
3. Y. H. Lin, H. Ren, S. Gauza, Y. H. Wu, Y. Zhou, and S. T. Wu, "High contrast and fast response polarization-independent reflective display using a dye-doped dual-frequency liquid crystal gel", *Mol. Cryst. Liq. Cryst.* (Accepted, 2006).
4. Y. H. Lin, H. Ren, S. Gauza, Y. H. Wu, Y. Zhao, J. Fang, and S. T. Wu, "IPS-LCD using a glass substrate and an anisotropic polymer film", *J. Display Technology* **2**, 21-25 (March, 2006).
5. H. Ren, Y. H. Lin, and S. T. Wu, "Flat polymeric microlens array", *Opt. Comm.* (May 1, 2006)
6. H. Ren, Y. H. Lin, and S. T. Wu, "Polarization independent phase modulators using double-layered liquid crystal gels", *Appl. Phys. Lett.* **88**, 061123 (2006).
7. Y. H. Lin, H. Ren, S. Gauza, Y. H. Wu, X. Liang, and S. T. Wu, "Reflective direct-view display using a dye-doped dual-frequency liquid crystal gel", *J. Display Technology* **1**, 230-233 (Dec. 2005).
8. J. Li, G. Baird, Y. H. Lin, H. Ren, and S. T. Wu, "Refractive index matching between liquid crystals and photopolymers", *J. SID* **13**, 1017-1026 (Dec. 2005).

9. J. H. Lee, X. Zhu, Y. H. Lin, W. K. Choi, T. C. Lin, S. C. Hsu, H. Y. Lin, and S. T. Wu, “High ambient-contrast-ratio display using tandem reflective liquid crystal display and organic light-emitting device”, *Opt. Express* **13**, 9431-9438 (2005).
10. H. Ren, Y. H. Lin, C. H. Wen, and S. T. Wu, “Polarization-independent phase modulation of a homeotropic liquid crystal gel”, *Appl. Phys. Lett.* **87**, 191106 (2005).
11. Y. H. Lin, H. Ren, Y. H. Wu, Y. Zhao, J. Fang, Z. Ge and S. T. Wu, “Polarization-independent phase modulator using a thin polymer-separated double-layered structure”, *Opt. Express* **13**, 8746-8752 (2005).
12. Y. H. Wu, J. H. Lee, Y. H. Lin, H. Ren, and S. T. Wu, “Simultaneous measurement of phase retardation and optical axis using an axially-symmetric sheared polymer network liquid crystal”, *Opt. Express* **13**, 7045-7051 (2005).
13. Y. H. Lin, H. Ren, Y. H. Fan, Y. H. Wu, and S. T. Wu, “Polarization-independent and fast-response phase modulation using a normal-mode polymer-stabilized cholesteric texture”, *J. Appl. Phys.* **98**, 043112 (August 15, 2005).
14. Y. H. Wu, X. Liang, Y. Q. Lu, Fang Du, Y. H. Lin, and S. T. Wu, “Variable optical attenuator using polymer-stabilized dual-frequency liquid crystal”, *Appl. Opt.* **44**, 4394-4397 (2005).
15. X. Nie, Y. H. Lin, T. X. Wu, H. Wang, Z. Ge, and S. T. Wu, “Polar anchoring energy measurement of vertically-aligned liquid crystal cells”, *J. Appl. Phys.* **98**, 013516 (2005).

16. Y. H. Wu, Y. H. Lin, H. Ren, X. Nie, J. H. Lee, and S. T. Wu, “Axially-symmetric sheared polymer network liquid crystals”, *Opt. Express* **13**, 4638-4644 (2005).
17. H. Ren, Y. H. Lin, Y. H. Fan, and S. T. Wu, “Polarization-independent phase modulation using a polymer-dispersed liquid crystal”, *Appl. Phys. Lett.* **86**, 141110 (2005).
18. H. W. Ren, Y. H. Lin, Y. H. Fan, and S. T. Wu, “Tunable-focus microlens arrays using nanosized polymer-dispersed liquid crystal droplets”, *Opt. Commun.*, **247**, 101-106 (2005).
19. H. Ren, J. R. Wu, Y. H. Fan, Y. H. Lin, and S. T. Wu, “Hermaphroditic liquid-crystal microlens”, *Opt. Lett.* **30**, 376-378 (2005).
20. Y. H. Lin, H. Ren, Y. H. Wu, X. Liang and S. T. Wu, “Pinning effect on the phase separation dynamics of thin polymer-dispersed liquid crystals”, *Optics Express* **13**, 468-474 (2005).
21. Y. H. Lin, H. Ren, K. H. Fang-Chiang, W. K. Choi, S. Gauza, X. Zhu and S. T. Wu, “Tunable-focus cylindrical liquid crystal lenses”, *Jpn. J. Appl. Phys.* **44**, 243-244 (2005).
22. Y. H. Wu, Y. H. Lin, Y. Q. Lu, H. Ren, Y. H. Fan, J. R. Wu and S. T. Wu, “Submillisecond response variable optical attenuator based on sheared polymer network liquid crystal”, *Opt. Express* **12**, 6377-6384 (2004).
23. H. Ren, Y. H. Lin, Y. H. Fan, and S. T. Wu, “In-plane switching liquid crystal gel for polarization independent light switch”, *J. Appl. Phys.* **96**, 3609-3611 (2004)..

24. Y. H. Fan, H. Ren, X. Liang, Y. H. Lin, and S. T. Wu, “Dual-frequency liquid crystal gels with submillisecond response time”, *Appl. Phys. Lett.* **85**, 2451-3 (2004).
25. Y. H. Lin, H. Ren, and S. T. Wu, “High Contrast Polymer-Dispersed Liquid Crystal in a 90° twisted cell”, *Appl. Phys. Lett.* **84**, 4083-4085 (2004).
26. Y. Lu, F. Du, Y. H. Lin, and S. T. Wu, “Variable optical attenuator based on polymer stabilized twisted nematic liquid crystal”, *Opt. Express* **12**, 1221-1227 (2004).
27. Y. H. Fan, Y. H. Lin, H. Ren, S. Gauza and S. T. Wu, “Fast-response and scattering-free polymer network liquid crystals for infrared light modulators”, *Appl. Phys. Lett.* **84**, 1233-1235 (2004).
28. Y. H. Lai, C. T. Yeh, Y. H. Lin, and W. H. Hung, “Adsorption and thermal decomposition of H_2S on Si(100)”, *Surf. Sci.* **519**, 150-156 (2002).

CHAPTER 1: INTRODUCTION

1.1 Motivation: Liquid Crystals as Amplitude Modulators

Liquid crystal displays (LCDs) have become the dominant display technology. Figure 1 shows some LCD applications such as high definition TV, aircraft cockpit display, notebook computer, desktop monitor, cell phone, etc. In a LCD, the LC medium functions as an electro-optic amplitude modulator. Commercial LCD devices suffer a low optical efficiency (~3%) because of the use of two polarizers. It is highly desirable to develop polarizer-free LCD devices.



Samsung 82" LCD TV



Aerospace application (CMO)



i-pod nano



Samsung



Sony Vaio



Kodak V530



Refrigerator



Figure 1: Some applications of LC amplitude modulators.

In Chapter 2, we introduce some general guidelines for designing polarization independent amplitude modulators. In Chapter 3, we demonstrate four polarization independent LC amplitude modulators using 1) twisted nematic polymer-dispersed liquid crystal (PDLC)^{11,12}, 2) dye-doped PDLC¹¹, 3) dye-doped dual-frequency liquid crystal (DFLC) gels^{13,14}, and 4) dye-doped negative LC gels¹⁵. In the twisted nematic PDLC cell, we also experimentally show how and why the surface pinning effect helps the device performance.

1.2 Motivation: Liquid Crystals as Phase Modulators

Phase-only modulation is useful for tunable grating, prism, lens, and other photonic devices. The phase modulators are important for laser beam steering^{16,17}. Mechanical beam steering requires stabilization system so that its total system is complex, power consumption is large, and cost is high for large aperture operation. On the other

hand, LC-based phase modulators have several advantages, e.g., low cost, light weight, low power consumption, no mechanical moving part, and large aperture. Besides laser beam steering, LC phase modulators can also be used in laser beam splitting, beam shaping, and adaptive focus lens, etc.

Figure 2 illustrates an optical phase grating using a LC phase modulator for laser beam steering. By controlling the applied voltage of each pixel, the optical phased array works as a phase grating. The deflection angle (θ) depends on the wavelength (λ) and grating period (Lg) as:¹⁶

$$\sin\theta = \frac{\lambda}{Lg}, \quad (1)$$

Two dimensional laser beam steering can be obtained by cascading two orthogonally oriented one-dimensional (1-D) LC phase gratings.

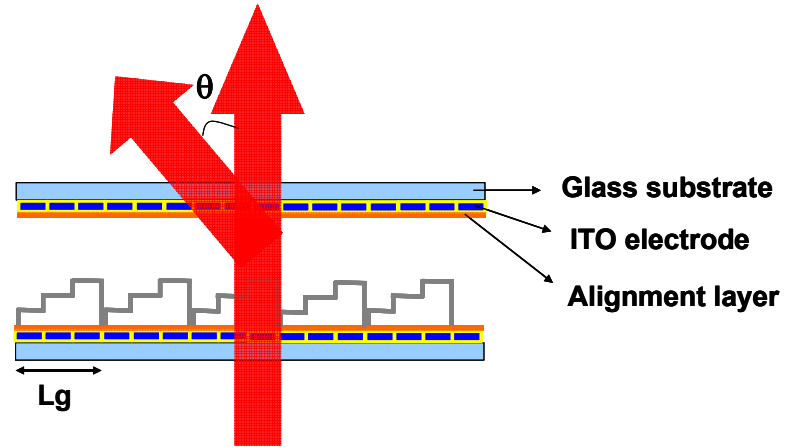


Figure 2: A LC phase modulator is used as an optical phase grating.

LC-based optical phase arrays which consist of pixilated LC phase modulators can be used for multiple target laser weapons as Figure 3(a) depicts. Such an optical phased array can also be used as part of tracking network which supports the high-data-

rate communication links. For example, Airborne Laser Terminal shown in Figure 3(b) can link between spacecrafts, aircrafts, space platforms, and the bases on the earth.

On the transmitter side, no polarizer on the phase modulator is required because the laser is usually linearly polarized. However, on the receiver side, polarizer is needed in order to assure the incoming light is in the correct polarization. The use of polarizer greatly reduces the light efficiency of the beam steering system. It is highly desirable to develop new operating mechanisms that are independent of the incident light polarization. In chapter 2, we introduce some general principles for designing a polarization-independent LC phase modulator. In chapter 4, we develop five polarization-independent liquid crystal phase modulations using 1) PDLC¹⁸, 2) PSCT¹⁹, 3) homeotropic LC gels²⁰, 4) a thin polymer-separated doubled-layered structure²¹, and 5) double-layered LC gels²².

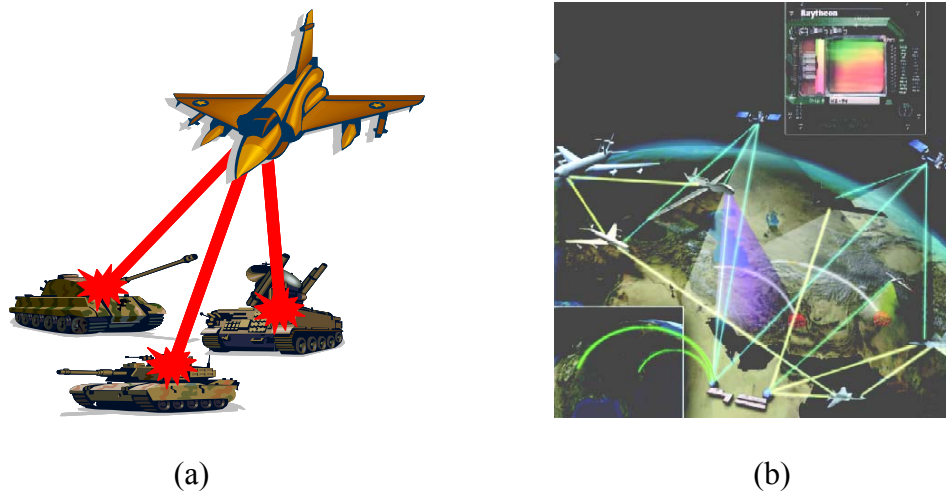


Figure 3: Applications of LC phase modulators. (a) Directed energy weapon, and (b) airborne laser terminal. (<http://www.raytheon.com/>)

1.3 Introduction of Liquid Crystal (LC)

1.3.1 What is Liquid Crystal?

Liquid crystal (LC) is a state of matter intermediate between crystalline solid and isotropic liquid¹⁻³. In Figure 4, nematic liquid crystal is used as an example. This intermediate was first observed by F. Reinitzer in 1888. When the LC molecules are sandwiched between two glass substrates with surface alignment treatment, the molecular axis tends to point along a preferred direction, called director (\mathbf{n}). The average LC director indicates that the LC orientation is not totally random even though their positions are random. Because of this directionality, LC is an anisotropic medium. Besides, LC directors can be reoriented by an electric field or magnetic field. The unique electro-optical properties of liquid crystal are widely used in many devices, such as displays, phase modulators, light shutters, etc.

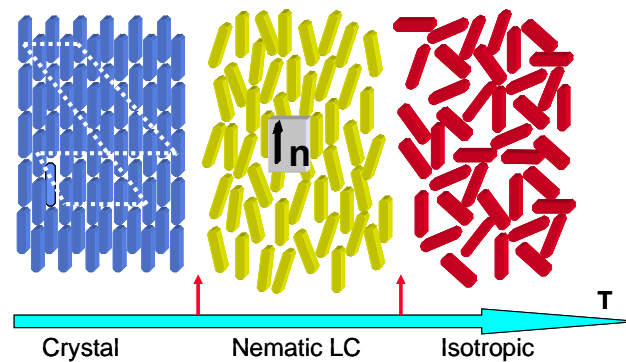


Figure 4: The nematic liquid crystal is an intermediate phase between crystalline phase and isotropic liquid phase. For thermotropic nematic liquid crystal, its nematic range exists between the melting and clearing temperatures.

A single LC compound usually possesses a narrow mesogenic phase. To widen the LC temperature range, forming eutectic mixtures is a general approach. It is quite common that a eutectic mixture might consist of a dozen single compounds. Figure 5 shows the chemical structure of a well-known LC compound: 4-cyano-4'-n-alkylbiphenyl, abbreviated as nCB, where n is the number of carbon in the flexible side chain. The width of nCB is around 5 Å and the length is about 20 Å.

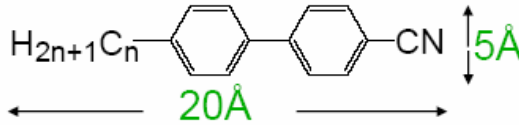


Figure 5: The chemical structure of nCB (4-cyano-4'-n-alkylbiphenyl) LC compound

1.3.2 Liquid crystals in Electric Fields

The applied electric field (\vec{E}) produces a dipole moment per unit volume which is called polarization \vec{P} . In general, the relation between \vec{E} and \vec{P} can be expressed as follows.¹⁻³

$$\vec{P} = \epsilon_0 \chi_e \vec{E}, \text{ or } \begin{pmatrix} P_x \\ P_y \\ P_z \end{pmatrix} = \epsilon_0 \begin{pmatrix} \chi_{e\perp} & 0 & 0 \\ 0 & \chi_{e\perp} & 0 \\ 0 & 0 & \chi_{e\parallel} \end{pmatrix} \begin{pmatrix} E_x \\ E_y \\ E_z \end{pmatrix} \quad (2)$$

where ϵ_0 is the permittivity of free space ($=8.85 \times 10^{-12} \text{ C}^2/\text{Nm}^2$), χ_e is the electric susceptibility, and the director is oriented along the z-axis. The unit of the electric field is

V/m. Therefore, the unit of polarization of liquid crystals is C/m² because \vec{P} is equal to the dipole moment (Cm) per unit volume (m³)

Then, the electric displacement \vec{D} can be defined by the applied electric field and polarization of LCs as:

$$\vec{D} = \epsilon_0 \vec{E} + \vec{P}, \quad (3)$$

The unit of \vec{D} is the same as \vec{P} . From Eqs. (2) and (3), \vec{D} becomes:

$$\vec{D} = \epsilon \vec{E}, \quad (4)$$

where $\epsilon = \epsilon_0 (1 + \chi_e)$ ϵ is also called the permittivity of materials.

A nematic liquid crystal has two components of permittivity, also called dielectric constants. One is along the LC director ($\epsilon_{//}$), and the other is perpendicular (ϵ_{\perp}). We can define the dielectric anisotropy of LC in permittivity as:

$$\Delta\epsilon = \epsilon_{//} - \epsilon_{\perp}. \quad (5)$$

For a LC compound or mixture, the dielectric anisotropy can be positive, zero, or negative, depending on the positions and strength of the dipole moments. A positive (or negative) LC is referred to the sign (+ or -) of the dielectric anisotropy of the LC. When $\Delta\epsilon \sim 0$, the LC is called non-polar.

When the applied electric field is not parallel to the induced dipole moments of LC molecules, it creates a net torque to reorient the LC directors along the electric field for a positive LC or perpendicular to the electric field for a negative LC in order to minimize the electrostatic energy, as shown in Figure 6.

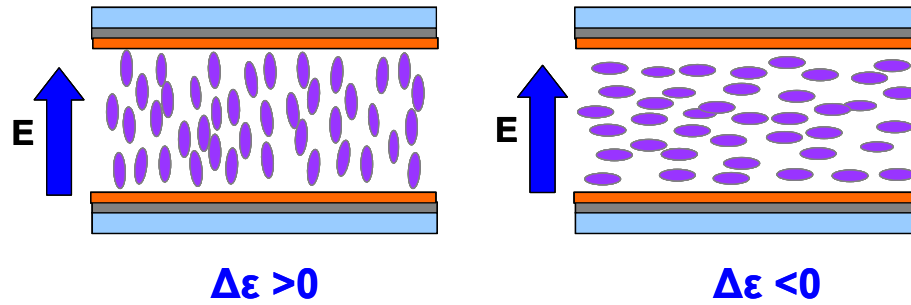


Figure 6: The orientation of positive and negative LCs under an applied electric field.

1.4 Dual-frequency Liquid Crystals

Dual-frequency liquid crystal (DFLC)³ is a special mixture of positive and negative LCs. Due to dielectric relaxation, the $\epsilon_{//}$ of the positive LC decreases as the electric field frequency increases. On the other hand, ϵ_{\perp} is independent of frequency up to the MHz range. The crossover frequency of the DF LC mixture is the frequency where $\Delta\epsilon$ changes sign. The value of the crossover frequency depends on the molecular structure and dipole properties of the DF LC compositions. To make a DF LC useful, the crossover frequency should be in the few kHz range. A typical relation between dielectric constant and frequency in DF LC is shown in Figure 7. The frequency effect of DF LC results from the longer relaxation time at higher frequency while the polarization of LC induced by the applied electric field is prompt. Besides, the molecular rotation along the short axis of LC molecules is more difficult than that along the long axis of LC. Therefore, the frequency dispersion is mainly for $\epsilon_{//}$. Figure 7 shows the typical dielectric constants of DF LC as a function of frequency.

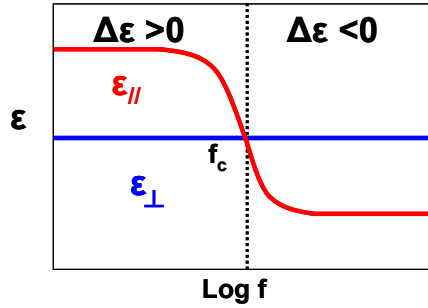


Figure 7: The dielectric constant as a function of frequency for a DFLC material.

1.5 Polymer-dispersed Liquid Crystal (PDLC)

Polymer-dispersed liquid crystals (PDLC)⁴ consist of micron-sized liquid crystal droplets that are dispersed in a solid polymer matrix as shown in Figure 8. It is similar to a sort of “Swiss cheese” polymer with liquid crystal droplets filling in the holes. The droplets are randomly distributed in the polymer matrix and their sizes are close to the visible wavelengths. The incident light is strongly scattered by the PDLC in the voltage-off state because of the refractive index mismatch and Rayleigh scattering. In the voltage-on state, the liquid crystal droplets are reoriented along the applied electric field. The LC is transparent to the incident light because the refractive index of the polymer is closed to the ordinary refractive index of the LC. Therefore, in a PDLC the incoming light could be modulated by changing the LC orientation with an electric field.

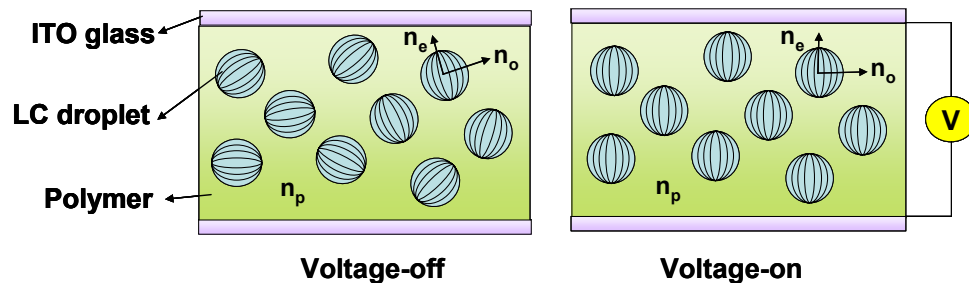


Figure 8: The operation principle of PDLC.

1.6 Polymer Stabilized Cholesteric Texture (PSCT)

Polymer stabilized cholesteric texture (PSCT)⁵ consists of cholesteric liquid crystal and some diacrylate monomer. The LC pitch length is around 0.5-5 μm . Here we only take a normal mode PSCT as an example. Without the applied electric field, the liquid crystal tends to keep the helical structure and the directions of helical axes are random. Meanwhile, the polymer network perpendicular to the glass substrates attempts to keep the LC director parallel to the polymer network. Besides the focal conic structure as show in Figure 9(a), the PSCT has multi-domain structures which are stabilized by the polymer networks. Therefore, PSCT strongly scatters the incident light at $V=0$. When the electric field is high enough to unwind the LC helical structure, the LC directors become homeotropic alignment as shown in Figure 9(b). Then, the PSCT is transparent for the incident light.

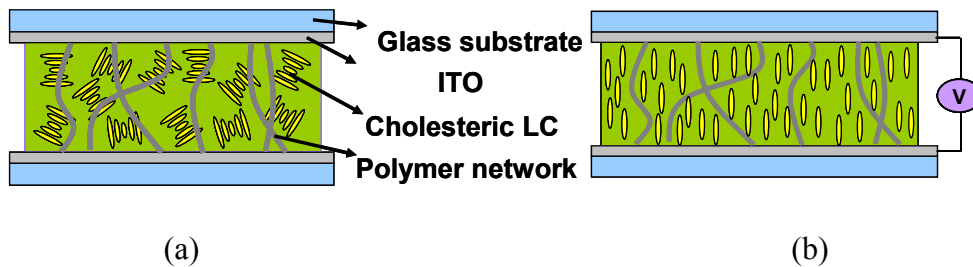


Figure 9: The operation principle of PSCT at (a) voltage-off state, and (b) voltage-on state.

1.7 Guest-host Liquid Crystal Displays (GH LCD)

The guest-host (GH) display consists of a host LC and guest dichroic dye.⁵ The orientation of dye molecules is affected by the LC alignment. The overall arrangement of the structure of GH LCD also affects the electro-optical properties of LCD, such as brightness and contrast ratio.

The operation mechanism of dichroic dye is shown in Figure 10. When the polarization (x-direction) of the incident light is parallel to the long axis of dye molecules, the light is strongly absorbed. The absorption is weak as the polarization (y-direction) of incident light is perpendicular to the long axis of dye molecules.

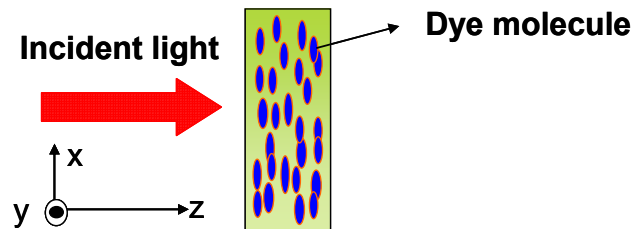


Figure 10: The operation mechanism of the guest-host LCD.

CHAPTER 2: GENERAL PRINCIPLES OF A POLARIZATION INDEPENDENT LC DEVICES

In this chapter, we introduce the general principles of polarization independent LC devices. Keeping those concepts in mind helps us to design a good polarization independent LC device no matter phase modulators or amplitude modulators. First, the nature of an unpolarized light is discussed. The polarization of an unpolarized light is random and the refractive index of a liquid crystal molecule is polarization sensitive. Better knowing the nature of light undoubtedly helps us to design a better LC device. Second, three main mechanisms for achieving polarization independent amplitude modulators are reviewed. By manipulating those mechanisms, we can design high performance polarization independent amplitude modulators. Third, the relation between polarization dependency and spatial symmetry of a LC structure is studied in section 2.3 to assist in designing polarization independent LC phase modulators. Then, several novel polarization independent phase modulators are also proposed and discussed at the end of this chapter.

2.1 Natural Light

A light wave which is an electromagnetic wave is produced by the vibration of a number of atomic emitters²³. All emitters radiating polarized wavetrains with a same frequency and then all the waves combine together to form a polarized wave. This polarized wave persists for less than 10^{-8} s. The natural light is unpolarized which means

the light is randomly polarized. The unpolarized light consists of a rapidly varying series of different polarization states. Moreover, the unpolarized light can be represented mathematically by two arbitrary, incoherent, orthogonal, linearly polarized waves with equal amplitude.

Generally speaking, a monochromatic plane and polarized wave can be expressed in complex notation as:

$$\vec{E}(\vec{r}, t) = E_0 \cdot e^{i(\omega t - \vec{k} \cdot \vec{r})} \cdot (A_{0x} \cdot e^{i\varphi_x} \cdot \hat{x} + A_{0y} \cdot e^{i\varphi_y} \cdot \hat{y}), \quad (6)$$

where E_0 , A_{0x} , A_{0y} are the amplitude of the light, $e^{i\varphi_x}$, $e^{i\varphi_y}$ are the phase terms, ω is the frequency of the wave, \vec{k} is the wave vector of the wave, t is time, and \vec{r} is the propagation distance in a vector form. The $(A_{0x} \cdot e^{i\varphi_x} \cdot \hat{x} + A_{0y} \cdot e^{i\varphi_y} \cdot \hat{y})$ term represents the polarization of the light. Moreover, A_{0x} and A_{0y} should satisfy the following relation:

$$A_{0x}^2 + A_{0y}^2 = 1, \quad (7)$$

For an unpolarized light, φ_x and φ_y are randomly varied with time.

When the wave propagates in a medium, the amplitude of the output wave changes and then this medium is operated as an amplitude modulator. Similarly, the phase terms ($e^{i(\omega t - \vec{k} \cdot \vec{r})}$, $e^{i\varphi_x}$, and $e^{i\varphi_y}$) of the output wave is modulated by the medium and then the medium is a phase modulator.

In a typical LC device, no matter amplitude or phase modulator, they require at least one polarizer. Therefore, the light efficiency is sacrificed. The main goal of this dissertation is to explore and design new polarization independent LC devices.

2.2 Mechanisms for Designing a Polarization Independent LC Amplitude Modulator

Since the refractive indices of LC molecules are polarization sensitive, how do we design a polarization insensitive LC device by just relocating the distribution of LC molecules? As a matter of fact, there are three mechanisms we can exploit for designing a polarization independent LC amplitude modulator: absorption, scattering, and reflection. Followed by a brief introduction of each mechanism, combining and re-mixing those three mechanisms are discussed. We also propose several designs at the end of this section.

2.2.1 Absorption

The dichroic dyes used in liquid crystal amplitude modulators typically have elongated and rigid molecular shape.^{4,5} When a small percentage (2-5 wt%) of dichroic dye is dissolved in a LC host, the dye molecules tend to follow the LC alignment. When the transition dipole of the dye molecules lies along the long axis of LC molecules, it is called a positive dye. Similarly, a negative dye has transition dipole perpendicular to the principal axis of the LC molecules. The absorbance of the dichroic dyes in a nematic LC host depends on the relative orientation of LC directors and polarization of the incident

light. Here we use a positive dye as an example shown in Figure 11. Light is absorbed strongly when the polarization of the incident light (x-direction in Figure 11) is parallel to the long axis of the dye molecules. The light is absorbed weakly when the polarization of incoming light (y-direction in Figure 11) is perpendicular to the long axis of the dye molecules.

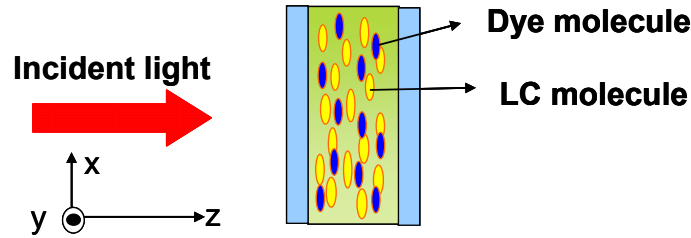


Figure 11: Schematic of positive dichroic dyes in a nematic liquid crystal host.

Basically the dye absorption is polarization dependent. To realize polarizer-free GH LCD, Dr. T Uchida proposed a double cell method in 1981.⁶ The device structure and a display panel are shown in Figure 12(a) and (c), respectively. Two homogeneous GH cells are stacked together in orthogonal directions. One polarization of an incident unpolarized light is strongly absorbed by the first GH layer because the polarization of the light is parallel to the long axis of the dye molecules. The residual polarization of the light is absorbed by the second GH layer. However, the middle glass substrate results in parallax and hinders the GH LCD from the high resolution display although the brightness is good. Later, Hasegawa et al proposed a similar structure to reduce the parallax by using a thin Mylar film^{7,8} as shown in Figure 12(b); however, the middle Mylar film can not align LC so that the contrast ratio is not very high.

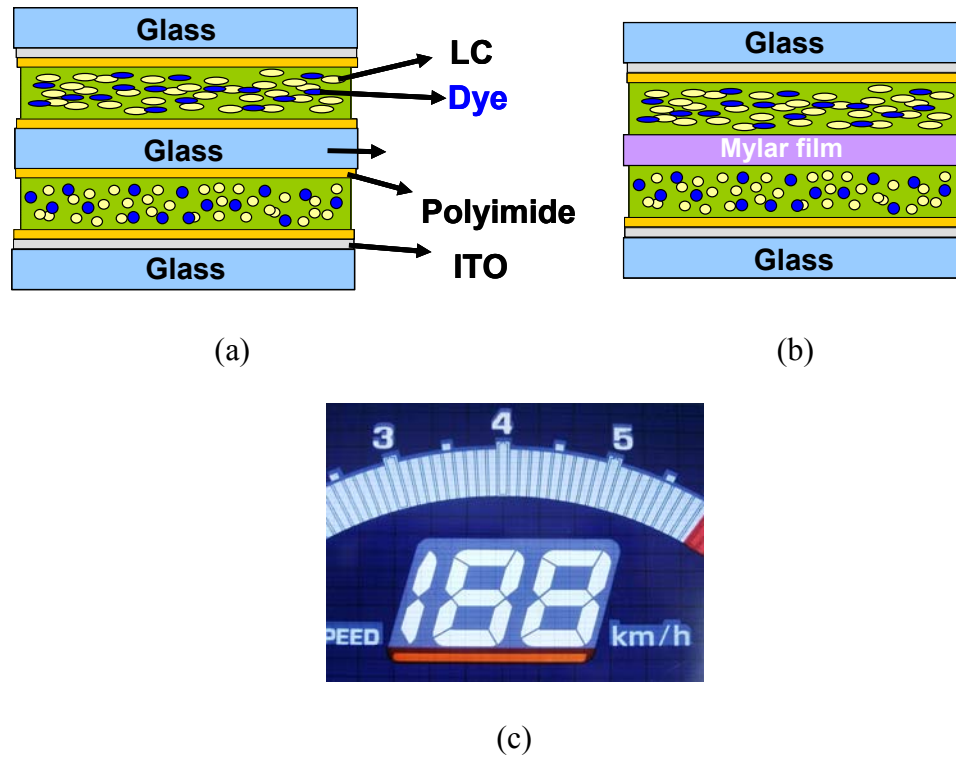


Figure 12: (a) Double-layered GH LCD using a middle glass substrate, (b) similar structure but using a thin mylar film, and (c) A dashboard display using structure (a).

2.2.2 Scattering

Scattering is another mechanism for designing a polarization independent amplitude modulator. Typically, we mix a small amount of monomer into a host liquid crystal mixture. The resulted polymer-stabilized liquid crystal strongly scatters light. The light scattering properties mainly depend on the domain size, refractive index mismatch between the LC and monomer, and LC and monomer miscibility⁴.

After phase separation process under a properly controlled experimental condition, the LC molecules are randomly dispersed in the sub-domains of polymer networks. Such

a scattering mechanism is polarization independent. When the domain size is comparable to the incident light wavelength, the light is strongly scattered by the polymer stabilized liquid crystals. As the refractive index mismatch increases, the scattering efficiency increases. Chemical solubility and different materials can form network structures or droplet structures which are called polymer network liquid crystals (or LC gels) and polymer dispersed liquid crystals, respectively, as shown in Figure 13.

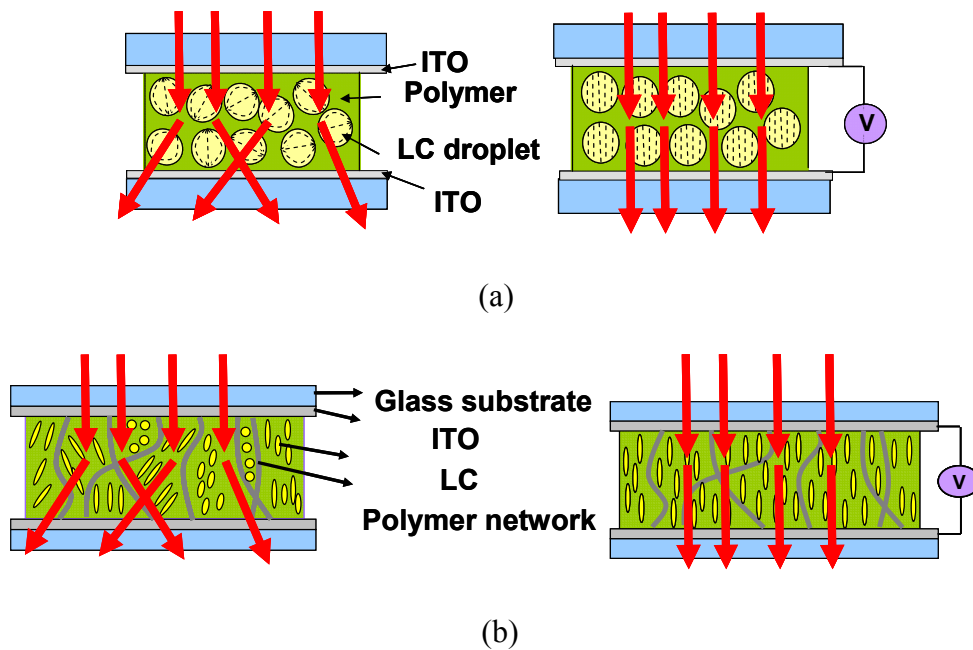
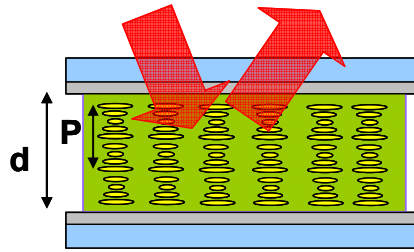


Figure 13: Schematic diagram of two scattering-type polymer stabilized liquid crystals. (a) Polymer-dispersed liquid crystals and (b) polymer network liquid crystals.

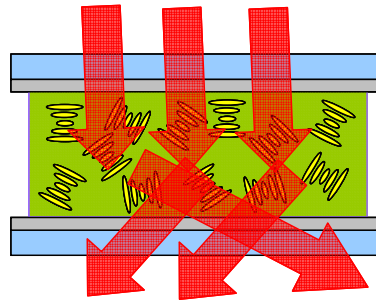
2.2.3 Reflection

The operation principle of cholesteric liquid crystals is also polarizer-free.⁵ Cholesteric liquid crystal exhibits helical structure due to the imbedded chiral center or chiral dopant. Similar to nematic liquid crystal, it has long-range orientation order but no long range position order. The structures of cholesteric liquid crystal are shown in Figure 14.

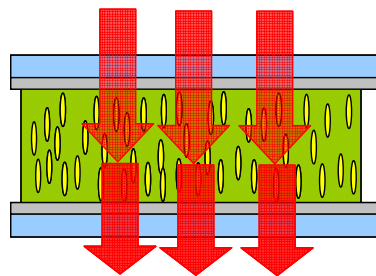
The cholesteric liquid crystal has a helical structure. In Figure 14(a), the average direction of the long axes of LC molecules is in a plane perpendicular to the helical axis. Along the helical axis, the liquid crystal directors on two near planes are twisted slightly to each other. The distance which the director rotates 2π along the helical axis is called pitch length (P).



(a)



(b)



(c)

Figure 14: The structures of cholesteric liquid crystals. (a) Planar texture, (b) focal conic texture, and (c) homeotropic texture.

In the planar texture, for the normally incident light due to the periodic structure of the refractive index, the liquid crystal exhibits Bragg reflection at the central wavelength $\lambda_0 = nP$, where n is the average refractive index of liquid crystal. The reflected bandwidth is ΔnP , where Δn is the LC birefringence. When an unpolarized white light propagates in the LC cell, the light can be decomposed into a right-handed circularly polarized light and a left-handed circularly polarized light. Only the circularly polarized light with the same handedness as the helical structure of cholesteric liquid crystals is reflected strongly due to the constructive interference of the reflected light from different layers. The other circularly polarized light with the opposite handedness is transmitted.

Incidentally, cholesteric liquid crystals have two stable states, the planar texture and the focal conic texture, at zero fields. In the focal conic texture, the direction of the helical axis is random and then it scatters the incident light. When the applied voltage is large, the helical structure is unwound and then the structure turns to a homeotropic texture as shown in Figure 14(c). Both focal conic and homeotropic states are polarization independent.

2.2.4 Combination of Different Effects

We have introduced three mechanisms for designing a polarization independent LC amplitude modulator. By manipulating them together, we can design a novel polarization independent LC amplitude modulator. For example, by combining dye absorption with the scattering effect, e.g., dye-doped LC gels, dye-doped PDLC, and dye-doped PSCT are possible designs showing a fairly good contrast ratio and reasonably fast

response time. The experimental results of the dye-doped LC gels and dye-doped PDLC are discussed in chapter 3. By combining scattering with reflection, A. Magnaldo et al has demonstrated a polymer dispersed cholesteric liquid crystal which contains cholesteric structure in the LC droplets^{9,10}. Or we can have dye-doped polymer-dispersed cholesteric liquid crystals. However, some designs may have problem about the materials or the instability of the whole structure. At last, we have discussed the guidelines for designing a polarization independent amplitude modulator.

2.3 Designing a Polarization Independent LC Phase Modulator

A piece of an isotropic glass plate is the simplest **passive** polarization independent phase modulator²⁴. The **isotropic** molecules in a glass plate are randomly positioned and distributed. The phase of an incident light is modulated but the amplitude remains unchanged. The phase difference is proportional to the optical length and the refraction index of the isotropic medium.

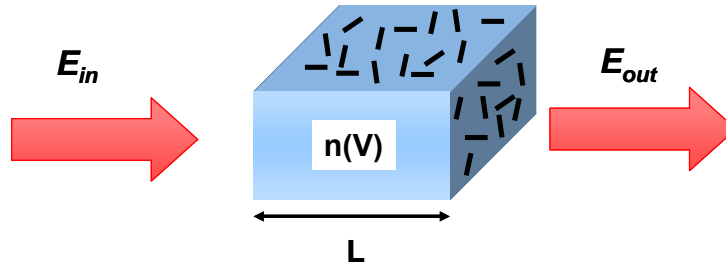


Figure 15: Schematic polarization independent phase modulator.

The concept of an electrically tunable phase modulator is illustrated in Figure 15. After traversing through the device as shown in Figure 15, the electric field of the outgoing light can be expressed as:

$$\vec{E}_{out} = \vec{E}_{in} \cdot e^{i\cdot\Psi} , \quad (8)$$

where \vec{E}_{out} and \vec{E}_{in} are the output and incident electric field of the light, and Ψ is the phase difference which can be expressed as:

$$\Psi = \frac{2\pi}{\lambda} \cdot n(V) \cdot L , \quad (9)$$

where λ is the wavelength of the light, L is the length of the medium, and $n(V)$ is the refractive index as a function of the applied voltage.

Here comes a question. Can we have a polarization independent LC phase modulator whose refractive index is electrically tunable as shown in Figure 15? The answer is positive. In the following sections, we discuss the relation between polarization and the spatial symmetry of a LC structure and then discuss how to design a polarization independent LC phase modulator. All the discussions are based on an assumption: the unpolarized light is at normal incidence.

2.3.1 Polarization Dependency and Spatial Symmetry of LC Structure

A typical LC phase modulator is homogeneous LC cell³ as shown in Figure 16(a). The homogeneous LC cell is an electrically tunable wave plate. In the voltage-off state, the refractive index of the slow axis is n_e and the refractive index of the fast axis is n_o , where n_e and n_o are the extraordinary and ordinary refractive indices of LC. In a voltage-on state, the LC directors are reoriented by the applied electric field and the refractive index of the slow axis changes. At a high voltage state, the LC cell becomes isotropic for

all the polarization of incident light. In order to operate the homogeneous cell as a phase modulator with maximal signal, the linear polarization of the incident light must be at 45 degrees with respect to the rubbing direction of the LC director. That means it is polarization dependent. From top view of LC cell, we can project all the LC directors in to x-y plane as shown in Figure 16(b). Because all the LC directors are along x-direction, the refractive index varies for different polarizations. In order to mimic an amorphous glass plate, we must rearrange the distribution of LC directors to have spatial symmetry in x-y plane as shown in Figure 17.

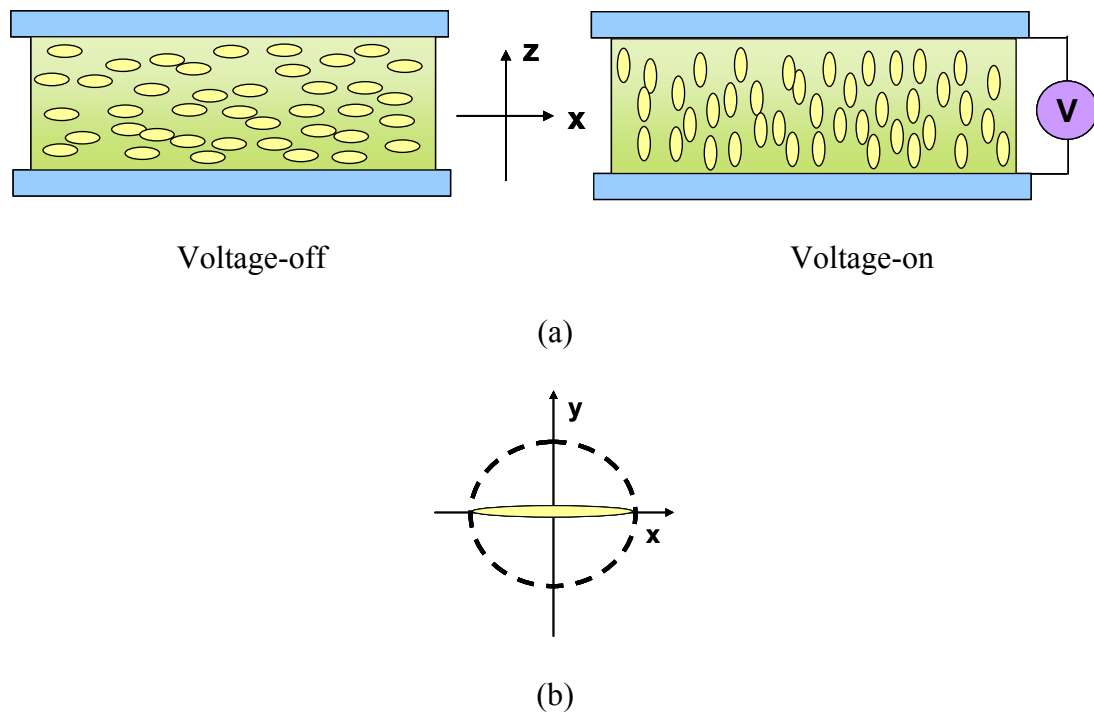


Figure 16: (a) A homogeneous LC cell at voltage-off and voltage-on states. (b) The top view of the projection of the LC molecules in x-y plane at the voltage-off state.

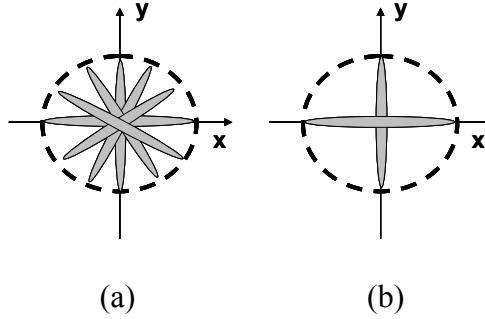


Figure 17: Spatial symmetry of the projected LC directors in x-y plane.

In Figure 17(a), all the projected LC directors are in a dotted circle with a fixed diameter in x-y plane. The average refractive index is same for all the polarization of the incident light; hence, it is polarization independent. In Figure 17(b), it is polarization independent for an unpolarized light only if we use double layered LC structure. All the polarized light can be decomposed into two linearly polarized lights in x-direction and y-direction (x-polarization and y-polarization). By using a double-layered structure, both x-polarization and y-polarization experience the same phase change and then the total polarization would not change. Therefore, it is polarization independent. We will continue to discuss this subject in next section.

2.3.2 Design a Polarization Independent LC Phase Modulator

By arranging the spatially symmetric distribution of LC directors, we can design various polarization independent LC phase modulators. Nevertheless, we need to be careful when we design a polarization independent LC phase modulator in order not to turn our designs to an amplitude modulator or polarization dependent device. Next, we discuss several examples.

A. Residual phase type of LC phase modulators

The first example is residual phase type of LC phase modulators. The name of “residual phase” is because the phase of this type for LC phase modulators is usually very small and it requires a bias voltage to keep the same tilt angle of LC directors at random positions. We extract the remaining phases from the LC cells.

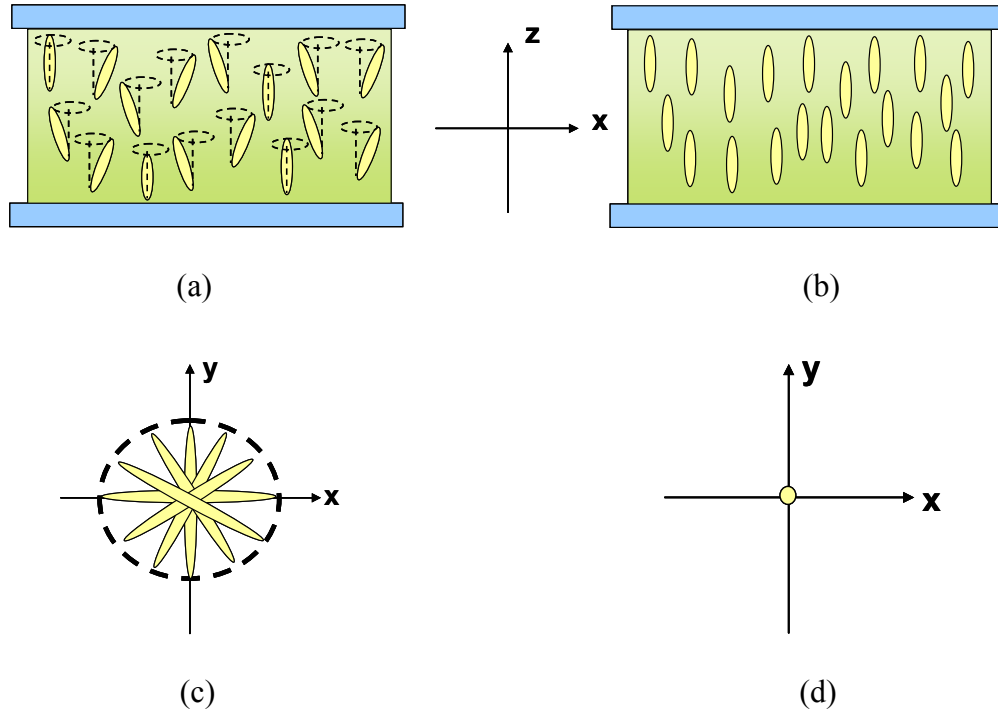


Figure 18: Residual phase type of LC phase modulators at (a) voltage-off state and (b) voltage-on state. (c) The projected LC directors of (a) in x-y plane. (d) The projected LC directors of (b) in x-y plane

The general principle of this type of LC phase modulator is as follows. In the voltage-off state we can arrange all the LC directors to have the same tilt angle at random positions as shown in (a). All the LC directors in (a) can be projected in the x-y plane as shown in (c). Assumed we have a normally unpolarized incident light which consists of randomly polarized light together and it can be expressed as:

$$\vec{E}(\vec{r}, t)_{input} \sim \sum_j [a_j \cdot (A_{0x} \cdot e^{i\varphi_x} \cdot \hat{x} + A_{0y} \cdot e^{i\varphi_y} \cdot \hat{y})_j], \quad (10)$$

where a_j is the weight factor for the j^{th} component. When an unpolarized light propagates into the LC cell, the average refractive index depending on the tilt angles is the same for all the polarizations. Hence, the output light can be expressed as:

$$\vec{E}(\vec{r}, t)_{output} \sim \sum_j [e^{-i\delta} \cdot a_j \cdot (A_{0x} \cdot e^{i\varphi_x} \cdot \hat{x} + A_{0y} \cdot e^{i\varphi_y} \cdot \hat{y})_j], \quad (11)$$

where phase shift (δ) depending on wavelength (λ), cell gap (d) and average refractive index (n_{ave}) can be expressed as:

$$\delta = \frac{2\pi}{\lambda} \cdot n_{ave} \cdot d, \quad (12)$$

Then, we rearrange Eq.(11). Eq.(11) becomes:

$$\vec{E}(\vec{r}, t)_{output} \sim e^{-i\delta} \cdot \sum_j [a_j \cdot (A_{0x} \cdot e^{i\varphi_x} \cdot \hat{x} + A_{0y} \cdot e^{i\varphi_y} \cdot \hat{y})_j], \quad (13)$$

Therefore, it is polarization independent.

Such an average refractive index ($n_{ave}(\theta)$) depends on the tilt angle (θ) and ordinary refractive index (n_o) of the LC as:

$$n_{ave}(\theta) = \frac{n_{eff}(\theta) + n_o}{2}, \quad (14)$$

where the effective refractive index $n_{eff}(\theta)$ has following expression:

$$n_{eff}(\theta) = \left[\frac{\cos^2 \theta}{n_o^2} + \frac{\sin^2 \theta}{n_e^2} \right]^{-1/2}. \quad (15)$$

The tilt angle is the angle between the LC director and the surface normal of the substrates. When the applied voltage further increases, the tilt angle of all LC directors decreases as well; in other words, the distribution of the projected LC directors is similar to (c), but the radius of the circle decreases. When the voltage is high enough to fully reorient the LC directors along the electric field direction as shown in (b), the distribution of the projected LC director in the x-y plane, as shown in (d), remains spatial symmetric similar to (c). It is still polarization independent.

The total phase shift between high voltage and zero voltage can be expressed as:

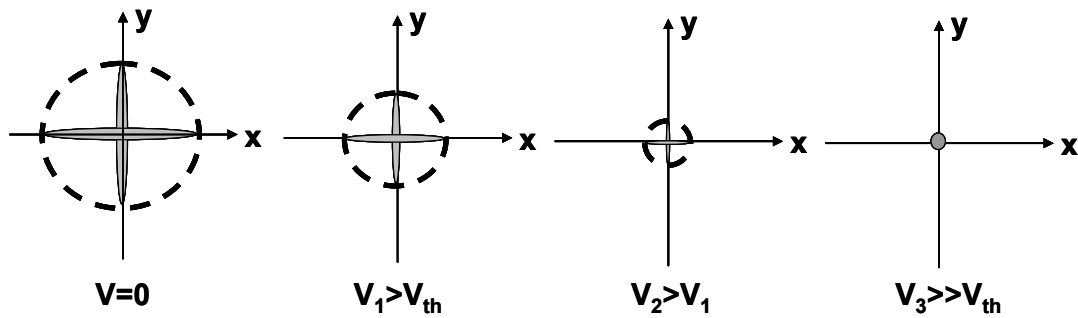
$$\delta(V \gg V_{th}, 0) = \frac{2\pi}{\lambda} \cdot (n_{ave}(\theta) - n_o) \cdot d . \quad (16)$$

The concept of residual phase type phase modulators is simple. However, to realize such a device in experiment is not so easy. We have successfully demonstrated several residual phase types of polarization independent LC phase modulators, such as PDLC, PSCT and homeotropic LC gels which are discussed in chapter 4. As we mention in previous sections, PDLC, PSCT and LC gels are scattering type amplitude modulations. However, they can be pure phase modulators when the voltage is larger than a saturated voltage. The details are discussed in chapter 4.

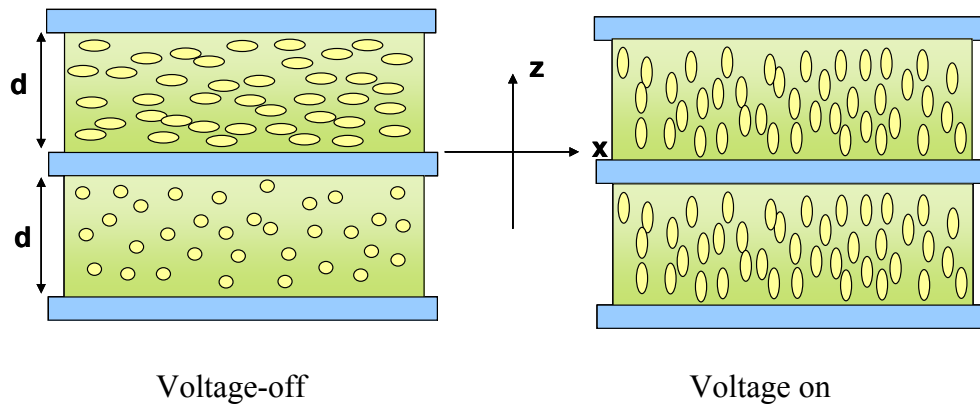
B. Double-layered type phase modulators

Another design to achieve a polarization independent phase modulator is to stack two layers together. Two identical LC cells, such as two homogeneous cells shown in Figure 19(b) or π -cell shown in Figure 19(c), are stacked together in orthogonal directions. The projected LC directions in x-y plane at different voltages are illustrated in Figure 19(a). An unpolarized light can be decomposed into x- and y- linear polarizations.

After propagating through the two LC layers, both x- and y- polarized lights experience the same phase change, Therefore the output polarization remains the same. The radius of the circle of projected LC directors decreases with applied voltage as shown in Figure 19(a). Besides the projected LC directors keep in x- or y- directors. It is polarization independent at all voltage levels.



(a)



(b)

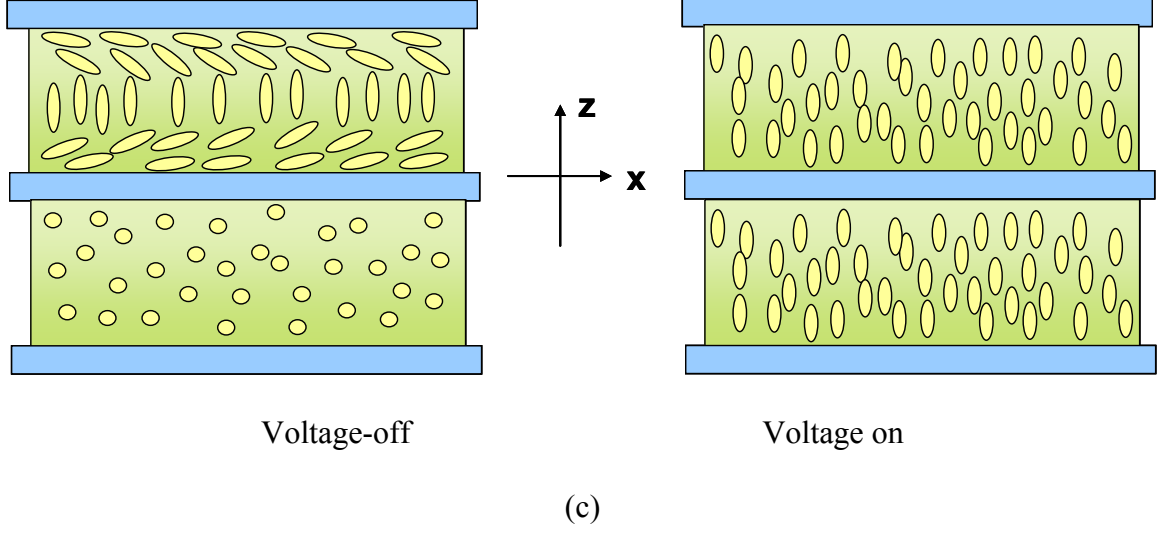


Figure 19: Double-layered type phase modulators. (a) Projected LC directors in x-y plane at difference voltages. (b) A doubled-layered homogeneous cell. (c) A doubled-layered π -cell.

We can prove the double-layered LC cells are polarization independent. Let us take double-layered homogeneous cells as an example as shown in Figure 19(b). The polarization-independent mechanism of the double-layered LC device can be proven as follows. Let us assume the normal incident unpolarized light can be expressed in Eq. (10). After propagating through the LC modulator at 0 V_{rms} , the output light can be expressed as:

$$\vec{E}(\vec{r}, t)_{\text{output}} \sim \sum_j [a_j \cdot (e^{-i\delta_1} \cdot E_{0x} \cdot e^{i\varphi_x} \cdot \hat{x} + e^{-i\delta_2} \cdot E_{0y} \cdot e^{i\varphi_y} \cdot \hat{y})]_j, \quad (17)$$

Any polarized light can be decomposed as x- and y- linearly polarized light. Each eigen mode experience some phase shift which depends on δ_1 and δ_2 . When δ_1 equals to δ_2 ($\delta_1 = \delta_2 = \delta$), Eq.(17) can be expressed as:

$$\vec{E}(\vec{r}, t)_{output} \sim e^{-i\delta} \cdot \sum_j [a_j \cdot (E_{0x} \cdot e^{i\varphi_x} \cdot \hat{x} + E_{0y} \cdot e^{i\varphi_y} \cdot \hat{y})]_j, \quad (18)$$

Therefore, it is polarization independent. When applied voltage is larger than threshold voltage, the distribution of the projected LC directors remains the same with smaller radius. Hence, it is still polarization independent when we applied voltage on the LC modulators.

When the light traverses through the LC cell (with $V=0$), the total accumulated phases of the x component and y components are $e^{i\kappa \cdot (n_e + n_o) \cdot d}$ and $e^{i\kappa \cdot (n_e + n_o) \cdot d}$, respectively, where the placement of the indices has been ordered to reflect the sequence of materials traversed from top to bottom, κ is the wave vector in the vacuum, d is the cell gap of each layer, and n_e and n_o are the extraordinary and ordinary refractive indices of the LC. The output electric field of the light becomes:

$$\vec{E}(\vec{r}, t)_{output} \sim e^{i\kappa \cdot (n_e + n_o) \cdot d} \cdot \sum_j [a_j \cdot (E_{0x} \cdot e^{i\varphi_x} \cdot \hat{x} + E_{0y} \cdot e^{i\varphi_y} \cdot \hat{y})]_j, \quad (19)$$

With an applied voltage, the total accumulated phases of the x - and y - components become $e^{i\kappa \cdot n_{eff}(\theta, \psi) \cdot d}$ and $e^{i\kappa \cdot n_{eff}(\theta, \frac{\pi}{2} + \psi) \cdot d}$, respectively, where $n_{eff}(\theta, \psi)$ is the effective refractive index of the LC, and θ and ψ respectively represent the tilt angle and the twist angle of the LC directors.

Therefore, the electric field of the outgoing light becomes:

$$\vec{E}(\vec{r}, t)_{output} \sim e^{i\kappa \cdot (n_{eff}(\theta, \psi) + n_{eff}(\theta, \frac{\pi}{2} + \psi)) \cdot d} \cdot \sum_j [a_j \cdot (E_{0x} \cdot e^{i\varphi_x} \cdot \hat{x} + E_{0y} \cdot e^{i\varphi_y} \cdot \hat{y})]_j \quad (20)$$

From Eqs (19) and (20), the polarization of the output electric field remains the same at a given applied voltage. Therefore, our LC device is polarization-independent in all different voltage states. The phase change increases with increasing voltage. The total phase change between $V=0$ and a voltage V is:

$$\delta = \frac{2\pi}{\lambda} (n_{eff}(\theta, \psi) + n_{eff}(\theta, \frac{\pi}{2} + \psi) - n_e - n_o) \cdot d, \quad (21)$$

Similarly, we can use double-layered π -cell as shown in Figure 19(c). The π cell means the rubbing directions of two alignment layers are parallel to each other. The response time of the double-layered π -cell is faster than that of a double-layered homogeneous cell because of the flow effect. However, it requires a non-zero bias voltage to turn the π -cell from splay to bend mode. Therefore, the phase change is greatly sacrificed compared to the phase change in a double-layered homogeneous cell.

C. Single twist nematic (TN) cell as a phase modulator

A single TN cell can also be used as a polarization independent phase modulator. The structure of a TN cell is plotted in Figure 20(a). The main operation principle is waveguiding effect or polarization rotation effect^{2,3,5}. At 0 V_{rms} , the polarization of an incident light propagates in a TN cell along the direction of the twisted axis. This is not a phase modulation. The middle layer of LC directors is reoriented first with increasing voltage. When the applied voltage is slightly above the Freedericksz transition threshold, some bulk LC directors are reoriented along the electric field direction and several layers near the boundaries are anchored by the alignment layers, as shown in Figure 20(b). As the voltage further increases, almost all the LC directors are along the electric field as

Figure 20(c) shows. By switching between the states depicted in Figure 20(b) and Figure 20(c), the TN cell works as a phase modulator. Similar to the double-layered type phase modulator, the two orthogonal LC directors are separated by the vertically aligned bulk directors. Therefore, it is polarization independent.^{52,53} The operation voltage of such a TN cell is low. However, the phase change is relatively small because the bulk LC directors make little contribution. This residual phase is not too sensitive to the cell gap.

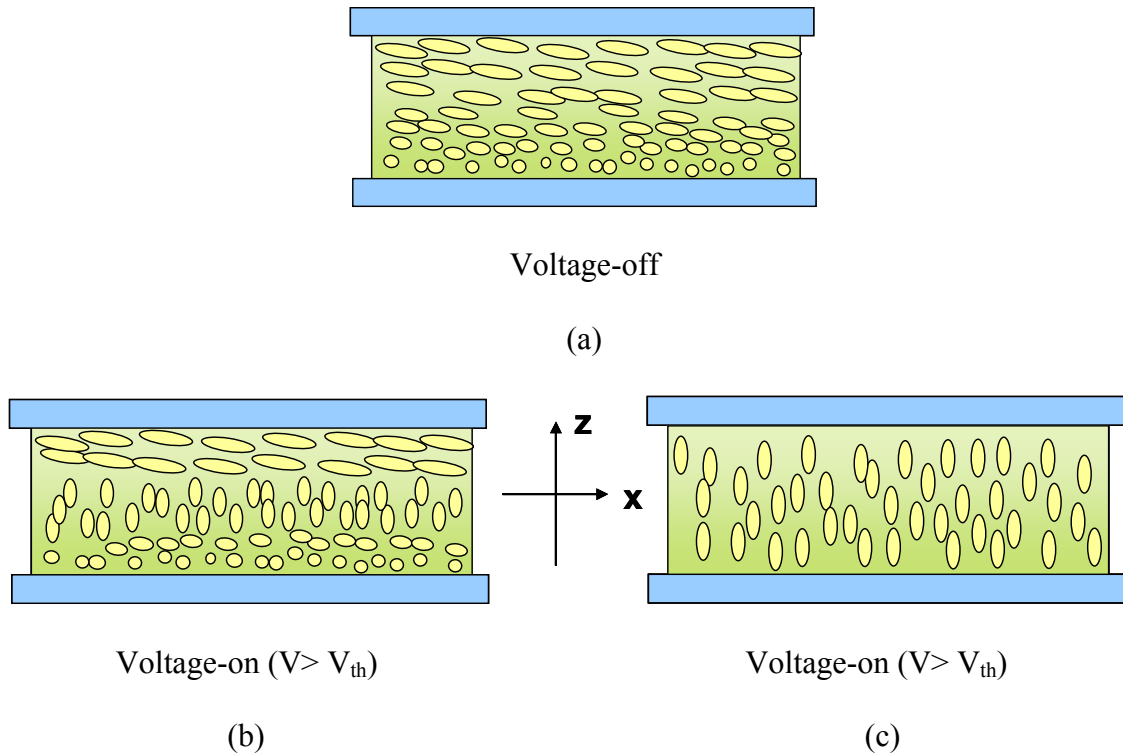


Figure 20: A single TN cell as a polarization independent phase modulator. (a) The TN cell at (a) voltage-off state, (b) intermediate voltage state ($V > V_{th}$), and (c) High voltage state ($V \gg V_{th}$).

D. Others

Another structure which also meets the spatial symmetric condition is cholesteric LC. For a cholesteric LC, the focal conic state is unavoidable. The property of polarization independence is destroyed once the twist properties are not perfect.

Moreover, the pitch of cholesteric LC has to be small in order to behave as a polarization independent phase modulator for a visible unpolarized light. Under such a circumstance, the whole cholesteric structure is unstable because the pitch is much smaller than the cell gap.

2.4 Conclusion

In this chapter, we introduce some basic and general principles to design a polarization independent LC amplitude modulator and a polarization independent LC phase modulator. Several examples are given in this chapter. In the following chapters, we focus on demonstrating polarization independent LC amplitude modulators and phase modulators in detail based on our design principles.

CHAPTER 3: POLARIZATION INDEPENDENT LIQUID CRYSTAL AMPLITUDE MODULATORS

3.1 Polymer-dispersed liquid crystal in a 90° twisted cell (TPDLC)

Polymer-dispersed liquid crystal (PDLC) which does not require a polarizer is a useful electro-optic material for displays²⁵⁻²⁶, light switches²⁷⁻³², and tunable-focus lens³³. For displays, the polarizer-free PDLC has a higher transmittance and wider viewing angle than the conventional twisted-nematic (TN) LCD. However, the LC molecules inside the droplets have many contact surfaces with polymer matrix, thus, the PDLC operating voltage is relatively high (~ 5 Vrms/ μm). Reducing cell gap or polymer concentration would lower the operating voltage; however, the contrast ratio is reduced accordingly. It is important to develop a low voltage PDLC while maintaining high contrast ratio.

In this section, we demonstrate a polymer-dispersed liquid crystal confined in a 90° twisted cell (abbreviated as T-PDLC) which exhibits a higher contrast ratio than a conventional PDLC. Unlike the traditional PDLC cell, our polyimide-buffed substrates are rubbed in orthogonal directions, similar to a 90° twisted nematic cell. Due to surface pinning effect in a thin cell, the T-PDLC not only preserves the advantage of polarization independence but also exhibits a higher light scattering efficiency.

3.1.1 Sample Preparation

We mixed UV-curable monomer NOA65 in a nematic LC host (E48, $\Delta n=0.231$ at $\lambda=589$ nm). The concentration of NOA65 is in the 15%–50% range. The LC/monomer mixture was injected into an empty 90° twisted cell in the isotropic state. The pretilt angle of the LC cell is $\sim 3^\circ$ and the cell gaps are $d=6.5$ and $8 \mu\text{m}$. For comparison, a conventional PDLC cell, i.e., the indium-tin-oxide (ITO) glass substrates without alignment layer, was also prepared under the same conditions ($d=8 \mu\text{m}$). In our experiments, the UV exposure intensity is $I=60 \text{ mW/cm}^2$ and curing time for both cells is 15 min at $T=20^\circ\text{C}$.

3.1.2 Experimental Setup

The electro-optic properties of the PDLC and T-PDLC cells were studied by measuring the transmittance of an unpolarized He–Ne laser beam ($\lambda=633$ nm) at normal incidence. The photodiode detector was placed at ~ 20 cm behind the sample; the corresponding collection angle is $\pm 1^\circ$. The voltage dependent transmittance curves were recorded by the LabVIEW data acquisition system. The response time was measured using a digital phosphor oscilloscope.

3.1.3 Morphologies

Figure21 (a) and (b) show the morphologies of the $8\mu\text{m}$ PDLC and T-PDLC cells, respectively, observed from a polarized optical microscope in the voltage-off state. The polymer concentration (c) is 30% for both cells. From Figure21 (a) and 1(b), we find that the liquid crystal droplets in the T-PDLC cell are smaller and more uniformly distributed than those in the PDLC cell. In the voltage-off state, these oriented droplets nearby the surface alignment layers enhance the light scattering efficiency because of the enlarged refractive index mismatch between the LC droplets and polymer matrix. Therefore, to achieve the same light scattering level the required T-PDLC layer is thinner than that of a PDLC.

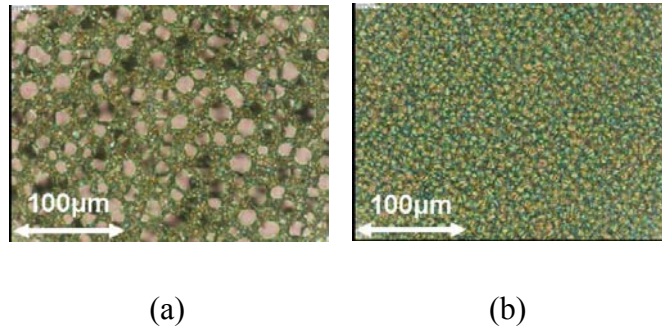


Figure21: Phase separation morphologies of (a) PDLC and (b) T-PDLC observed from a polarized optical microscope. NOA65:E48=30:70. Both devices have same cell gap $d\sim 8\mu\text{m}$. The T-PDLC has a $\sim 1.5X$ smaller and more uniform droplet size than PDLC

The physical mechanism responsible for the observed smaller droplets and more uniform size distribution in T-PDLC, as shown in Figure21 (b), is believed to originate from the surface pinning effect of the buffed polyimide surfaces. The strong surface pinning energy prevents LC droplets from growing and aggregating with the surrounding droplets during phase separation process. As a result, T-PDLC exhibits a smaller droplet

and more uniform droplet distribution than PDLC under the same polymer concentration and UV exposure conditions. The better droplet uniformity helps to enhance light scattering efficiency when the droplet size is comparable to the wavelength. In Figure21(b), the droplet size is $\sim 2 \mu\text{m}$. A 6-7 μm cell gap would contain roughly 3 droplets in each cross-section.

3.1.4 Electro-optical Properties

To evaluate the contrast ratios of the T-PDLC and PDLC cells, we measured their voltage-dependent transmittance. To calibrate the substrate reflection losses, the transmittance of a homogeneous cell filled with E48 LC mixture is defined as unity. Figure22 compares the voltage dependent transmittance of an 8- μm PDLC (gray line) and a 6.5- μm T-PDLC (dark line) cells at the same polymer concentration ($c=40\%$). The T-PDLC cell has a better dark state at $V=0$ and slightly higher transmittance in the voltage-on state than PDLC. Thus, T-PDLC exhibits a higher contrast ratio than the PDLC even though its cell gap is thinner than that of PDLC. To understand this phenomenon, we need to consider the surface alignment effect.

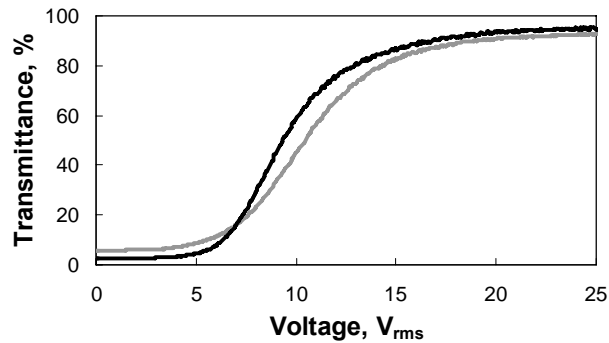


Figure22: The voltage-dependent transmittance of T-PDLC (dark line) and PDLC (gray line). LC/polymer mixture: NOA65:E48=40:60; $\lambda=633$ nm.

In a T-PDLC, the LC molecules inside the droplets near the substrates present orthogonal orientation. In the bulk, the LC droplets are randomly distributed. Therefore, its light scattering behavior in the voltage-off state is also independent of polarization, similar to a PDLC. In the low voltage regime, the T-PDLC cell exhibits a better dark state than PDLC, as shown in Figure22. The saturation voltage of both cells occurs at ~ 20 V_{rms}. Thus, we compare the contrast ratio at $V=20$ V_{rms}, i.e. $CR=T(V=20)/T(V=0)$. From Figure22, T-PDLC exhibits a higher contrast ratio than PDLC.

3.1.5 Concentration Effect

In addition to surface alignment, polymer concentration also plays an important role in affecting the device contrast ratio. We have varied the polymer concentration from 15% to 50%. In both T-PDLC and PDLC cells, the droplet size decreases as the polymer concentration increases. In the same polymer concentration, the droplet size of T-PDLC is roughly $\sim 1.5X$ smaller than that of PDLC. Therefore, the optimal polymer concentration for maximizing light scattering (i.e. droplet size is comparable to the laser wavelength) for T-PDLC and PDLC is different. For T-PDLC, the optimal polymer concentration would be lower than that for PDLC.

Figure 23 shows the polymer concentration dependent contrast ratio (measured at $V=20$ V_{rms}) for T-PDLC (triangles) and PDLC (circles). From Figure 23, as the polymer concentration increases, the contrast ratios for both T-PDLC and PDLC cells increase

almost linearly but at different slopes. For the 6.5- μm T-PDLC, the optimal polymer concentration occurs at $c \sim 40\%$ where the contrast ratio reaches $\sim 35:1$. At $c=50\%$, the droplet size becomes much smaller than the He-Ne laser wavelength. Moreover, the influence of surface anchoring to these tiny droplets is no longer significant. As a result, the contrast ratio decreases sharply. On the other hand, for the 8- μm PDLC at $c=50\%$ its droplet size is still $\sim 1.5\text{X}$ larger than that of T-PDLC so that the light scattering remains significant. Its optimal polymer concentration should occur at a higher level. Increasing cell gap would improve the contrast ratio for both T-PDLC and PDLC at the expense of increased voltage. Increasing curing temperature³⁴ is another option for improving contrast ratio. However, the response time becomes slower.

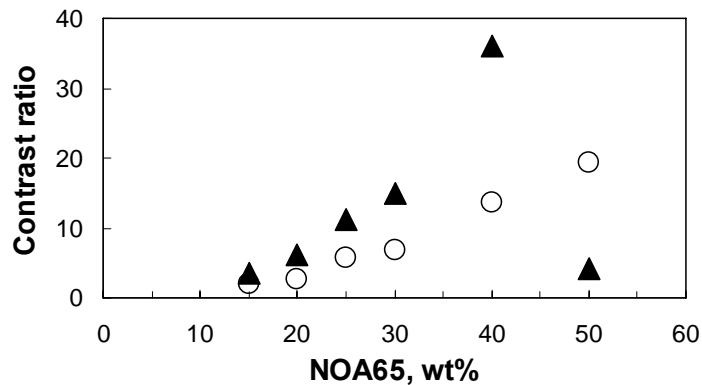


Figure 23: Polymer concentration effect on device contrast ratio. Triangles are for the 6.5 μm T-PDLC cell and circles are for the 8 μm PDLC cell.

3.1.6 Response Time

The response time of the transmissive T-PDLC and PDLC cells was measured at room temperature using 20 V_{rms} square pulses. In general, the PDLC response time depends on the LC viscosity, droplet size and shape, and the ratio of the applied voltage

over threshold voltage.³⁵ For the 6.5- μm -thick T-PDLC cell ($c=40\%$), the measured rise time (10-90%) is ~ 5 ms and decay time (90-10%) is ~ 10 ms. In contrast, the 40% PDLC has 7.6 ms rise time and 21 ms decay time. The faster response time of T-PDLC originates from its smaller droplet sizes. To further improve switching speed, we could reduce the droplet size by increasing the polymer concentration or use a lower viscosity LC. However, smaller droplet sizes require a higher operating voltage. Holographic PDLC is such an example.²⁸

3.1.7 Reflective Mode TPDLC

From Figure 22, the contrast ratio of the thin transmissive T-PDLC and PDLC cells is insufficient for display or light switch applications. To enhance contrast ratio, a thicker LC layer or reflective mode operation can be considered. A thicker PDLC layer would result in a higher operating voltage. For the interest of keeping operating voltage low, reflective mode is preferred. In a reflective device, the incident light traverses the LC layer twice so that its contrast ratio is increased by a quadratic function.³⁶

Figure 24 depicts the voltage-dependent reflectance of the T-PDLC (solid line) and PDLC (dashed lines) cells with $c=40\%$. The cell gap for the T-PDLC and PDLC is 6.5 μm and 8.0 μm , respectively. In principle, the reflector should be imbedded in the inner side of the cell in order to avoid parallax.³⁷ For proving concept, we simply placed a dielectric mirror behind the transmissive cell. To avoid overlapping, the reflected unpolarized He-Ne laser beam was deviated from the incident beam by $\sim 4^\circ$. The collection angle of the photodiode detector remains at $\pm 1^\circ$. The inset in Figure 24 shows

the magnified dark state reflectance. Apparently, T-PDLC exhibits a better dark state than PDLC, although its cell gap is thinner. At $V \sim 20 V_{\text{rms}}$, the measured contrast ratio of the PDLC cell is $\sim 250:1$. For T-PDLC, the measured contrast ratio is $\sim 900:1$, which is not too far off from the square of $35:1$ (the contrast ratio of the transmissive mode). Indeed, double pass significantly improves the device contrast ratio.

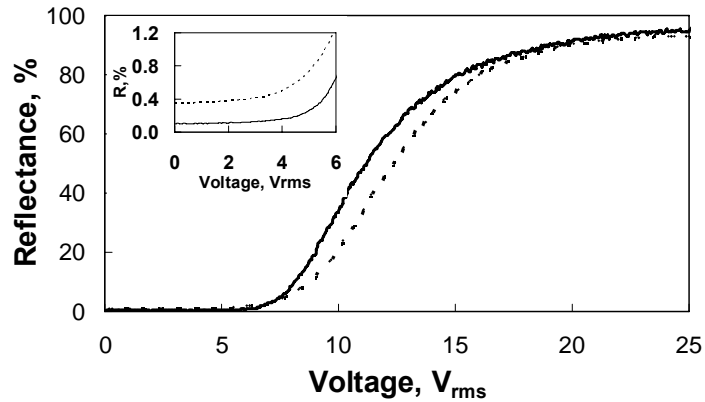


Figure 24: The voltage dependent reflectance of T-PDLC (solid line; $d=6.5 \mu\text{m}$) and PDLC (dashed lines; $d=8 \mu\text{m}$). The inset shows the magnified scale for comparing the dark state.

3.1.8 Reflective Dye-doped TPDL

The dark state of a light scattering-based display is translucent, rather than black. To realize a black and white display, we added a $\sim 2 \text{ wt}\%$ black dye to the $c=40\%$ T-PDLC cell. The cell gap is $d \sim 6.7 \mu\text{m}$. The bottom ITO electrode was etched into a segmented number “8”. The T-PDLC cell preparation process remains the same. For demonstration purpose, we placed a piece of white paper behind the bottom substrate to serve as a diffusive reflector. Figure 25 shows the displayed image at $V=20 V_{\text{rms}}$. The on-state T-PDLC is highly transparent so that the reflected image appears white. Since the

display does not require a polarizer, the viewing angle is wide and the display is bright under room light condition. The display contrast ratio was measured to be $\sim 10:1$, limited by the dichroic ratio of the employed dye molecules. The doped 2% dye molecules slightly increase the switching time. Further increasing the dye concentration would enhance the display contrast ratio at the tradeoffs of lower bright state reflectance and slower response time



Figure 25: The displayed image using a dye-doped T-PDLC reflective display. Black dye concentration: 2%, LC/polymer mixture: NOA65:E48=40:60, $d=6.7 \mu\text{m}$, and $V=20 V_{\text{rms}}$. A white paper was placed behind the bottom substrate to act as a diffusive reflector.

The contrast ratio of the dye-doped T-PDLC is still not good enough in Figure 25. There are several reasons⁴. First, it is the solubility problem which means some dyes are dissolved not only in liquid crystal host but also in the polymer matrix. The dyes dissolved in the polymer matrix affect the light scattering and also change the absorbance. Second, the order parameter of dye is not as good as liquid crystal molecules. Third, the dye concentration we used is low and its dichroic ratio is not high enough. To reduce the dye in the polymer matrix, we can instead use polymer network structure.

3.1.9 Conclusion

In conclusion, the T-PDLC exhibits a more efficient light scattering than the conventional PDLC. The formed droplets are smaller and more uniform in T-PDLC because of the surface pinning effect in thin cells which will be discussed in next section. A reflective black and white display using 2% dye-doped T-PDLC shows a reasonably good contrast ratio. The required operating voltage is still too high to be used for active matrix display. To avoid image flickering for active matrix display, the employed LC mixture should have a high resistivity.

3.2 Surface Pinning Effect in Thin PDLCs

The phase separation, which is an important process affecting the electro-optic properties of PDLCs, has been studied by computer simulations³⁸⁻⁴¹ and by experiments⁴²⁻⁴³. In a conventional PDLC, the formed droplets, each about the size of a visible wavelength, are randomly distributed in the polymer matrix. Typically, the LC and monomer mixture is sandwiched between two indium-tin-oxide (ITO) glasses without any surface treatments. After photo-induced phase separation, the droplets are formed and their sizes vary. Due to the relatively large cell gap and micron-sized LC droplets, phase separation dynamics do not depend on surface interaction. The phase separation dynamics determine the final composite morphology of PDLC. The more uniform LC droplets exhibit a higher light scattering efficiency and higher device contrast ratio^{4,11}.

Several factors, such as the transition from isotropic to nematic ordering of the LCs, the solubility of the LC and monomer, the growing molecular weight and the gelation of polymer matrix and elastic forces in the polymer matrix^{4,44}, compete with each other to determine the phase separation dynamics of PDLCs. In this paper, we demonstrate that the phase separation dynamics are influenced by the surface effect for a PDLC confined in a thin cell. The PDLCs with a strong surface anchoring exhibit smaller LC droplets and better uniformity because the anchoring force in the boundaries fixes the droplets and prevents them from flowing and coalescing.

In this section, we demonstrate that the phase separation dynamics are influenced by the surface effect for a PDLC confined in a thin cell^{12,46}. The PDLCs with a strong surface anchoring exhibit smaller LC droplets and better uniformity because the

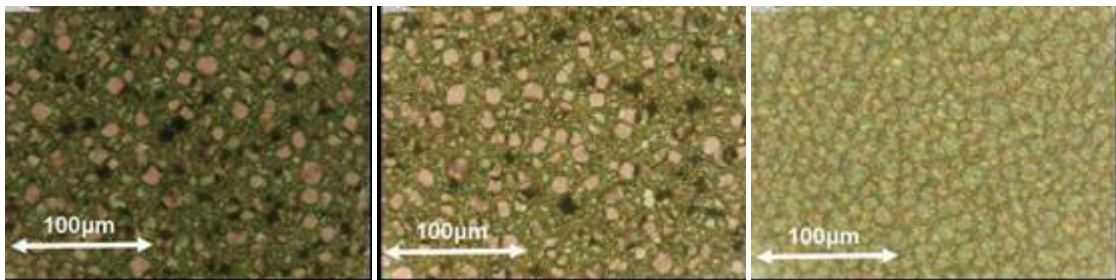
anchoring force in the boundaries fixes the droplets and prevents them from flowing and coalescing.

3.2.1 Sample Preparation

To fabricate a PDLC device, we mixed UV-curable monomer NOA65 in a nematic LC host (E48, $\Delta n = 0.231$ at $\lambda = 589$ nm and $T = 22^\circ\text{C}$). We varied the polymer concentration from 20 to 40 wt%. However, the general phenomena remain the same except for the different droplet sizes. Thus, we focus our discussions using the PDLC with 30 wt% NOA65 as examples. The LC and monomer mixture was injected into an empty cell in the isotropic state. The cell gap is $d = 8$ μm . For comparison, we prepared several types of cells with different surface treatments: 1) a conventional PDLC cell, i.e. the indium-tin-oxide (ITO) glass substrates without polyimide (PI) alignment layers, 2) a PI cell, i.e. an ITO glass cell with each inner surface overcoated with a thin (~ 10 nm) PI layer but without rubbing, 3) a 90° twisted nematic (TN) cell, i.e. the ITO glass substrates with orthogonal rubbing alignment layers, 4) a homogeneous cell, i.e. the ITO glass substrates with anti-parallel rubbing alignment layers, 5) a 45° twisted nematic (45° -TN) cell, i.e. the rubbing directions of the ITO glass substrates are at 45° , and 6) a single-sided rubbing cell, in which only one substrate was rubbed, the other had plain PI. In the TN and homogeneous cells, the polar anchoring energy of the buffed PI layers was measured to be $\sim 3 \times 10^{-4}$ J/m² by the voltage-dependent phase retardation method^{45,47}. The pretilt angle of these cells is about 3° .

3.2.2 Surface Pinning Effect

Figure 26(a) to (f) show the morphologies of the abovementioned UV-cured PDLC cells observed from a polarized optical microscope in the voltage-off state. The UV exposure intensity was $I=60 \text{ mW/cm}^2$ and the curing time for both cells was 15 min at $T=20 \text{ }^\circ\text{C}$. From Figure 26(a) and Figure 26(b), we find that the LC droplets in the conventional and non-rubbed PI cells are larger and less uniform than those observed in Figure 26(d) for the 90° -TN cells, Figure 26(e) for the 45° -TN cells and Figure 26(f) for the homogeneous cells. That means the rubbed PI surfaces have a crucial influence on the phase separation of PDLC when the cell gap is thin. The smaller and more uniform LC droplets exhibit a higher light scattering efficiency which, in turn, leads to a higher device contrast ratio¹¹. The droplets are more uniform in the single-sided rubbing than in the conventional and non-rubbed PI cells. Besides, the single-sided rubbing has larger droplet sizes than the TN, 45° -TN and homogeneous cells. For comparison, the morphologies of a weak-rubbing homogeneous cell (Figure 26(g); anchoring energy $W\sim 1\times 10^{-4} \text{ J/m}^2$) and sputtered SiO_2 alignment layers (Figure 26(h); $W\sim 8\times 10^{-5} \text{ J/m}^2$) are also less uniform.



(a)

(b)

(c)

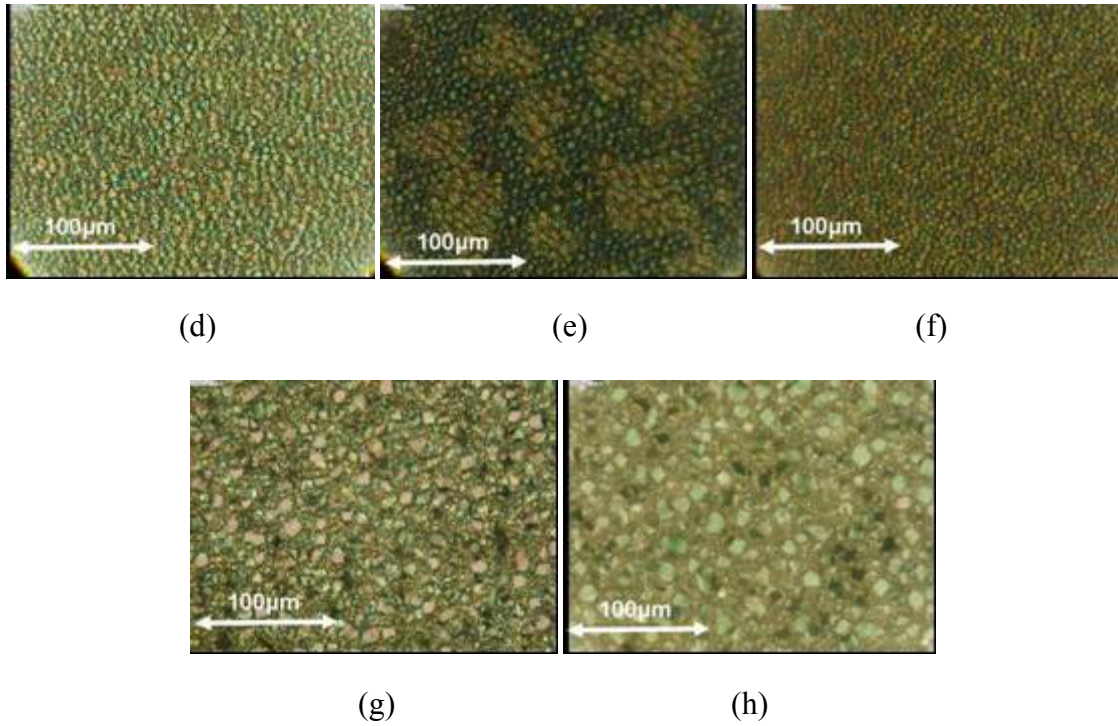
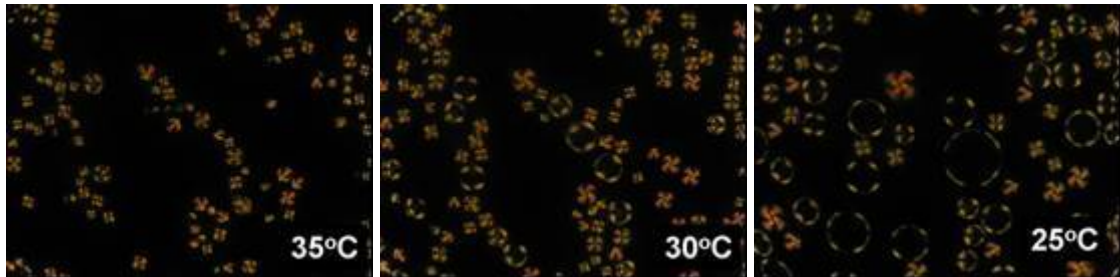


Figure 26: Phase separation morphologies of PDLC in (a) conventional cell, (b) PI cell without rubbing, (c) single-side rubbing (d) 90°-TN cell (anchoring energy $W \sim 3 \times 10^{-4} \text{ J/m}^2$), (e) 45°-TN cell ($W \sim 3 \times 10^{-4} \text{ J/m}^2$), (f) homogeneous cell ($W \sim 3 \times 10^{-4} \text{ J/m}^2$), (g) homogeneous cell (weak rubbing, $W \sim 1 \times 10^{-4} \text{ J/m}^2$), and (h) homogeneous cell with SiO_2 alignment layers ($W \sim 8 \times 10^{-5} \text{ J/m}^2$) observed from a polarized optical microscope. LC/monomer mixture: 70 wt% E48 and 30 wt% NOA65. All the devices have the same cell gap $d \sim 8 \text{ } \mu\text{m}$.

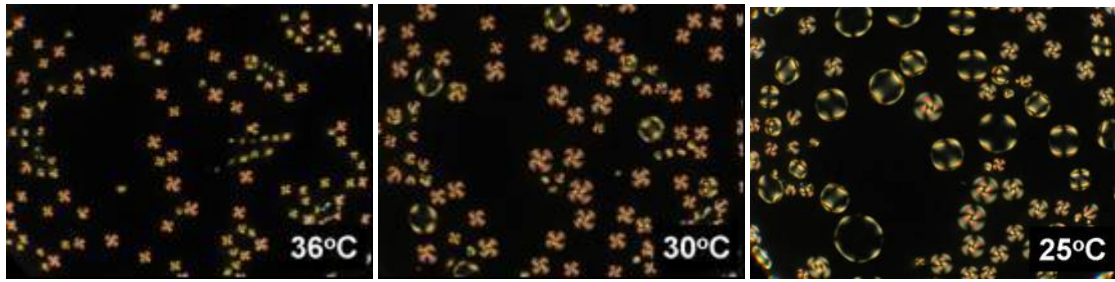
3.2.3 Thermal-induced Phase Separation of PDLC

To show that the phase separation dynamics indeed depend on the surface rubbing conditions, we observed the morphologies of the four PDLC cells from a polarized optical microscope in the voltage-off state before UV curing. Results are shown in Figure 27 (a)-(d). The cells were put on a heating stage and their temperatures were probed by a thermocouple. In Figure 27 (a) and Figure 27 (b), the LC droplets in the conventional

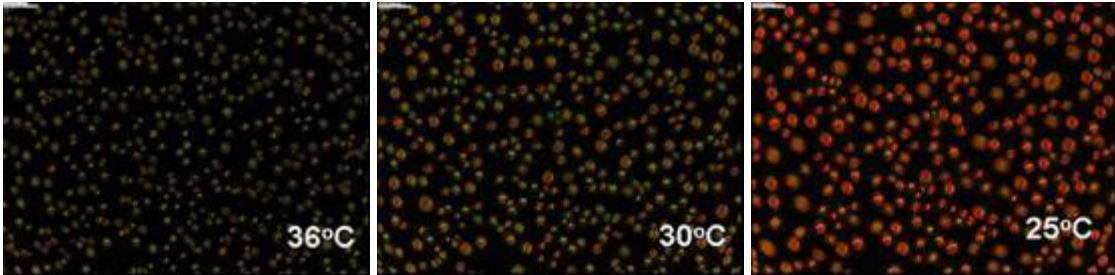
substrates and in the PI cells start to appear at $T \sim 40$ °C when the temperature was cooled from the clearing point ($T_c = 65$ °C) of the LC/monomer mixture. In both figures, the LC droplets nucleate and grow at the beginning and then rapidly flow and coalesce due to the absence of the anchoring force (for the conventional cell) or a weak anchoring force (for the PI cell) in the ITO substrates during the cooling process. In Figure 27 (c) and Figure 27 (d), the LC droplets confined in the TN and homogeneous cells begin to appear at $T \sim 38$ °C when the temperature is cooled down slowly from $T_c = 65$ °C. The LC droplets continue to nucleate and grow but remain basically static during the cooling process. These “pinned” droplets move only slightly but barely coalesce with the surrounding droplets. This is because the strong anchoring forces from the boundaries prevent the LC droplets from flowing. As the temperature decreases, the sizes of the LC droplets in both of the rubbed cells are smaller and the size variation is less than those in the non-rubbed PI cells. The color difference between the low and high temperatures is due to the temperature-dependent LC birefringence⁴⁸.



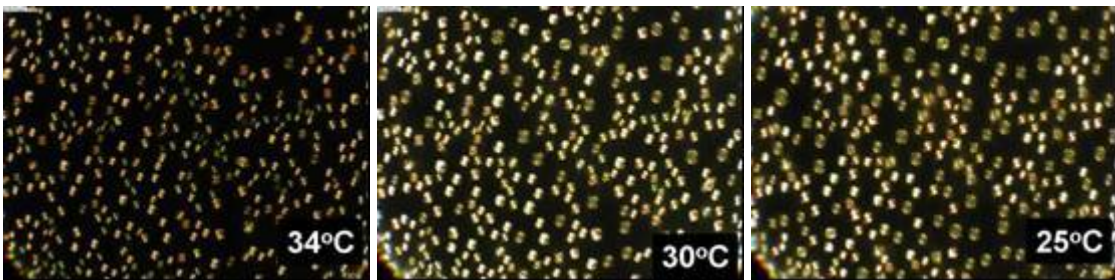
(a)



(b)



(c)



(d)

Figure 27: The dynamic phase separation morphologies of PDLC observed from a polarized optical microscope under different temperatures without UV illumination: (a) conventional PDLC cell, (b) PI without rubbing, (c) TN cell, and (d) homogeneous cell.

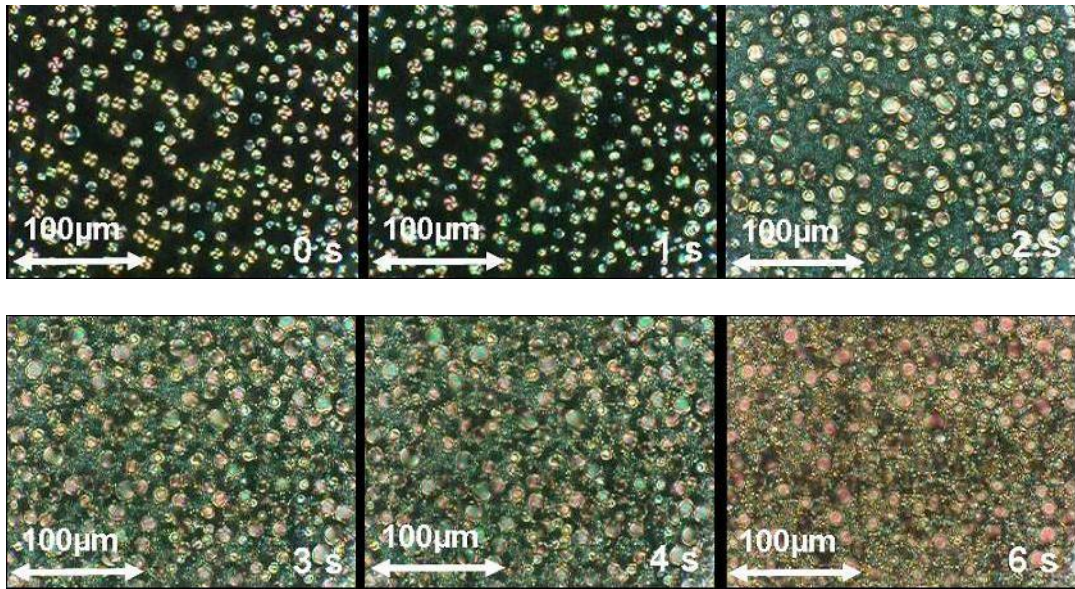
3.2.4 Dynamic Phase Separation of PDLC

In Figure 28 and Figure 29, the cells were cooled to $T=27^{\circ}\text{C}$ and then illuminated by UV light at $t=0$. Meanwhile, the phase separation animations were simultaneously recorded on a digital camera (Olympus Camedia C-3040) connected to a polarized optical

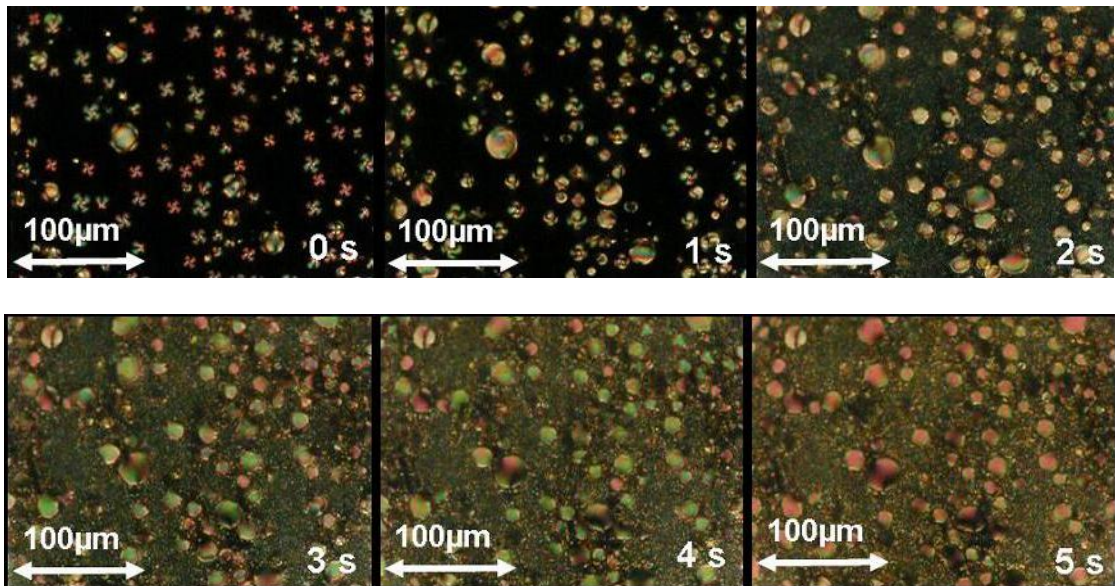
microscope. In Figure 28(a)-(b), we show the time-resolved morphologies in the conventional cell (without PI) and the PI cell without rubbing. The LC droplets exist at $t=0$ due to the thermal-induced phase separation even before UV exposure took place. The following nucleated LC droplets caused by the increased expulsion of LCs from the polymer matrix flow in the conventional and PI cells due to the weak or the lack of anchoring forces in the boundary substrates. When the nucleated and flowing LC droplets approach each other, they coalesce. As the polymerization reaction continues, gelation gradually occurs which resists the growth of the moving and nucleating LC droplets. The LC droplets are frozen by the polymer matrix when the polymer matrix reaches its gelation point. The morphologies remain basically unchanged after $t=6$ s for the conventional cell and after $t=5$ s for the PI cell without rubbing because the polymer matrix has either grown sufficiently in molecular weight or reached its gelation point, impeding further coalescence. The resultant morphology consists of LC droplets dispersed in the polymer matrix. The droplet size decreases with an increase in the UV curing temperature or UV exposure intensity. The sizes of the LC droplets are not quite uniform due to first the flow and then the coalescence.

The time-resolved morphologies in the TN and homogeneous cells are shown in Figure 29(a) and Figure 29(b), respectively. The cells were also cooled to $T=27^{\circ}\text{C}$ and illuminated by UV light at $t=0$. At $t=0$, the morphologies shown in Figure 29(a) and Figure 29(b) are different from those shown in Figure 28(a) and Figure 28(b). The LC droplets appear to be smaller in size and are uniformly dispersed at $t=0$ because they are anchored by the boundary anchoring force which prevents the droplets from moving and coalescing. As the photo-induced polymerization reaction goes on, the LC droplets are

frozen by the boundary anchoring force and by the polymer matrix which gradually reaches its gelation point. The LC droplets stop growing when the gelation point of the polymer matrix is reached. The morphologies which have better uniformity and smaller droplet sizes remain the same after 4 seconds in the TN and homogeneous cells.

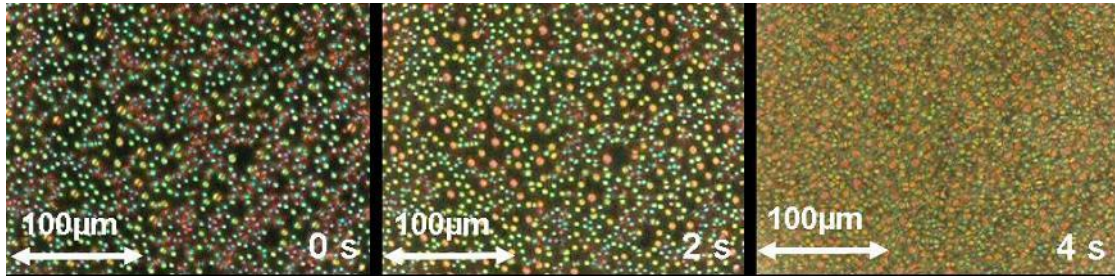


(a)

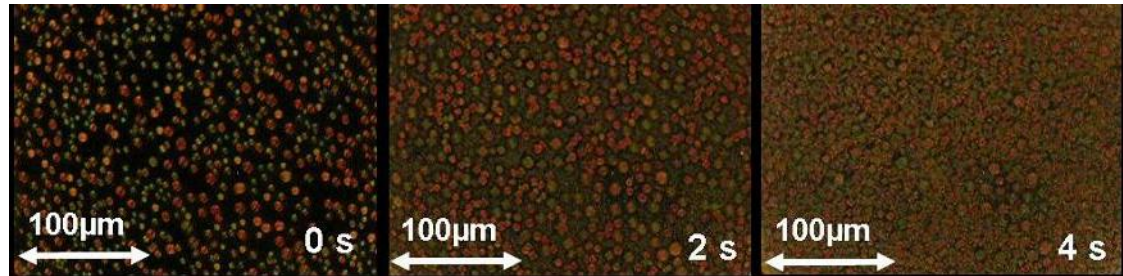


(b)

Figure 28: The dynamic phase separation morphologies of PDLC at $T=27^{\circ}\text{C}$ with UV exposure starting at $t=0$: (a) conventional cell without PI, and (b) PI cell without rubbing. The UV intensity is $I=60\text{ mw/cm}^2$.



(a)



(b)

Figure 29: The dynamic phase separation morphologies of PDLC at $T=27^{\circ}\text{C}$ with UV exposure starting at $t=0$: (a) TN cell, and (b) homogeneous cell. The UV intensity is $I=60\text{ mw/cm}^2$ and cell gap $d=8\text{ }\mu\text{m}$.

3.2.5 Cell Gap Effect

Figure 30 shows the morphologies of homogeneous PDLC cells with various cell gaps at $T=20^{\circ}\text{C}$, as observed from a polarized optical microscope. The larger cell gap shows a larger droplet size. This is because the strong boundary effect only influences the droplets nearby the surfaces. As the cell gap increases, the bulk droplets are not influenced by the surfaces. During the phase separation processes, the PDLC droplets in

the middle layers can still flow and result in larger droplets sizes as illustrated in Figure 31. Due to the pinning effect of the droplets near surfaces, the morphologies of the cell whose gap is $<16\ \mu\text{m}$ are still uniform.

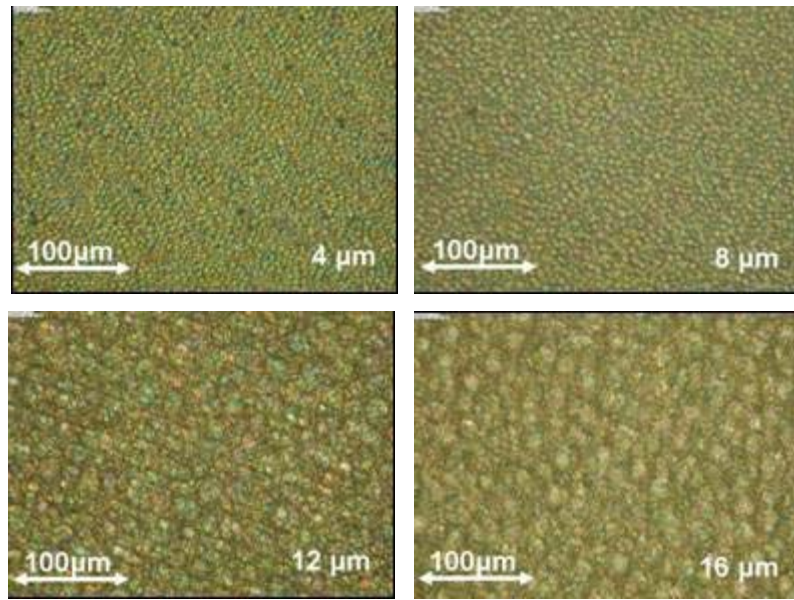


Figure 30: The morphologies of the homogeneous PDLC cells with various cell gaps at $T=20^\circ\text{C}$ observed from a polarized optical microscope. LC/monomer mixture: 70 wt% E48 and 30 wt% NOA65.

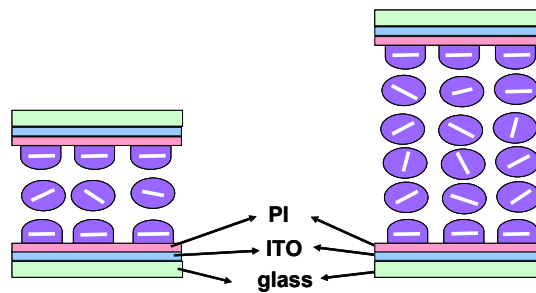


Figure 31: When the cell gap is larger, the surface anchoring effect is weaker to the bulk.

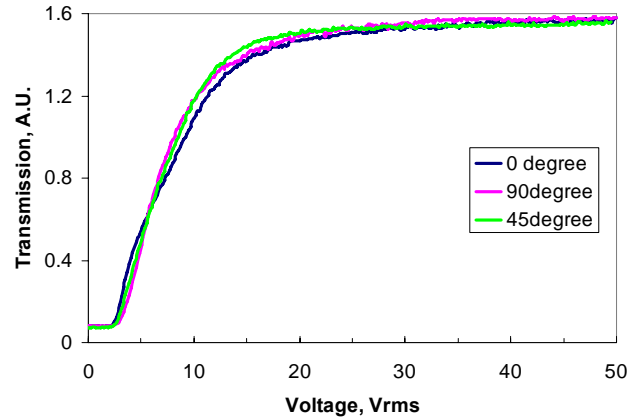


Figure 32: PDLC in orthogonal-rubbed thin cell is polarization independent. The cell gap is $6.5 \mu\text{m}$.

Similar to a conventional PDLC, the light scattering behavior of the thin TN PDLC cell is also independent of light polarization as shown in Figure 32. In Figure 32, the voltage dependent transmission in the thin TN PDLC cell remains the same when we rotate the polarizer at 0, 45 and 90 degrees. This is because the orthogonal surface alignments influence the LC orientation in the boundary PDLC layers. This phenomenon of the complementary birefringence colors of the cell is observed under polarized optical microscope when the polarizers are crossed. On the other hand, the PDLC in the thin ($d=4 \mu\text{m}$) homogeneous cell is dependent on the incident light polarization, as shown in Figure 33. As the cell gap increases, the surface effect to the bulk LC droplets is reduced due to the longer distance. Therefore, the bulk LC droplets are more randomly distributed and the light scattering behavior is less sensitive to polarization. Also included in Figure 33 is the voltage-dependent transmittance of a $16\text{-}\mu\text{m}$ homogeneous PDLC cell. Although the cell has the same anchoring energy as the thin cell, the bulk droplets are less ordered

in a thicker cell so that the overall light scattering behavior is less dependent on the incident light polarization.

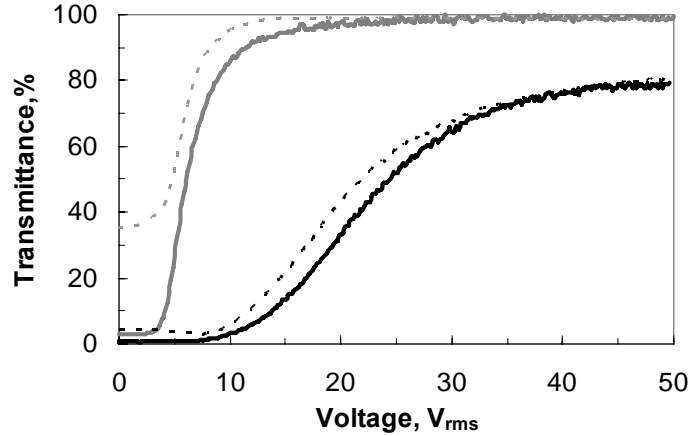


Figure 33: Voltage-dependent transmittance of the 16- μm (black solid and dashed lines) and 4- μm (gray solid and dashed lines) homogeneous PDLC cells. Solid lines: the input polarization is parallel to the cell rubbing direction. Dashed lines: the input polarization is perpendicular to the rubbing direction. $\lambda=633\text{ nm}$ and $T=22^\circ\text{C}$.

3.2.6 Conclusion

The surface pinning effects on phase separation dynamics of PDLCs with thin cell gaps are demonstrated. Comparing various boundary conditions, the inner surfaces of the substrates with or without polyimide layers [but no rubbing] cannot provide enough anchoring force, so in either case the LC droplets flow and coalesce to form larger and less uniform droplets. However, if the inner surfaces of the substrates are coated with rubbed polyimide layers with anchoring energy $>1 \times 10^{-4}\text{ J/m}^2$, almost all the nucleated LC droplets grow at a fixed position during phase separation. The appearance of the

coalescence is not obvious and the formed LC droplets are relatively uniform. The surface anchoring has a significant effect on the morphology of PDLCs.

3.3 Reflective Dye-doped Dual-frequency LC Gels

The dye-doped T-PDLC presented in previous section has inadequate contrast ratio. To avoid that the dye dissolved into the polymer matrix, in this section we consider polymer network liquid crystals. Here, we demonstrate a new GH LCD using a dye-doped DFLC gel to realize polarizer-free, fast response, and high contrast reflective display^{13,14}. This is a normally white display utilizing both light scattering and absorption effects. In the voltage-off state, the gel exhibits ~50% reflectance. At ~30 V_{rms}, a good black state is observed. The device contrast ratio as high as ~230:1 is obtained. The response time is ~5 ms.

3.3.1 Operation Principle

To improve response time and light scattering efficiency, our group has developed a polarization independent DFLC gel⁴⁹. The gel is also a light scattering device. Two important features of the DFLC gel are fast response time and high contrast ratio. This gel has been used for high speed photonic devices. But for displays, we need a good black state, high contrast ratio, and wide viewing angle.

The light modulation mechanisms of the dye-doped DFLC gel can be schematically depicted in Figure 34(a) to Figure 34(c). At V=0, the cell does not scatter light and the absorption is rather weak because the dye molecules are aligned perpendicular to the substrates, as shown in Figure 34(a). Therefore, the display has the highest reflectance. This is known as the normally-white mode. When the applied high-

frequency ($f > f_c$) voltage exceeds a threshold, the LC directors and dye molecules are tilted away from the electric field because the LC has a negative $\Delta\epsilon$. Under such a circumstance, the gel is switched into micron-sized domain structure. The tilted direction is random because the substrates do not have any alignment treatment, as depicted in Figure 34(b). As a result, the reflectance is reduced due to light scattering of the gel and absorption of the dyes. As the applied voltage increases further, the liquid crystals and dye molecules are reoriented in the x-y plane, as shown in Figure 34(c), so that light scattering and dye absorption efficiency reach their maxima and the display appears black and is polarization independent.

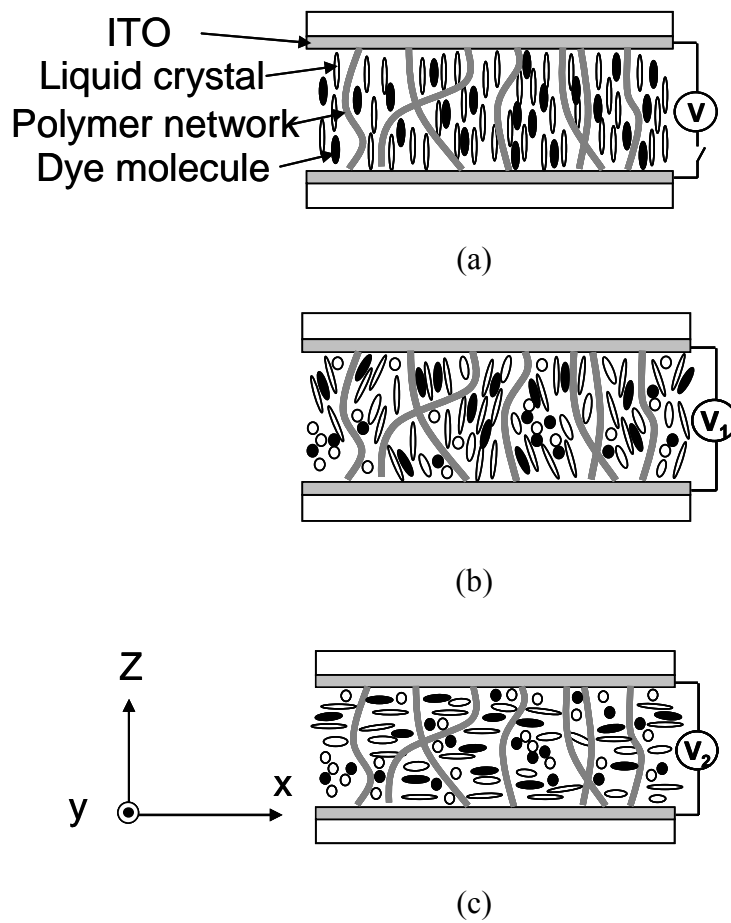


Figure 34: Schematic representation of the operating principle. (a) Voltage-off state, (b) voltage-on state, and (c) voltage-on state and $V_2 > V_1$. The PI has no rubbing treatment.

3.3.2 Sample Preparation

To fabricate DFLC gel, we first prepare a DFLC mixture consisting of some biphenyl esters and lateral difluoro tolanes. The formulated DFLC mixture has following physical properties: birefringence $\Delta n=0.267$ (at $\lambda=633$ nm, $T=21^\circ\text{C}$), cross-over frequency $f_c=10$ kHz, and dielectric anisotropy $\Delta\epsilon= 7.72$ at $f= 1$ kHz and $\Delta\epsilon= -3.51$ at $f= 50$ kHz. We mixed the DFLC, a diacrylate monomer (bisphenol-A-dimethacrylate), and the dichroic dye S428 (Mitsui Chemicals Inc.) at 90:5:5 wt % ratios. The mixture was injected into an empty cell whose inner surfaces were coated with a thin indium-tin-oxide (ITO) electrode. The cell gap is $d=5$ μm . The filled cell was irradiated by a UV light ($\lambda\sim 365$ nm, $I\sim 15$ mW/cm^2) at room temperature for 1 hour with a biased voltage ~ 40 V_{rms} ($f= 1$ kHz). The formed chain-like polymer networks are along the electric field direction because the LC directors are aligned perpendicular to the glass substrates during the UV curing process, as shown in Figure 34(a).

3.3.3 Electro-optical Properties

To measure the reflectance of the dye-doped DFLC gel, ideally we should use an unpolarized white light. The dye we employed appears black, but when dissolved in the gel system it appears dark red. Its cutoff wavelength was measured to be ~ 650 nm. That means it has some light leakage in the red spectral region. Therefore, we used a linearly polarized green diode laser ($\lambda=532$ nm) for characterizing the device performances. A dielectric mirror was put behind the cell so that the laser beam passed through the cell twice. A large area photodiode detector was placed at ~ 40 cm behind the sample which

corresponds to $\sim 1.5^\circ$ collection angle. A computer controlled LabVIEW data acquisition system was used for driving the sample and recording the light reflectance.

Figure 35 plots the voltage-dependant reflectance of the dye-doped DFCL gel. The reflectance is normalized to that of a pure DFCL cell with the same cell gap. At $f=1$ kHz, the applied voltage cannot reorient the dye-doped DFCL gel because the LC directors are in homeotropic structure and $\Delta\epsilon$ is negative. At $f=50$ kHz, the reflectance remains higher than 50% in the low voltage regime and decreases gradually as $V > V_{th}$. For the 5- μm gel, $V_{th} \sim 7V_{rms}$. At $V=30 V_{rms}$, the measured contrast ratio for the green laser beam is as high as 150:1.

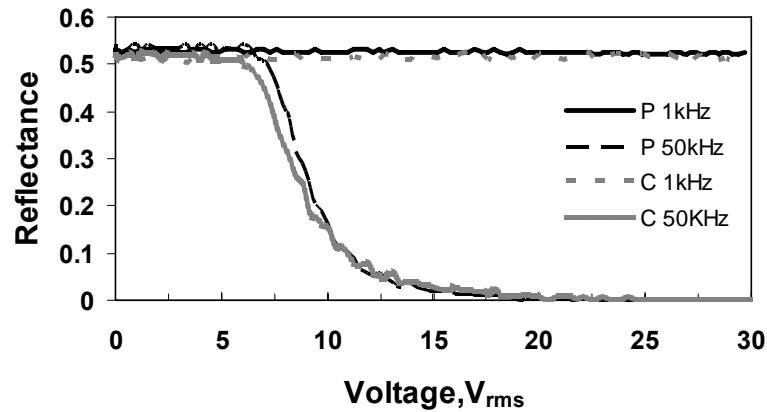


Figure 35 Voltage-dependent reflectance of dye-doped DFCL gel. P and C's polarizations of the incident light are orthogonal.

To verify that the gel is indeed polarization independent, we rotated the cell by 90° and repeated the voltage-dependant reflectance curves. Results are plotted in Figure 35, where P and C's polarization of the incident light are orthogonal to the LC cell. From Figure 35, the P and C curves almost overlap each other. That means our dye-doped DFCL gel is polarization independent. The contrast ratio (CR) is defined as the ratio of

reflectance at $V = 30 V_{rms}$ and 0. The CR is ~ 230 at $f = 50$ kHz and the maximum reflectance is $\sim 50\%$.

For a scattering device, the contrast ratio is dependent on the distance of the detector from the sample, as shown in Figure 36. In a handheld reflective display, a comfortable viewing distance is about 20-25 cm. To mimic this condition, we shortened the detecting distance from 40 to 20 cm and the measured contrast ratio is still 120:1. This result indicates that our gel has a very strong scattering property. The scattered light diverges quite fast.

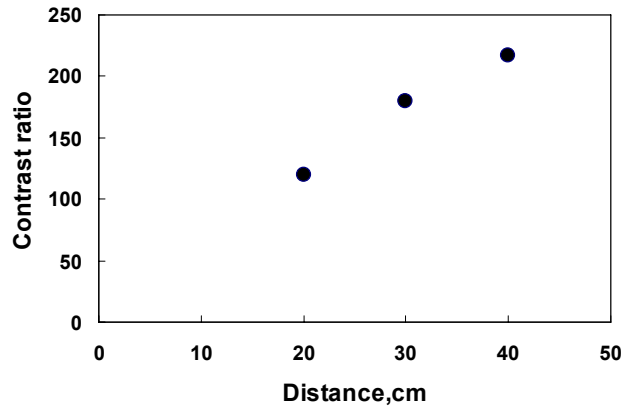


Figure 36: Contrast ratio as a function of detector's distance from sample.

In our sample, the dark state voltage is still high ($\sim 30 V_{rms}$) and it can be reduced by using a higher $\Delta\epsilon$ DFLC material, thinner cell gap, or lower monomer concentration. The contrast ratio can be further improved by increasing the cell gap, monomer concentration, or dye concentration. However, increasing dye concentration would reduce display reflectance and lead to a slower response time, increasing polymer concentration would cause a higher operating voltage, and increasing cell gap would increase the operating voltage, reduce the voltage-off state reflectance, and lengthen the response time.

Figure 37 shows the voltage-dependant reflectance of a 5- μm and 8- μm cells. In both cells, the LC host and dye and polymer concentrations are kept the same. As the cell gap increases from 5 to 8 μm , the bright-state reflectance decreases from 52% to 28% when a high-frequency voltage is applied. Although the contrast ratio is improved, the bright state reflectance is greatly sacrificed. Thus, this approach is not worth taking.

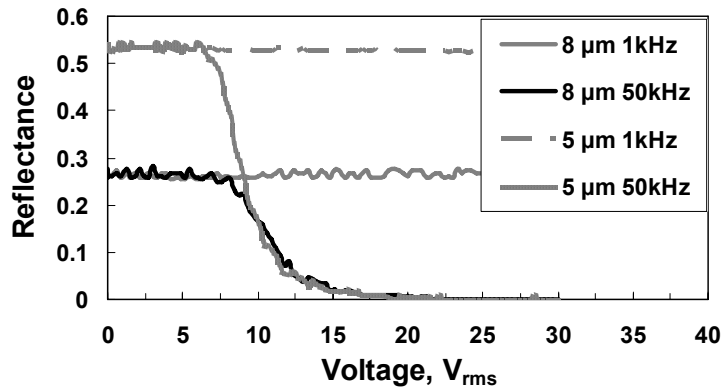


Figure 37: Voltage-dependent reflectance of dye-doped DF LC gel with different cell gaps. Dye and polymer concentrations are kept at 5 wt %.

3.3.4 Reflectance Spectra

Figure 38 shows the reflectance spectra of dye-doped DF LC gel at 0 (black line) and $20V_{\text{rms}}$ at $f=50$ kHz (gray line). The light source we used is standard white light source (Mikropack, DH-2000, UV-VIS-NIR). We used an iris and a lens to collimate the white light and expand the beam diameter to $\sim 4\text{mm}$. A dielectric mirror was placed behind the LC cell for reflective mode measurement. The output beam was collected by a lens to a fiber-optics based universal serial bus (USB) spectrometer (resolution=0.04 nm; USB HR2000, Ocean Optics). The baseline we used for calibration was a pure LC cell

with the same cell gap. In Figure 38, at $V=0$ the reflectance of the dye-doped DF LC gel is $\sim 50\%$ between 450 and 550 nm. Beyond 550 nm, the reflectance increases because our dye-doped DF LC gel looks reddish, rather than black.

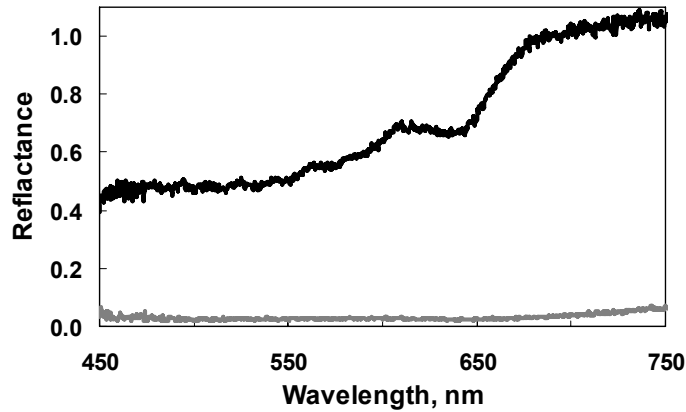


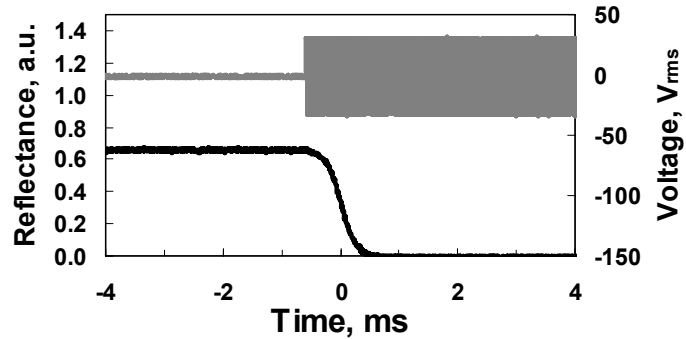
Figure 38: Reflectance spectrum of dye-doped DF LC gel at 0 V_{rms} (black line) and at 20 V_{rms} (50 kHz) (gray line).

3.3.5 Response Time

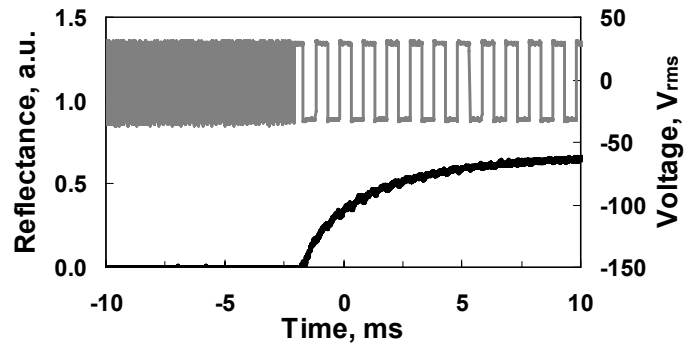
Response time is another important issue for guest-host displays. The dye molecules are usually bulky and have a large viscosity. Moreover, guest-host displays do not use any polarizer so that their governing response time equations are different from those with polarizers. As a result, a typical response time of a guest-host display is around 50 ms. Detailed values depend on the dye concentration and cell gap.

The response time of our dye-doped DF LC gel is fast. Figure 39 shows the measured response times of the 5- μm gel. If we switch the applied voltage from 0 to 30 V_{rms} at 50 kHz frequencies, the rise time is 1 ms and decay time is 10 ms. If we fix the

voltage at $30 V_{\text{rms}}$ while switching the frequency between 1 kHz and 50 kHz, the rise time is reduced to ~ 0.55 ms and decay time to ~ 5.78 ms, as shown in Figure 39(a) and Figure 39(b). Fast response time is a key feature of the DFLC materials.



(a)

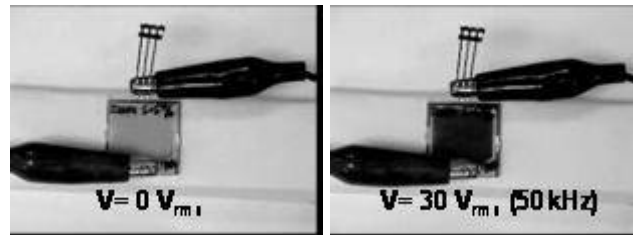


(b)

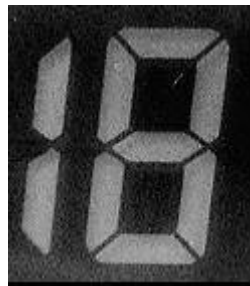
Figure 39: Measured response time of a $5\text{-}\mu\text{m}$ dye-doped DFLC gel at $V=30V_{\text{rms}}$. The upper traces show the dual-frequency (50 kHz and 1 kHz) addressing and lower traces show the corresponding optical signals. (a) Rise time= 0.55 ms and (b) decay time= 5.78 ms. $\lambda=532$ nm.

3.3.6 Reflective Direct-View Displays Using a Dye-doped LC Gel

Figure 40(a) shows a single pixel of the 5- μm dye-doped DFCL reflective display at 0 V_{rms} and 30 V_{rms} (50 kHz). It shows good bright and dark states. To prove principle, we fabricated a segmented reflective display using the dye-doped DFCL gel. Figure 40(b) shows a sample using a 7- μm dye-doped DFCL gel. To avoid specular reflection, we laminated a diffusive reflector on the backside of the bottom glass substrate in order to widen the viewing angle. The bright segments represent the areas without ITO electrodes. Since no voltage was applied, these segments appear white. The dark areas represent the ITO electrodes with $V=30 V_{\text{rms}}$ at $f=50 \text{ kHz}$.



(a)



(b)

Figure 40: (a) Single pixel of the 5- μm dye-doped DFCL reflective display at $V=0$ and 30 V_{rms} (50 kHz). (b) A device of the dye-doped DFCL reflective display. A diffusive reflector is laminated to the back of the bottom glass substrate. In the white segments, the ITO electrodes were etched away so that $V=0$. Cell gap= $7 \mu\text{m}$.

3.3.7 Discussion and Conclusion

The dye-doped DF LC gel exhibits a good contrast ratio due to strong scattering and dye absorption. The reflectance (R) can be expressed as

$$R = e^{-\beta \cdot d \cdot N_1} e^{-\alpha \cdot c \cdot d \cdot N_2}, \quad (22)$$

where α is the average absorption coefficient, β is the scattering coefficient, c is the dye concentration (~ 0.05), d is the cell gap ($\sim 5 \mu\text{m}$), and N_1 and N_2 are the scale numbers because of the multiple scattering and absorption. In Eq. (22), α is equal to $\alpha_{//}$ or α_{\perp} which stand for the absorption coefficients when the incident light polarization is parallel or perpendicular to the principal molecular axis of the dye molecules. At $V=0$, the dye absorption (α_{\perp}) dominates and the gel's scattering is negligible. In a high voltage state at a high frequency, α can be expressed as:

$$\alpha = \frac{\alpha_{//} + \alpha_{\perp}}{2}, \quad (23)$$

because all the dye molecules are randomly oriented along the x - y plane. In dye-doped PDLC, droplets are randomly dispersed in 3-dimensional space. So α is:

$$\alpha = \frac{\alpha_{//} + 2\alpha_{\perp}}{3}, \quad (24)$$

By comparing Eq. (23) with Eq. (24), our dye-doped DF LC gel has a larger average absorption coefficient than the dye-doped PDLC. Due to the multi-domain structure and the random LC arrangement along the x - y plane, the gel's scattering efficiency is maximized and independent of polarization. In addition, the dark state

reflectance is minimized owing to the multiple light scattering in conjunction with dye absorption.

We have demonstrated a polarizer-free, high contrast, and fast response new reflective GH LCD using a dye-doped DFLC gel. The fabrication process is relatively simple as compared to the double cell GH LCD. The reflectance reaches ~50% and the contrast >100:1. The response times are fast (0.55 ms rise and 5.8 ms decay) when using the dual-frequency addressing method. Since it does not require any polarizer, the viewing angle is wide. This new reflective GH LCD is attractive for handheld displays. To make color displays, pixilated color filters should be implemented.

3.4 Reflective Dye-doped Negative LC (NLC) gels

We have demonstrated a polarizer-free reflective dye-doped DF LC gel. The contrast ratio is high, but the driving voltage ($\sim 30 V_{\text{rms}}$) is also higher than what TFT can afford. In order to effectively reduce the driving voltage, we need DF LC materials with a higher dielectric anisotropy at high frequency. However, it is difficult to obtain such materials, especially in TFT grade. In this part, we further reduce the driving voltage of GH LCD using a negative $\Delta\epsilon$ liquid crystal (NLC) gel¹⁵. The normally white dye-doped NLC gel exhibit $\sim 52\%$ reflectance, $\sim 200:1$ contrast ratios, ~ 5 ms response time, and $\sim 20 V_{\text{rms}}$ driving voltage. The black and white segmented reflective displays using such LC gels are also demonstrated.

3.4.1 Structure and Mechanism

The operating mechanism of the dye-doped NLC gel is similar to that of dye-doped DF LC gel. The structure and light modulation mechanisms of the dye-doped NLC gel are schematically depicted in Figure 41(a) and Figure 41(b). At $V=0$, the cell does not scatter light and the absorption is rather weak. Therefore, the display has the highest reflectance. When we apply a high voltage at $f=1$ kHz in the dye-doped NLC gel, the liquid crystals and dye molecules are reoriented in the x-y plane, as Figure 41(b) depicts. The polymer network scatters light strongly. Since the alignment layer has no rubbing treatment, the absorption has no preferred direction; therefore, the light scattering and dye absorption efficiency reaches their maxima. As a result, the display appears black.

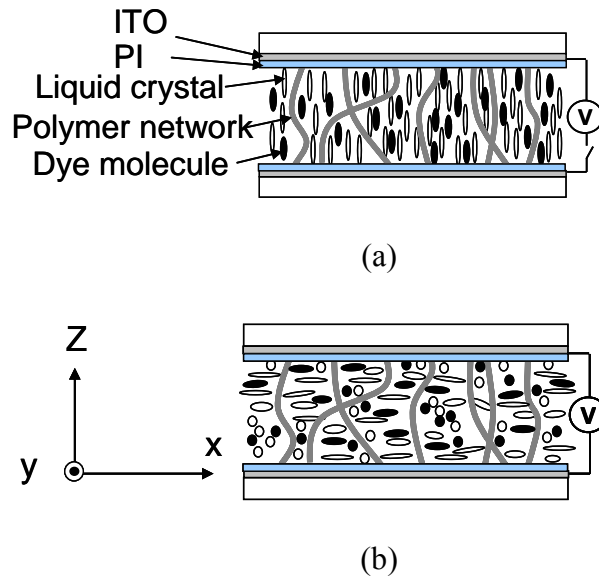


Figure 41: Operating principle of the dye-doped DF LC gel and dye-doped negative LC gel. (a) Voltage-off state, and (b) voltage-on state. The PI has no rubbing treatment.

3.4.2 Sample Preparation

For comparison purpose, two types of LC gels were fabricated: 1) DF LC and 2) negative $\Delta\epsilon$ LC (NLC). Our DF LC mixture has following physical properties: birefringence $\Delta n=0.267$ (at $\lambda=633$ nm, $T=21^\circ\text{C}$), crossover frequency $f_c=10$ kHz, and dielectric anisotropy $\Delta\epsilon= 7.72$ at $f= 1$ kHz and $\Delta\epsilon= -3.51$ at $f= 50$ kHz. The NLC we employed is ZLI-4788 (Merck, $\Delta n=0.1647$ at $\lambda=589$ nm; $\Delta\epsilon= -5.7$ at $f= 1$ kHz). We prepared two LC cells: one is dye-doped DF LC cell, and the other is dye-doped negative LC cell. We mixed the DF LC (or ZLI-4788) and a diacrylate monomer (bisphenol-A-dimethacrylate) with a dichroic dye S428 (Mitsui, Japan) at 90:5:5 wt % ratios. The dye-

doped DF LC mixture (or the dye-doped NLC mixture) was then injected into an empty cell whose inner surfaces were coated with a thin indium-tin-oxide (ITO) electrode and polyimide (PI) layer *without* rubbing treatment. The PI layer provides vertical alignment for the LC molecules. The cell gap was 5 μm . The filled cell was irradiated by a UV light ($\lambda \sim 365 \text{ nm}$, $I \sim 15 \text{ mW/cm}^2$). Both cells were cured at 13°C for 2 hr. After photopolymerization, the formed chain-like polymer networks are along the z direction because the LC directors are aligned perpendicular to the glass substrates during the UV curing process, as Figure 41(a) shows.

3.4.3 Electro-optical Properties

Because the guest-host system we employed appears dark red rather than black, we used a linearly polarized green diode laser ($\lambda = 532 \text{ nm}$) instead of a white light source for characterizing the device performances. A dielectric mirror was placed behind the cell so that the laser beam passed through the cell twice. A large area photodiode detector was placed at $\sim 25 \text{ cm}$ (the normal distance for viewing a mobile display) behind the sample which corresponds to $\sim 2^\circ$ collection angle. A computer controlled LabVIEW data acquisition system was used for driving the sample and recording the light reflectance.

Figure 42 plots the voltage-dependant reflectance of the dye-doped DF LC gel at $f = 50 \text{ kHz}$ (gray line) and dye-doped NLC gel $f = 1 \text{ kHz}$ (solid black line). These curves are independent of laser polarization. The reflectance is normalized to that of a pure DF LC cell or pure negative LC cell with the same cell gaps. The maximum reflectance is $\sim 52\%$ in the low voltage regime and decreases gradually as $V > V_{\text{th}}$ because the employed LC

has a negative $\Delta\epsilon$ and LC directors are in homeotropic structure at $V=0$. At $V=30 V_{\text{rms}}$, the measured contrast ratio of the dye-doped DF LC cell is as high as 190:1 at $f=50$ kHz. As to dye-doped NLC gel, it reaches the same contrast at $20 V_{\text{rms}}$ at $f=1$ kHz.

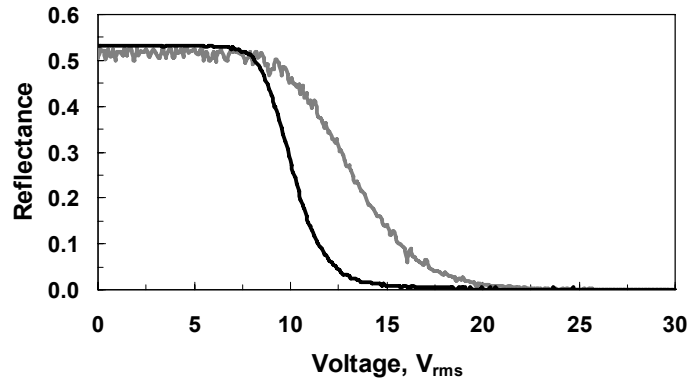


Figure 42: The voltage-dependent reflectance of the dye-doped DF LC gel at $f=50$ kHz (gray line), and the dye-doped NLC gel at $f=1$ kHz (black line). $\lambda=532$ nm.

3.4.4 Response Time

Response time is another important issue for guest-host displays. A typical response time of a guest-host display is around 50 ms. The response time of our dye-doped DF LC gel and dye-doped NLC gel is fast as shown in Figure 43 and Figure 44. If we fix the voltage at $30 V_{\text{rms}}$ while switching the frequency between 1 kHz and 50 kHz in the dye-doped DF LC gel, the rise time is ~ 0.93 ms and decay time is ~ 0.47 ms. For the dye-doped NLC gel, the rise time is 1.03 ms and decay time is 4.54 ms when the applied voltage is from 0 to $20 V_{\text{rms}}$ at $f=1$ kHz.

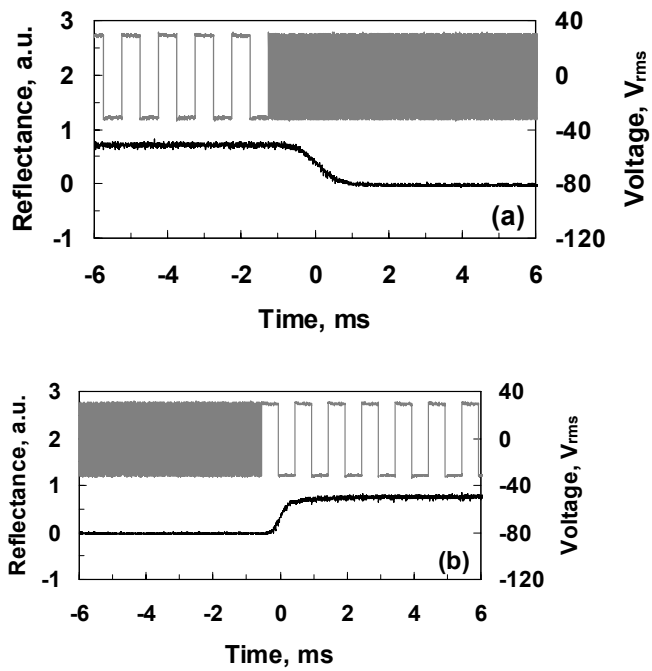


Figure 43: Response time of the dye-doped DFCLC gel.

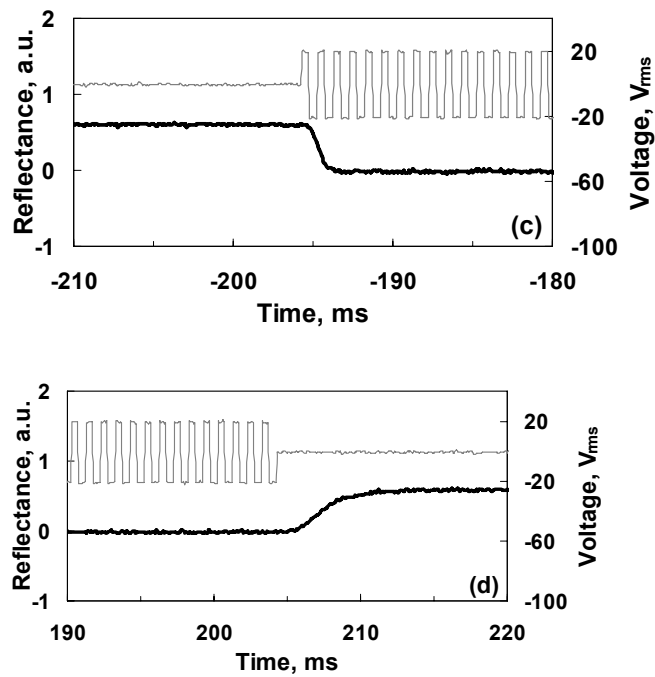


Figure 44: Response time of the dye-doped negative $\Delta\epsilon$ LC gel.

3.4.5 Reflective Dye-doped NLC gels

To prove principle, we also fabricated a segmented reflective display using the dye-doped NLC gel. To avoid specular reflection, we laminated a diffusive reflector on the backside of the bottom glass substrate in order to widen the viewing angle. The ambient white light was used to illuminate the samples. Figure 45 show the displays using a 4- μm dye-doped NLC gel. The bright segments represent the state of $V=0$. The dark areas represent the ITO electrodes with $V=20 V_{\text{rms}}$ at $f=1 \text{ kHz}$ in dye-doped NLC gel.

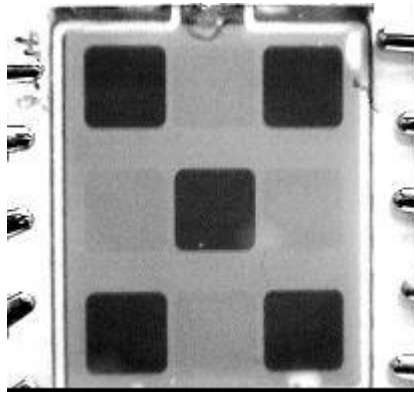


Figure 45: Displayed images using a reflective dye-doped NLC gel.

This dye-doped LC gel can also be used for polarizer-free transfective display as well. To match the electro-optic properties, the double cell gap approach should be implemented. The concept is shown in Figure 46. Since no polarizer is needed, the display should exhibit high optical efficiency and wide viewing angle. To lower the driving voltage, a high birefringence and high $\Delta\epsilon$ negative LC and slightly lower polymer concentration could be considered.

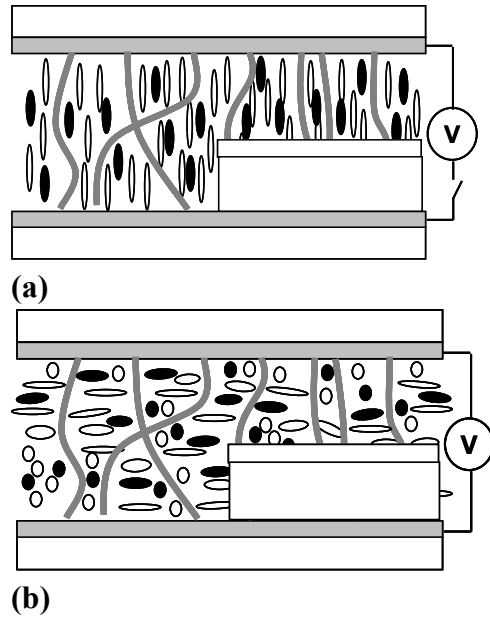


Figure 46: The concept of a polarizer-free transfective GH LCD using dye-doped LC gels.

3.4.6 Conclusion

We have demonstrated two high-contrast and polarization-independent reflective guest-host LCDs using dye-doped DFLC gel and dye-doped negative $\Delta\epsilon$ LC gel. The fabrication process is simple compared to the doubled layer GH LCDs. The response time is fast in dye-doped DFLC gel, but the driving voltage is high. Besides, DFLC has dielectric heating effect and usually the $\Delta\epsilon$ is small. The dye-doped negative LC gel is a more practical way for applications. The driving voltage is low in dye-doped negative LC gel; however, the tradeoff is the slightly slower response time. Since no polarizer is needed, the viewing angle is wide and the brightness is high in both cells. The new designs of polarizer-free guest-host LCDs are useful in electronic paper application and also have potential to be used in polarizer-free transfective LCD using double cell gaps.

CHAPTER 4: POLARIZATION INDEPENDENT LIQUID CRYSTAL PHASE MODULATORS

4.1 Introduction

Phase-only modulation can be used for tunable grating, prism, lens, and other photonic devices. Homogeneous alignment of liquid crystals (LCs) is commonly used for phase-only modulation,⁵⁰ although twisted nematic LC cells also exhibit such capability in the low voltage regime.⁵¹ For phase modulation using a homogeneous cell, the polarization axis (z-axis) of the input linearly polarized light (x-axis) is parallel to the LC directors. As the voltage exceeds a threshold, the LC directors are reoriented in the z-x plane. The phase change of the outgoing light varies with voltage as: $\Delta = 2\pi d[n_e(V) - n_o]/\lambda$; where d is the cell gap, $n_{e,o}$ is the refractive index of the extraordinary (or ordinary) ray, and λ is the wavelength. The major advantage of such a homogeneous cell is that a large phase change can be obtained with a relatively low voltage. However, the homogeneous cell is polarization dependent and its response time, which depends on d^2 , is typically ~ 10 ms for a $5 \mu\text{m}$ cell gap using a high birefringence LC operated at 70°C .⁵⁴

To achieve polarization-independent phase-only modulation and fast response time, nanosized polymer-dispersed liquid crystal (nano-PDLC) droplets have been explored.^{30,31,33,55-57} In a nano-PDLC system, the LC droplets dispersed in the polymer

matrix are randomly oriented. Since the LC droplet size is smaller than a visible wavelength, the light scattering is almost completely suppressed and the nano-PDLC acts as a phase retarder in the voltage-off state. As the voltage increases, the LC directors within the droplets are reoriented along the electric field direction and, therefore, induce a phase shift. Because of the small LC concentration (~35%) and random droplets distribution, the available phase change is fairly small. Despite this small phase change, nano-PDLC has potential applications for phase gratings, micro-prisms, microlens arrays, color filters, and color displays. A critical issue of the nano-PDLC is high operating voltage (~10 V/ μm). For a 20 μm cell gap, the required voltage is ~200 V_{rms} .

Unlike nano-PDLC, the conventional PDLC²⁶ has a larger droplet size (~1 μm) and higher LC concentration (~70%). As a result, PDLC exhibits a lower saturation voltage (~2-3 V/ μm) than nano-PDLC. However, in the voltage-off state, PDLC strongly scatters visible light because its droplet size is comparable to the wavelength and its average refractive index mismatches with that of polymer matrix. The phase modulation property of PDLC has been investigated previously.²⁹ It was found that phase shift coexists with light scattering, but depends on the incident light polarization and incident angle. For the normally incident light, PDLC does not possess any phase change when the applied voltage is below the saturation voltage (V_{sat}).

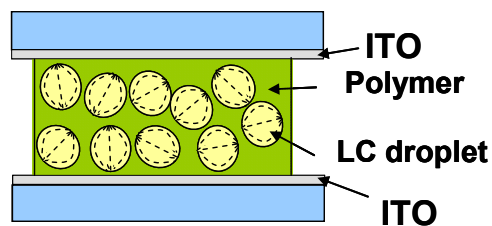
4.2 Polarization Independent LC Phase Modulators Using PDLC

In this part, we find that the phase-only modulation using PDLC for the normally incident light exists in the high voltage region ($V > V_{\text{sat}}$). Moreover, such a phase shift is polarization independent and has fast response time. Although the remaining phase

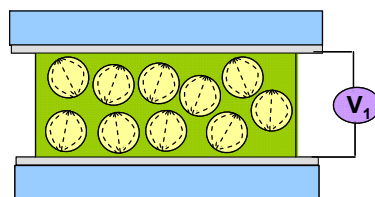
change is not too large, it is still sufficient for making micro-devices, such as microprisms and microlens. For feasibility demonstration, we fabricate a two-dimensional tunable-focus microlens arrays using PDLC. In comparison to nano-PDLC, PDLC has a lower operating voltage.

4.2.1 Mechanism

Figure 47 illustrates the phase modulation mechanism of a PDLC. In Figure 47(a), the LC droplets (or domains) are randomly dispersed in polymer matrix. Because of the refractive index mismatch, light scattering is strong. As the applied voltage increases, the LC directors are reoriented along the electric field direction. As a result, PDLC becomes transparent, as shown in Figure 47(b). If the voltage is increased further, more LCs in the droplet cavities are reoriented by the electric field, as shown in Figure 47(c). From Figure 47(b) to Figure 47(c), phase-only modulation is still available and is independent of polarization for the normally incident light.



(a)



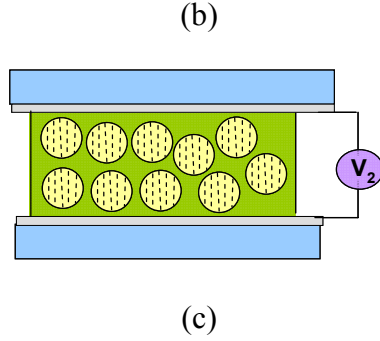


Figure 47: LC droplet orientations in a PDLC film at (a) $V=0$, (b) V_1 , and (c) $V_2 > V_1$.

4.2.2 Sample Preparation

To prepare a PDLC cell, we mixed nematic LC E48 ($n_o=1.523$, $\Delta n=0.231$) with a UV-curable monomer NOA65 (refractive index $n_p=1.524$) at 84:16 wt % ratios. Here, we intentionally used a higher LC concentration in order to obtain a larger phase change at a lower voltage. The conventional PDLC with ~65:35 LC/monomer ratios would work equally well but the required voltage is higher. The LC/monomer mixture was injected into an empty cell whose inner surfaces were coated with a thin indium-tin-oxide (ITO) electrode. The cell gap was measured to be $d=22 \mu\text{m}$. The filled cell was then exposed to UV light ($\lambda \sim 365 \text{ nm}$, $I \sim 15 \text{ mW/cm}^2$) at room temperature for 30 min to induce phase separation.

We observed the phase separation morphology of the PDLC sample using a polarized optical microscope. The formed morphology indicates that the LC dispersed in polymer matrix exists as domains separated by polymer networks rather than isolated LC

droplets. This kind of morphology is common for the PDLC system having a high LC concentration.⁴

4.2.3 Experimental Setup

Next, we measured the transmittance of the PDLC cell using a He-Ne laser ($\lambda=633$ nm) beam. A large area photodiode detector was placed at ~ 30 cm behind the sample which corresponds to $\sim 2^\circ$ collection angle. A computer controlled LabVIEW data acquisition system was used for driving the sample and recording the light transmittance.

4.2.4 Electro-optical Properties

Figure 48 plots the measured voltage-dependent transmittance of the PDLC sample. At $V=0$, the PDLC sample is translucent so that the transmittance is low. As the voltage increases, the transmittance increases. From Figure 48, the measured contrast ratio is $\sim 9:1$, which is lower than a typical PDLC because of the larger domain size which originates from the higher LC concentration. When the applied voltage exceeds $26 V_{\text{rms}}$, the transmittance remains basically unchanged. We define this voltage as saturation voltage (V_{sat}). At $V > V_{\text{sat}}$, the PDLC cell remains highly transparent. For each cell, the saturation voltage could vary because it depends on the cell gap, LC material, and monomer concentration.

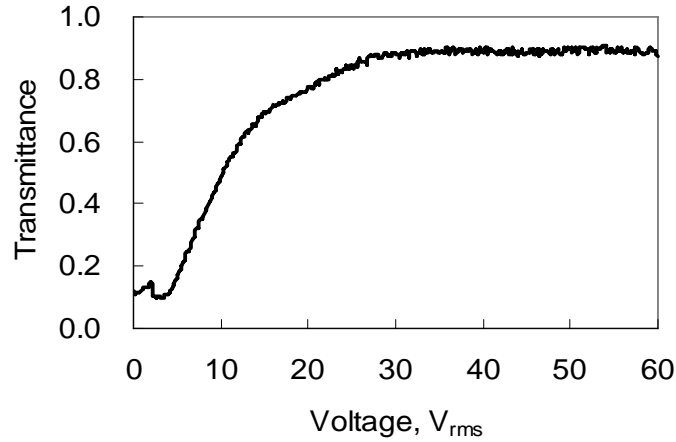


Figure 48: Voltage-dependent transmittance of a PDLC film. $\lambda=633$ nm and cell gap $d=22$ μm .

4.2.5 Phase Shift

To measure the phase shift of residual phase type polarization independent LC phase modulator, we can put the LC cell between two polarizers. By measuring the transmittance under parallel and crossed polarizers, the phase change can be calculated from Eq. (25) as:

$$\delta = 2 \tan^{-1} \sqrt{T_{\perp} / T_{\parallel}} , \quad (25)$$

where T_{\perp} and T_{\parallel} represent the transmittance at the crossed- and parallel-polarizer configurations, respectively.

To examine whether the PDLC film exhibit a phase-only modulation capability in the high voltage regime, we measured its transmittance at $\lambda=633$ nm between parallel and crossed polarizers. Results are shown in Figure 49. The transmittance increases for the parallel polarizer configuration, while decreases gradually for the crossed polarizers in

the $V > V_{\text{sat}}$ region. These results imply that PDLC can produce phase-only modulation when the applied voltage is higher than the saturation voltage. Moreover, rotating the sample does not affect the measurement results shown in Figure 49. This indicates that the phase-only modulation is independent of the incident light polarization. In the high voltage state, the LC directors are basically perpendicular to the substrates, similar to a homeotropic cell. The input linearly polarized light always sees the ordinary refractive index, regardless of its polarization axis. Thus, the phase modulation is independent of the incident light polarization.

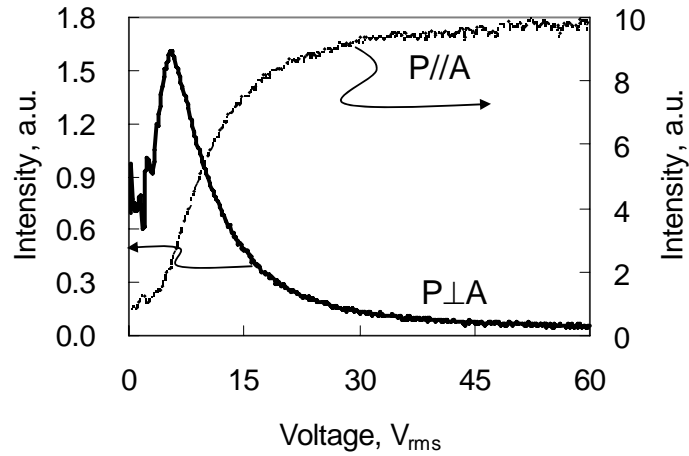


Figure 49: Voltage-dependent transmittance of a PDLC cell between parallel (right ordinate) and crossed (left ordinate) polarizers. $f=1$ kHz, $\lambda=633$ nm, and cell gap $d=22$ μm .

From Figure 49, the saturation voltage of the PDLC sample is ~ 1.2 V/ μm , which is ~ 10 X lower than that of a nano-PDLC. The phase change (δ) of the PDLC sample can be calculated using the Eq.(25).

Figure 50 plots the measured voltage-dependent phase change of the PDLC cell. From 26 to 60 V_{rms} , δ decreases gradually because the LC directors inside the droplets continue to be reoriented by the electric field, as schematically shown in Figure 47(c).

Although the phase change is small, it is still sufficient for making microlens arrays. To increase the phase difference, several approaches can be implemented, for instance, to use a high birefringence LC material, increase LC cell gap, or enhance LC concentration.

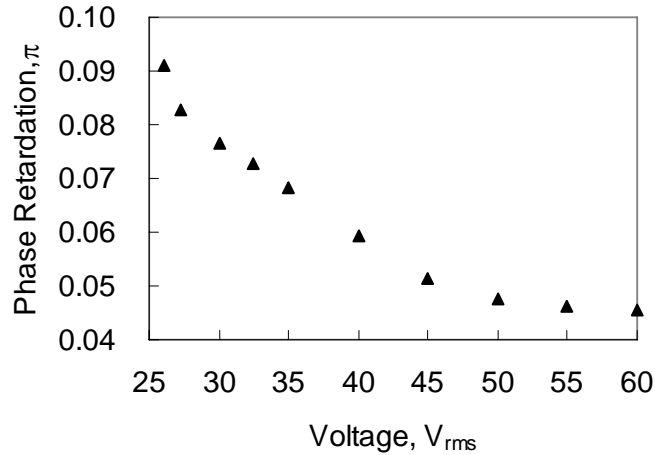


Figure 50: Measured phase shift of the PDLC cell at different voltages. Cell gap $d=22\mu\text{m}$.

4.2.6 Response Time

Response time is a very important parameter for almost every LC device. We measured the PDLC response time using a square voltage burst at $f=1$ kHz between 26 and 55 V_{rms} . The measured rise time is ~ 0.8 ms and decay time ~ 1.9 ms at room temperature. Such a fast response time results from the high bias voltage effect.

4.2.7 Application: Microlens Arrays using PDLC

To demonstrate the usefulness of the observed phase change, we fabricated a 2D microlens arrays using the PDLC as electro-optic medium. We first used a lamination

method to prepare polymer microlens arrays.⁵⁹ The polymer material used is NOA65 ($n_p=1.524$). The thickness and diameter of the formed microlens is $\sim 50 \mu\text{m}$ and $450 \mu\text{m}$, respectively. Afterwards, we filled the polymer microlens array cavities with the NOA65/E48 mixture. The cell was then sealed with a top ITO-glass substrate. Finally, we cured the sealed cell using a UV light. The UV curing condition is the same as mentioned above.

Figure 51(a) and Figure 51(b) show the patterned polymer microlens arrays before and after filling the PDLC material. These two photos were taken under a polarized optical microscope. From Figure 51(a), each circular ring corresponds to a concave lens of $\sim 450 \mu\text{m}$ diameter and lens pitch $\sim 20 \mu\text{m}$. In Figure 51(b), the filled circular region is translucent due to light scattering.

To characterize the focusing properties of the microlens, we illuminated the lens arrays with a collimated unpolarized He-Ne laser beam. The transmitted light was detected by a CCD camera. Figure 52 shows the images of the focused spots produced by the microlens arrays at different voltages. At $V=0$, the focusing effect is obscured because of strong light scattering. At $V=70 \text{ V}_{\text{rms}}$, the focal spots appear but not very sharp. At $V=140 \text{ V}_{\text{rms}}$, the focus is at image plane. Thus, the light intensity increases noticeably. This result means that the patterned microlens arrays have a tunable focal length in the high voltage regime. If we increase the voltage from 70 to 180 V_{rms} , the focal length is tuned continuously from $\sim 8 \text{ cm}$ to $\sim 12 \text{ cm}$. In principle, if the LC and polymer have a similar ordinary refractive index, the focal length of the polymer/PDLC microlens should reach infinity in the high voltage regime. The focal length of a microlens is dependent on the lens radius, LC birefringence, and lens thickness. If we

want to reduce the focal length, we could reduce the lens diameter, use a higher birefringence LC, or increase the lens thickness.

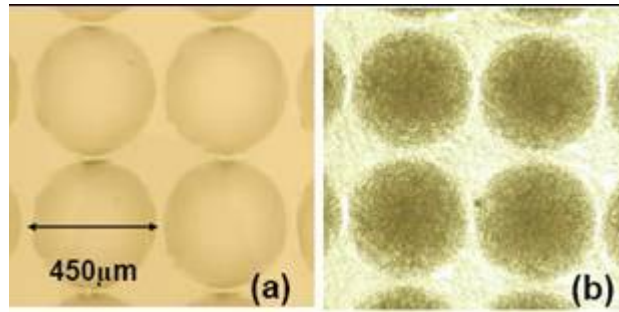


Figure 51: Microscope photos of (a) concave polymer microlens arrays, and (b) polymer/PDLC microlens arrays.

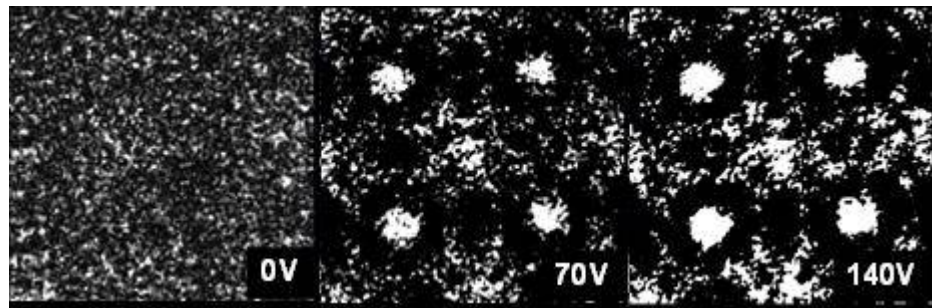


Figure 52: Measured CCD images of the 2D microlens arrays at different voltages: (a) $V=0$, (b) $V=70 V_{\text{rms}}$, and (c) $V=140 V_{\text{rms}}$.

4.2.8 Discussion and Conclusion

In comparison with other tunable LC phase modulators, PDLC exhibits a relatively small phase change. This is because the phase phenomenon only exists in the high voltage regime where the LC orientation is close to the saturation level. However, the phase modulation using PDLC is polarization independent, scattering-free, and has

fast response time. The operating voltage is lower than that of nano-PDLC system. Although the tunable phase shift is small, it is still sufficient for some micro-devices.

In conclusion, we have demonstrated the phase modulation capability using a PDLC film which only exists in the high voltage regime. Such a phase modulation is scattering-free, polarization independent, and has fast response time. Although the phase change is small, it is still sufficient for making tunable-focus microlens arrays.

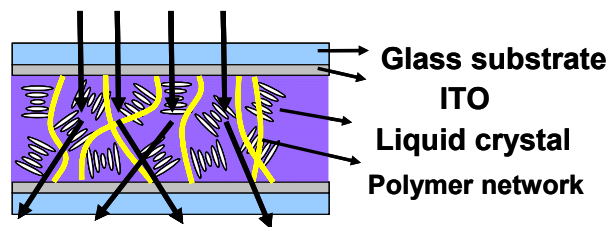
4.3 Polarization Independent LC Phase Modulators Using Polymer Stabilized Cholesteric Textures (PSCT)

In this part, we find another polarization-independent phase modulation mechanism using a polymer-stabilized cholesteric texture (PSCT)¹⁹. PSCT has been studied for display and privacy window applications for more than a decade.^{60,5} Both normal-mode⁶¹ and reversed-mode^{36,62-65} PSCT devices have been developed. Usually a normal-mode PSCT is operated at a voltage below the saturation voltage where the maximum transmittance is first reached. In this paper, we find a small phase modulation is available in the $V > V_s$ region. Moreover, this phase change is polarization-independent, hysteresis-free, and has sub-millisecond response time. To demonstrate the usefulness of this polarization-independent phase modulation, we fabricated a microlens arrays based on the abovementioned PSCT. The focal length is tunable from 3.5 cm to 5 cm when the voltage is switched from 180 to 80 V_{rms} .

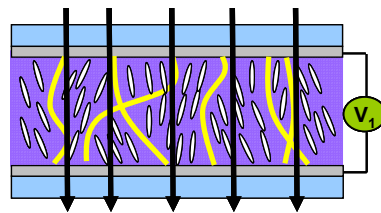
4.3.1 Mechanism

Figure 53 illustrates the operation mechanism of a normal-mode PSCT. To achieve a normal-mode operation, the LC cell was illuminated by an UV light in the homeotropic state with the presence of a bias voltage (40 V_{rms}). When the polymerization process is completed, the applied voltage is removed and then the focal conic texture is formed owing to the competition between the intrinsic spiral structure and the polymer constraint, as shown in Figure 53(a). In this state, the cell is translucent because of strong

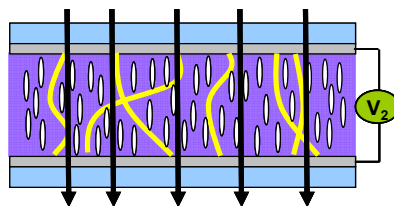
light scattering originated from the poly-domain focal conic structures. As the voltage reaches the saturation voltage, the electric field unwinds and transforms the spiral LC structures into a nearly homeotropic state. Under such a circumstance, the PSCT cell is transparent, as shown in Figure 53(b). As the voltage exceeds V_s , more LC directors are aligned vertically, as shown in Figure 53(c). Although the phase change between Figure 53(b) and Figure 53(c) is small, it is scattering-free, polarization independent, hysteresis-free and has a fast response time.



(a)



(b)



(c)

Figure 53: The operation mechanism of PSCT at (a) $V=0$, (b) $V_1 \sim V_s$, and (c) $V_2 > V_1$. The residual phase between (b) and (c) can be used for phase modulator.

4.3.2 Sample Preparation

To prepare a normal-mode PSCT cell, we mixed nematic LC E44 ($\Delta n=0.26$, Merck), CB15 (a chiral agent), and a diacrylate monomer (bisphenol-A-dimethacrylate) at 90.25: 5.75: 4 wt % ratios. The mixture was injected into an empty cell whose inner surfaces were coated with a thin indium-tin-oxide (ITO) electrode only. The cell gap was controlled at $d=25 \mu\text{m}$. During UV exposure, the filled cell was biased at $V=40 V_{\text{rms}}$ (1 kHz sinusoidal waves) so that the LC directors and monomer were reoriented nearly perpendicular to the substrates. The UV ($\lambda\sim 365 \text{ nm}$) intensity was controlled at $I\sim 15 \text{ mW/cm}^2$ and exposure time was 1 hr. The UV curing process took place at room temperature ($T\sim 23^\circ\text{C}$).

4.3.3 Electro-optical Properties

In experiment, we measured the transmittance of the PSCT cell using an unpolarized He-Ne laser ($\lambda=633 \text{ nm}$) beam. No polarizer was used. A large-area photodiode detector was placed at $\sim 30 \text{ cm}$ behind the sample, which corresponds to $\sim 2^\circ$ collection angle. A computer-controlled LabVIEW data acquisition system was used for driving the sample and recording the light transmittance. Figure 54 plots the voltage-dependant transmittance of the normal-mode PSCT. The PSCT shows a severe hysteresis effect when the voltage is ramped up (black line) and down (dotted line). In the low voltage regime, the PSCT scatters light strongly so that the transmittance is low and the sample appears translucent. As the voltage reaches the saturation voltage $V_s\sim 40 V_{\text{rms}}$, the PSCT cell becomes highly transparent. In general, the saturation voltage is determined by

the chiral dopant and monomer concentration, LC material, and cell gap. As shown in Figure 54, the hysteresis is negligible when $V \geq V_s$.

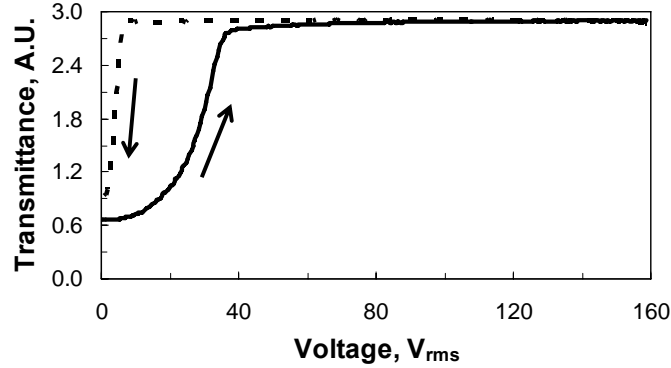


Figure 54: The voltage-dependant transmittance of a PSCT cell with increasing voltage (black line) and decreasing voltage (dotted line).

4.3.4 Response Time

Next, we measured the response time of our PSCT phase modulator by using a square-wave voltage burst at $f=10$ kHz between 40 and 160 V_{rms} . The measured rise time is ~ 75 μs and decay time ~ 793 μs . The very fast rise time originates from the high operating voltage (160 V_{rms}) and the sub-millisecond decay time from the relatively high bias voltage (40 V_{rms}) and the twist power of the chiral dopant and the polymer network.

4.3.5 Phase Change

To characterize the phase change of PSCT, we measured the transmittance of the PSCT cell under crossed- and parallel-polarizer conditions. Results are plotted in Figure 55. Below 40 V_{rms} , the cell scatters light. Beyond 40 V_{rms} , the transmittance (T_{\perp}) for the

crossed polarizers gradually decreases and T_{\parallel} increases for the parallel polarizers. This is clear evidence that the phase modulation exists when the applied voltage exceeds the saturation voltage. Besides, when we rotate the PSCT cell between the polarizers, the transmittance curves remain unchanged. That means the PSCT phase modulator is indeed polarization independent.

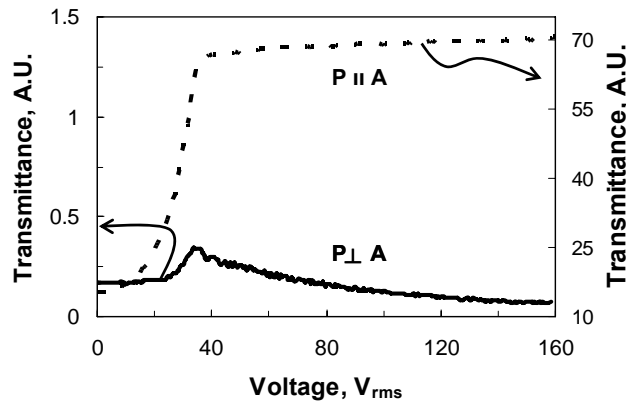


Figure 55: The voltage-dependant transmittance of a PSCT cell between crossed polarizers (black line, left ordinate) and parallel polarizers (dotted line, right ordinate). $f=1$ kHz, $\lambda=633$ nm, and cell gap $d=25$ μm .

The phase change (δ) of the PSCT cell can be calculated from Eq (25). Figure 56 depicts the measured voltage-dependent phase change of the PSCT cell. The available phase decreases gradually with increased voltage because the LC directors are continuously reoriented by the electric field, as schematically shown in Figure 53(c). The total phase change between 40 and 160 V_{rms} is $\sim 0.025\pi$. A higher voltage is required for getting more phase change. Although the residual phase change is small, it is still useful for making micro devices, such as microlens arrays, micro-grating, and micro-prism.

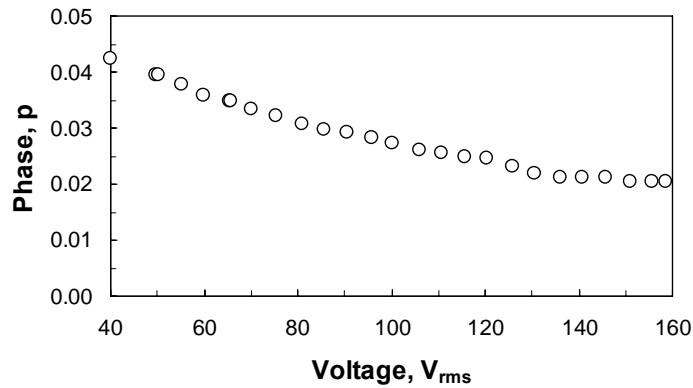


Figure 56: Measured voltage-dependent phase shift of the E44 PSCT cell we prepared. Cell gap $d = 25 \mu\text{m}$.

The residual phase can be increased by using a higher birefringence LC, larger cell gap, higher LC concentration, or higher curing temperature. The first two factors are obvious, but the last two need some explanations. Based on our experimental results, the phase can be boosted by $\sim 2X$ as we increase the LC concentration from 90.25 to 93.61 wt% while reducing the chiral dopant from 5.75 to 3.39 wt% and polymer from 4 to 3 wt%. The reduction of chiral dopant and polymer lowers the saturation voltage. As a result, the remaining phase increases. The tradeoff is the increased hysteresis. The curing temperature also has an important effect on the residual phase. At a given curing voltage, the domain size increases as the curing temperature increases³⁴ which, in turn, lowers the saturation voltage. Therefore, the remaining phase increases. Our experimental results show that the phase is increased by $\sim 2-3X$ when the curing temperature is increased by $\sim 20^\circ\text{C}$.

4.3.6 Application: Microlens Arrays

To demonstrate the usefulness of this small residual phase change, we made a two-dimensional (2D) microlens array using the normal-mode PSCT as electro-optics medium. The fabrication method is similar to that reported earlier.⁵⁹ First, we used the lamination method to prepare a polymer microlens arrays with NOA65 (Norland, $n_p=1.524$). The radius of curvature and the radius of aperture of each microlens are ~ 950 μm and 222 μm , respectively. Second, we filled our LC/polymer/chiral mixture into the polymer microlens array cavities. Third, the cell was sealed with a top ITO-glass substrate. Finally, the cell was biased at ~ 140 V_{rms} during the UV curing process.

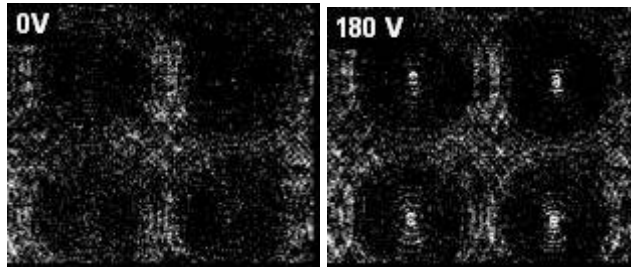


Figure 57: Measured CCD images of 2D microlens arrays at $V=0$ and $V=180$ V_{rms} .

To characterize the focusing properties, a collimated unpolarized He-Ne laser beam was used to illuminate the PSCT microlens arrays and then a CCD camera was used for detecting the transmitted light. The focusing properties of the PSCT microlens arrays at 0 and 180 V_{rms} are shown in Figure 57. At $V=0$, the imaging property is obscured because of the strong light scattering. At $V=180$ V_{rms} , clear focal spots appear. Moreover, the focal length of the patterned microlens arrays is tunable by the applied voltage. The focal length is 3.5 cm at $V=180$ V_{rms} and increases to 5 cm at $V\sim 80$ V_{rms} .

Based on this result, we can calculate the effective refractive index of the PSCT using the following equation:

$$f = R^2 / 2d(n_{eff} - n_p), \quad (26)$$

where f is focal length of the lens, R is the radius of the microlens aperture, d is the LC thickness (the maximum thickness is $\sim 26 \mu\text{m}$), and n_{eff} is the effective refractive index of the PSCT. Plugging in the known values of f , R , d , and n_p to Eq. (26), we find $n_{eff} \sim 1.551$ at $180 \text{ V}_{\text{rms}}$. This value is reasonable because it should satisfy the following relationship: $n_0 < n_{eff}(V_{\text{rms}}) < (2n_0 + n_e)/3$, where $n_0 = 1.53$ and $n_e = 1.79$. From the above equation, the focal length of a microlens depends on the lens radius and thickness, and the LC effective birefringence. To obtain a shorter focal length, we could reduce the lens diameter, use a higher birefringence LC, or increase the LC lens thickness. The shortcoming of using a thick LC layer is the increased operating voltage. A simpler solution is to employ a high birefringence and low threshold voltage PSCT.

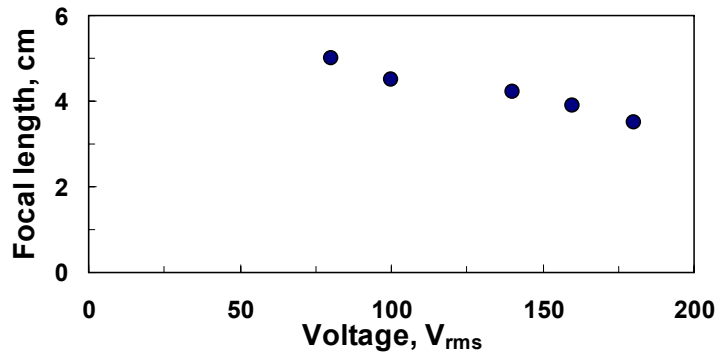


Figure 58: Voltage-dependent focal length of the PSCT-based 2D microlens arrays.

Figure 58 plots the voltage-dependent focal length of the PSCT microlens arrays. The focal length of our lens array is polarization-independent and is tunable from 3.5 cm to 5 cm when the voltage is switched from 180 to 80 V_{rms}.

The PSCT-based phase modulator exhibits a ~4X lower threshold voltage (~1.6 V/ μ m) than the nano-PDLC phase modulator⁵⁷ (~6 V/ μ m) because of its larger domain size. The response time is somewhat slower but still comparable to that of nano-PDLC phase modulators. In comparison to a conventional PDLC phase modulator,¹⁸ the PSCT exhibits a faster response time because the chiral dopant provides an extra force to assist the LC relaxations. However, it is also due to the chiral dopant the PSCT threshold voltage is higher than that of a PDLC phase modulator.

4.3.7 Conclusion

We have demonstrated a polarization-independent, scattering-free, hysteresis-free, and fast-response PSCT-based phase modulator. Although the operating voltage is high and the residual phase is small, the PSCT is still useful for making micro-devices. A PSCT-based tunable-focus microlens arrays is demonstrated.

4.4 Polarization Independent LC Phase Modulators Using Homeotropic LC gels

We have demonstrated two polarization-independent phase modulators using a conventional PDLC layer and PSCT. To bypass the light scattering regime, a bias voltage is applied to both PDLC and PSCT cells. However, the bias voltage is too high in PSCT because of the chiral dopant. In PDLC, because the average LC droplet size is larger than the visible wavelength, the operating voltage (3 V/ μm) is lower than PSCT. Meanwhile, the response time is fast (~ 1 ms) benefiting from the bias voltage effect. However, due to the bias voltage effect the remaining tunable phase change is relatively small ($\sim 0.04\pi$) in PDLC. Although the observed small phase change is still usable for microphotonic devices, it is highly desirable to increase the phase shift and decrease the operating voltage while keeping a fast response time.

In this part, we demonstrate a homeotropic LC gel²⁰ whose phase shift is larger but operating voltage is lower than a nano-PDLC. The larger phase change and lower operating voltage originate from the higher LC concentration in our gel. Different from a conventional LC gel,⁶⁶ our LC domain size is in submicron region so that the light scattering is completely suppressed in the voltage-off state.

4.4.1 Mechanism

Figure 59(a), (b), and (c) show the schematic configurations of the LC directors and polymer networks in the voltage-off ($V=0$), threshold (V_{th}) for directors reorientation,

and light scattering states ($V_s > V_{th}$) of the homeotropic LC gel. In Figure 59(a) where $V=0$, the LC directors are aligned nearly perpendicular to the substrates and stabilized by polymer gels. The polymer networks are formed along the same orientation as the LC directors. Because of the small domain sizes and good index match, the LC gel is highly transparent. As the applied voltage exceeds a threshold, the LC directors begin to tilt away from the electric field direction, as shown in Figure 59(b), because the LC has a negative dielectric anisotropy ($\Delta\epsilon < 0$). Further increasing voltage to V_s , light scattering occurs because the refractive index mismatch between the LC and the polymer gel, as shown in Figure 59(c). From Figure 59(b) to 64(c), phase-only modulation is expected. Due to the random reorientation of the LC directors in the polymer networks, the phase shift is polarization independent for the normally incident light.

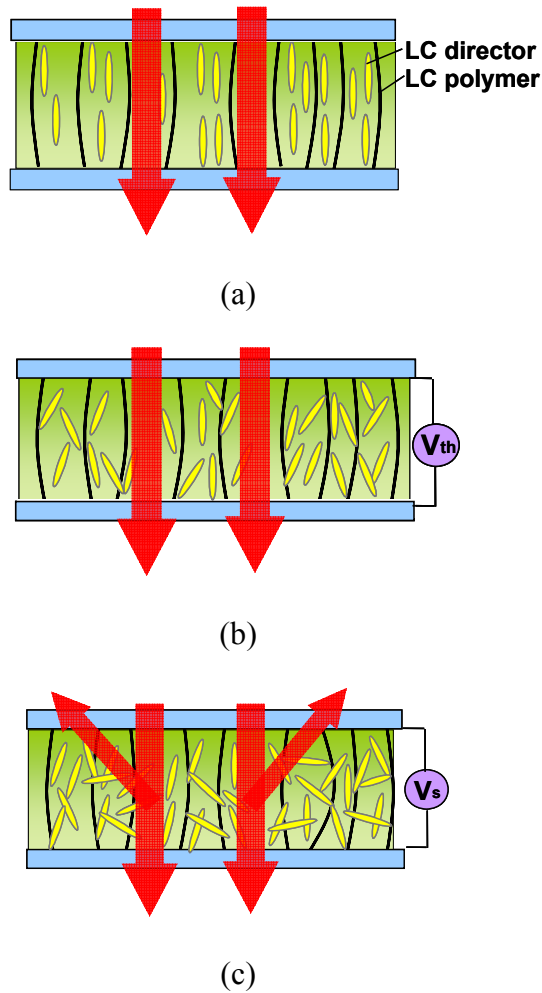


Figure 59: Schematic diagrams of polymer and LC directors orientations of a homeotropic LC gel: (a) $V=0$, (b) $V=V_{th}$ where the LC directors reorientation starts, and (c) $V=V_s$ where the light scattering takes place.

4.4.2 Sample Preparation

To prepare a homeotropic LC gel with small LC domain sizes, we mixed 20 wt% of a Merck photocurable LC diacrylate monomer RM257 in a negative nematic LC MLC-6608 ($\Delta n=0.083$, $\Delta \epsilon=-4.2$). The LC/monomer mixture was injected into an empty cell in the isotropic state. The inner surfaces of the indium-tin-oxide (ITO) glass

substrates were coated with thin homeotropic polyimide alignment layers and rubbed in orthogonal directions in order to reduce the polarization dependency originating from the boundary layers. The pretilt angle is $\sim 88^\circ$ on each surface. The filled cell was then slowly cooled down to room temperature and exposed to UV light ($\lambda \sim 365$ nm, $I \sim 10$ mW/cm²). The UV curing time for the cell was ~ 30 min. The cell gap was controlled at ~ 23 μm using two stripes of mylar film.

4.4.3 Electro-optical Properties

The electro-optic properties of the LC gel was characterized using an unpolarized He-Ne laser beam ($\lambda = 633$ nm). The transmitted light was measured by a photodiode detector which was placed at ~ 30 cm behind the sample. A computer controlled LabVIEW data acquisition system was used for driving the sample and recording the light transmittance. The response time of the LC gel was recorded by a digital oscilloscope.

The LC gel sample appears slightly bluish as visually observed in the reflection state, which implies that the formed LC domain size is comparable to a blue wavelength ($\lambda \sim 400$ nm). The LC gel is highly transparent at the He-Ne laser wavelength ($\lambda \sim 633$ nm).

Figure 60 plots the voltage-dependent transmittance of the LC gel. The LC gel is highly transparent at $V=0$. Below $180V_{\text{rms}}$, the transmittance remains at $\sim 88\%$. The $\sim 12\%$ light loss mainly originates from the interface reflections between the ITO-glass substrates and the air. The refractive index of ITO is ~ 1.90 . As the voltage exceeds

$180V_{\text{rms}}$, the transmittance begins to decline due to light scattering. Therefore, we define $180V_{\text{rms}}$ as the V_s of the LC gel. The relatively high V_s is due to the small $\Delta\epsilon$ and small Δn of the LC mixture employed, and the submicron domain sizes due to high (20%) polymer concentration. The hysteresis of the voltage-dependent transmittance of the LC gel was also measured. Results indicate that the forward and backward curves overlap very well, which means the hysteresis is completely suppressed.

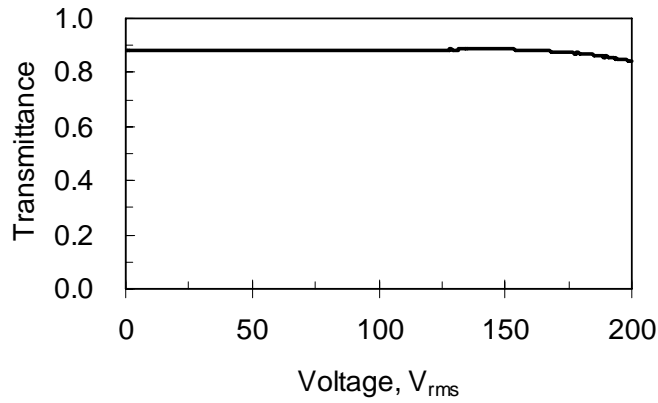


Figure 60: Voltage-dependent transmittance of the LC gel. $d=23\mu\text{m}$. An unpolarized He-Ne laser was used for this measurement.

To examine the phase modulation capability of the LC gel, we measured the transmittance (T_{\parallel} and T_{\perp}) at $\lambda=633\text{ nm}$ between parallel and crossed polarizers with the beam normally incident on the sample surface. We set the polarization axis of the analyzer parallel to one rubbing direction of the cell. Results are shown in Figure 61. Due to the homeotropic alignment of the LC gel, $T_{\perp} \sim 0$ at $V=0$. As the applied voltage exceeds the threshold voltage $V_{\text{th}}=130V_{\text{rms}}$, T_{\parallel} decreases but T_{\perp} increases with voltage gradually. This means phase-only modulation exists. At $V>180V_{\text{rms}}$, light scattering takes

place which is not desirable for the phase-only modulation. To validate whether the gel is polarization dependent, we rotated the sample in the azimuthal direction. Results remain unchanged. This indicates that the phase-only modulation is independent of incident light polarization.

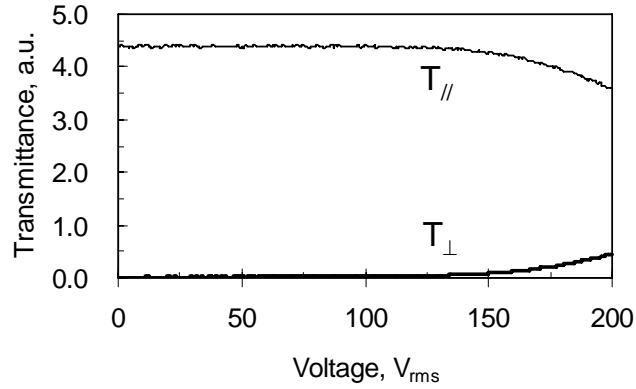


Figure 61: Voltage-dependent transmittance of the LC gel between parallel ($T_{//}$) and crossed (T_{\perp}) polarizers. Cell gap $d=23\mu\text{m}$, $f=1$ kHz, $\lambda=633$ nm, and $T\sim 21$ °C.

4.4.4 Response Time

Response time is another important parameter for LC based phase modulator. We measured the response time of the LC gel using square voltage bursts at $f=1$ kHz between 0 and $180V_{rms}$. The measured rise time is $\tau_{rise} \sim 590$ μs and decay time $\tau_{decay} \sim 150$ μs at room temperature. Such a fast response time results from the small LC domain size as well as the strong polymer stabilization effects. Based on the measured decay time, we estimate the domain size is around 300 nm. This is consistent to the very weak bluish appearance of the LC gel.

4.4.5 Phase Change

The phase change in the range from 0~180V_{rms} can be calculated from Eq (25). Figure 62 plots the voltage dependent phase change of the LC gel at $\lambda=633$ nm and T~21 °C. As the voltage increases, the phase increases gradually because the LC directors inside the domains are reoriented randomly away from the electric field, leading to an increased effective birefringence. From 130 to 180V_{rms}, the phase shift is $\Delta\delta \sim 0.08 \pi$ (for the 23 μm LC gel) which is 2X larger than our previous results using a conventional PDLC.¹⁸

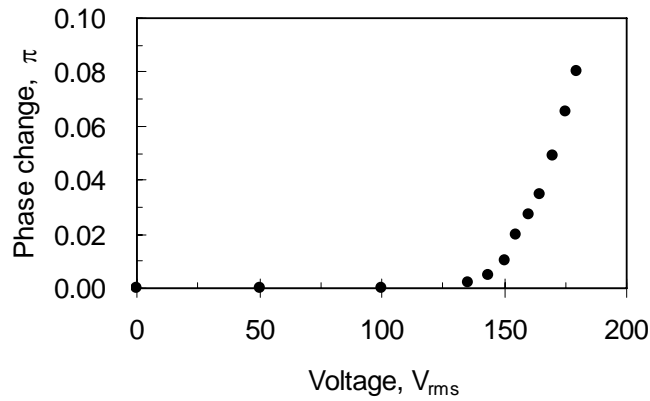


Figure 62: Measured phase shift of the LC gel at different voltages. $d=23 \mu\text{m}$ and $\lambda=633$ nm

In our LC gel, the effective refractive index at $V=0$ can be expressed as

$$n_{o-eff} = \frac{v_{LC}n_o + v_p n_p}{v_{LC} + v_p}, \quad (27)$$

where n_o is the ordinary refractive index of the LC, v_{LC} and v_p are the LC and polymer volume fractions, and n_p is the refractive index of the polymer. By applying a voltage across the LC gel, the LC directors tend to reorient themselves perpendicular to the electric field because of the negative $\Delta\varepsilon$. Therefore, light impinging on the sample at normal incidence will see an average refractive index increased from n_o to $\bar{n}(V)$. In this case, the effective refractive index of the LC gel can be rewritten as

$$n_{eff} = \frac{v_{LC}\bar{n}(V) + v_p n_p}{v_{LC} + v_p}, \quad (28)$$

As a result, the field-induced phase shift can be expressed as

$$\Delta\delta = \frac{2\pi}{\lambda} d(n_{eff} - n_{o-eff}), \quad (29)$$

where d is the cell gap and λ is the incident wavelength. By combining Eqs. (27) and (29), we rewrite the phase shift as follows:

$$\Delta\delta = \frac{2\pi}{\lambda(v_{LC} + v_p)} dv_{LC}(\bar{n}(V) - n_o), \quad (30)$$

From Eq. (30), the LC volume fraction (v_{LC}) is an important parameter contributing to the phase change because $v_{LC} + v_p$ does not change. In our gel system, the LC concentration is $\sim 80\%$ which is much higher than that in a nano-PDLC ($\sim 30\%$). As a result, our LC gel should exhibit a larger phase shift than the nano-PDLC, if the same Δn is employed.

From Figure 62, the 0.08π phase change was obtained at $V = 180V_{rms}$ which corresponds to $7.8 V/\mu m$. Two factors affecting the on-state voltage are $\Delta\varepsilon$ of the LC mixture and LC concentration. Negative LC mixtures tend to have a smaller $\Delta\varepsilon$ than their

positive counterparts. A nano-PDLC device usually uses a positive, large $\Delta\epsilon$ LC mixture in order to suppress its operating voltage. Although our LC gel uses a negative, small $\Delta\epsilon$ LC mixture, its required electric field strength is still lower than that of a nano-PDLC because of the higher LC concentration involved. A higher LC concentration not only leads to a slightly larger LC domain size but also decreases the contact interface between the polymer binder and the LC molecules. As a result, the operating voltage is reduced. The strong anchoring force that the polymer binders exert to the LC directors is responsible for the observed fast response time.

If we operate the gel in reflective mode, the phase will be doubled. Although the achievable phase change is small ($\delta \sim 0.08\pi$), it is still quite useful for the polarization-independent microlens and microprism applications. From Eq. (30), to increase phase shift we could either enlarge the LC cell gap or use a higher birefringence LC material.⁶⁷ The latter is preferred because increasing cell gap would lead to a higher operating voltage. However for a given domain size, increasing LC birefringence would also enhance light scattering capability. Therefore, an optimal LC birefringence should exist before light scattering takes place. On the other hand, to lower the on-state voltage we could use a higher $\Delta\epsilon$ LC mixture.

4.4.6 Conclusion

In conclusion, we have demonstrated a homeotropic LC gel whose phase modulation is polarization insensitive. Such a phase modulation is free from light scattering and hysteresis. Its response time is submillisecond at room temperature and its

operation stability is excellent. The obtainable phase change is 2X larger than that of a nano-PDLC system, but at a lower operating voltage.

4.5 Polarization Independent LC Phase Modulators Using a Thin Polymer-Separated Doubled-layered Structure

So far, we have demonstrated three polarization independent LC phase modulators by using voltage-biased PDLC¹⁸, voltage-biased PSCT¹⁹, and voltage-biased homeotropic LC gels²⁰ in previous sections. A common problem of these approaches is that their phase change is relatively small and the operating voltage quite high. Thus, more polarization-independent light modulation mechanisms need to be developed.

In this part, we demonstrate a polarization-independent LC phase modulator using a double-layered structure with two ultra-thin anisotropic polymer films as cell separators²¹. The double-layered structure has been proposed for guest-host liquid crystal displays (LCDs) more than two decades ago.^{5-8,68} The conventional approach uses a thin glass (~0.3 mm) or Mylar film (~0.1 mm) to separate the two orthogonal LC layers. In the former case, an indium-tin-oxide (ITO) glass substrate is used as a middle substrate. To overcome the electric field shielding effect, both sides of the ITO layers should be pixilated and connected (e.g., via feed-through holes), and then overcoated with a thin polyimide layer which is rubbed in the orthogonal directions to match the LC alignment. This approach is difficult for high resolution devices because of the complicated pixel structures and extra alignment between the passive ITO pixels in the middle substrate and active elements. To reduce the parallax incurred by the middle glass substrate and to enable high resolution, a thin Mylar film can be considered. However, the Mylar film cannot align the LC molecules⁸ because the baking temperature of polyimide is higher than the glassy transition temperature of the Mylar film. The anisotropic polymer films

we developed in this paper are thin and they possess alignment capability. As a result, excellent LC alignment, large phase shift, and low operating voltage are achieved. Using two 12- μm orthogonal E7 LC layers, we obtain 2π phase shift ($\lambda=633\text{ nm}$) at merely 9 V_{rms} and 8.1π phase shift at 40 V_{rms} . This is by far the polarization-independent LC phase modulator ever demonstrated exhibiting the largest phase change at the lowest operating voltage.

4.5.1 Structure

Figure 63 shows the schematic design of our polarization-independent phase modulator. The cell consists of two glass substrates which are overcoated with thin ($\sim 80\text{ nm}$), mechanically buffed polyimide layers, two anisotropic polymer films, and two LC layers. The top and bottom LC directors are oriented orthogonal to each other. The anisotropic polymer films were peeled off from a UV-induced phase separation of a LC/polymer cell. Such a polymer film is an optically uniaxial film. It has excellent alignment capability⁶⁹. To achieve orthogonal homogeneous LC layers, the principal axes of these two anisotropic polymer films were also arranged to be orthogonal to each other.

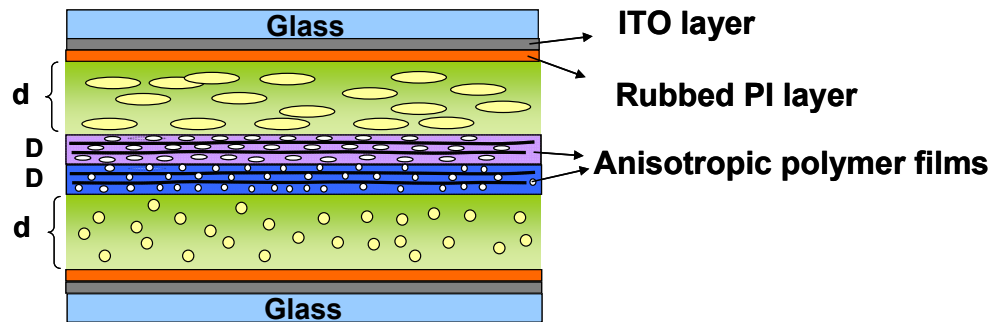


Figure 63: The structure of a polarization-independent phase modulator using a thin polymer-separated double-layered structure

4.5.2 Sample Preparation

To fabricate the anisotropic film, we mixed a Merck E7 nematic LC mixture, photo-initiator IRG184, and an LC monomer RM-257 (4-(3-Acryloyloxypropyloxy)-benzoic acid 2-methyl-1,4-phenylene ester) at 19:1:80 wt % ratios. The LC/monomer mixture was injected into a homogeneous cell with 23 μm cell gap which was controlled by the Mylar stripes and then the cell was exposed to a UV light with intensity $I = 10 \text{ mW/cm}^2$ for ~ 30 min at 90 $^\circ\text{C}$. After UV exposure, the two substrates of the homogeneous cell were peeled off and a solidified anisotropic film with 23 μm thickness was obtained. We prepared two polymer films with the same thickness ($D=23 \mu\text{m}$) and stacked them together in orthogonal directions, as Figure 63 depicts. The LC mixture employed is also E7. The LC was filled to the empty cell by the one-drop-fill method. The cell gap of each LC layer was controlled by a Mylar film to be $d\sim 12 \mu\text{m}$. The total dimension of our cell is around 25 mm by 25 mm.

4.5.3 Surface Morphologies of an Anisotropic Polymer Film

Figure 64 shows the surface morphologies of an anisotropic polymer film taken from an atomic force microscope (AFM) (Dimension 3100, Digital Instruments). Silicon nitride cantilever with a normal spring constant of 30 N/m and an apical radius of 20 nm

was used. The AFM measurements were performed in tapping mode at a scan rate of 1 Hz in air under ambient conditions. In Figure 64, the polymer film appears to consist of elongated polymer grains. The elongated polymer grains are oriented at the same direction (marked with an arrow), giving an anisotropic polymer surface. The root-mean-square (RMS) roughness of the surface can be defined as RMS average of height deviations taken from the mean data plane. Then, the RMS roughness of the surface of the anisotropic polymer film is 1.01 nm. The LC molecules were found to be aligned along the elongate direction of the polymer grains in order to minimize free energy. During fabrication process, when we peel off the polymer film from the ITO glass substrates the LC molecules near the surface stay on the glass substrates which leave the anisotropic polymer film with valleys and polymer network structures. The size and the structure of the polymer grains depend on the fabrication conditions. In chapter 5, we will discuss the anisotropic polymer film in more details.

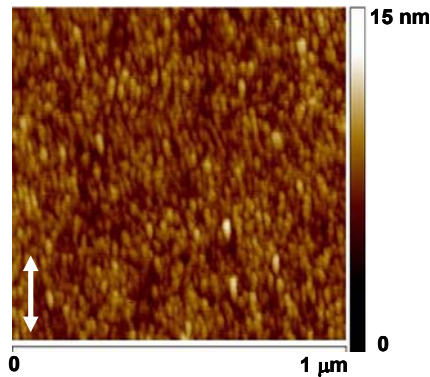


Figure 64: AFM images of the anisotropic polymer film surface. LC directors are aligned along the arrow. The color bars indicate the height.

4.5.4 Experimental Setup

To characterize the phase shift of the double-layered LC cell, we used Mach-Zehnder interferometer as depicted in Figure 65. An unpolarized He-Ne laser ($\lambda=633$ nm) was used as a light source. The laser beam was split equally into two arms by a beam splitter. We placed the LC cell in one arm. The cell was driven by a square-wave voltage at frequency $f=1$ kHz. The interference pattern was recorded by a digital video camera (SONY, DCR-HC40). The whole system was built on a floating optical table to avoid any environment-induced fluctuation.

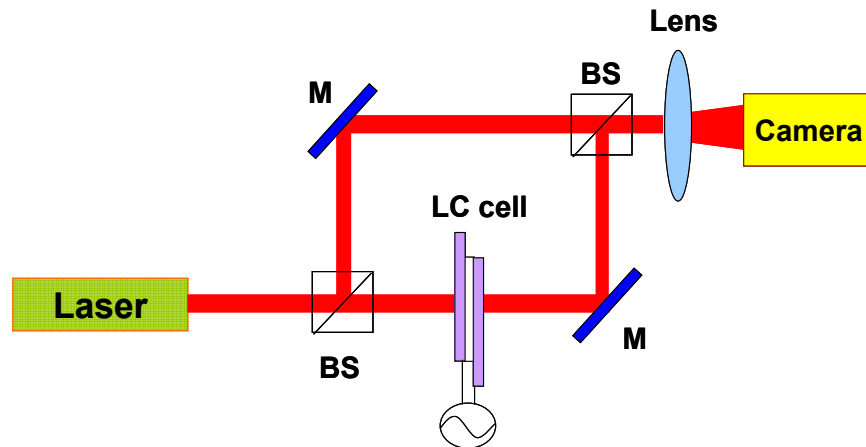


Figure 65: Mach-Zehnder interferometer for measuring the phase shift. M: dielectric mirror, and BS: beam splitter.

4.5.5 Phase Change

Figure 66(a) is a recorded movie showing the voltage-dependent interference fringes of the double-layered LC cell. The phase shift at $V=0$ was used as reference. Figure 66(b) plots the interference fringes at three specific voltages: $V=0$, 7, and 9 V_{rms} .

The phase shift is around 1.06π between 0 and $7 V_{\text{rms}}$ and around 2π between 0 and $9 V_{\text{rms}}$.

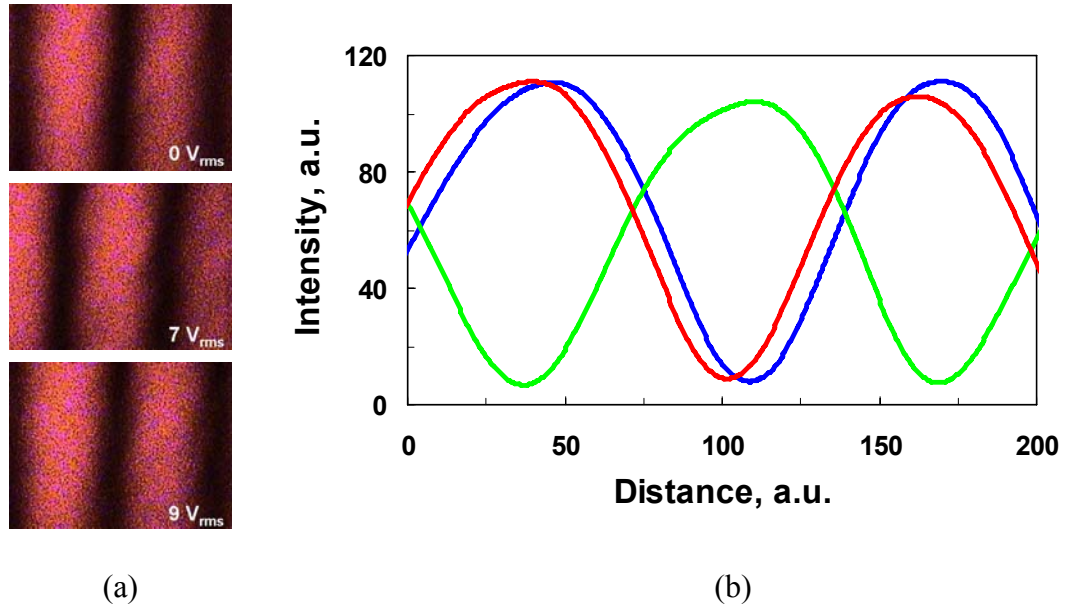


Figure 66: (a) Interference patterns at various voltages and (b) intensity profiles at 0 (blue), 7 (green) and $9 V_{\text{rms}}$ (red). The two orthogonal LC cells are $12\text{-}\mu\text{m}$ E7 layers. $\lambda=633 \text{ nm}$ from an unpolarized He-Ne laser.

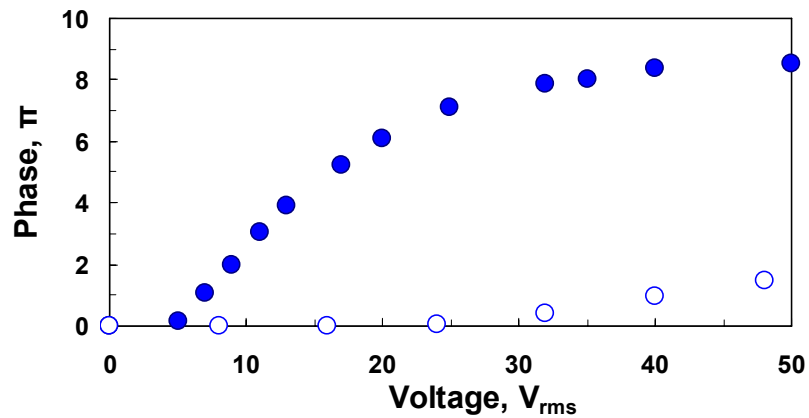


Figure 67: Voltage-dependent phase shift of the polarization-independent LC phase modulator at $\lambda=633 \text{ nm}$. Filled circles represent the measured data using our anisotropic polymeric films while open circles are the simulated results of the double-layered structure using a 0.3-mm -thick glass separator.

Figure 67 plots the measured voltage-dependent phase shift at $\lambda=633$ nm of the double-layered E7 LC cell (filled circles). The threshold voltage is $\sim 5 V_{\text{rms}}$. For reference, the threshold voltage of the single E7 cell without any middle substrate is $\sim 0.95 V_{\text{rms}}$. The increased threshold voltage is due to the dielectric shielding effect of the middle polymeric layers. In the interferometer, the measured phase shift is referenced to that at $V=0$. The total phase shift reaches $\sim 8.1\pi$ at $V=40 V_{\text{rms}}$. This total phase shift remains the same no matter we placed a polarizer in front of the LC device or rotated the polarizer.

We also performed numerical analysis for the double-layered structure using a 0.3-mm-thick glass separator. Both sides of the glass separator are assumed to be coated with thin polyimide layers and rubbed in orthogonal directions to match with the top and bottom substrates. The simulation results (open circles) are included in Figure 67 for comparison. The same LC material (E7) and same cell gaps are assumed. The calculated threshold voltage is as high as $\sim 24 V_{\text{rms}}$ because of the electric field shielding effect from the relatively thick glass separator. To obtain 8π phase shift, the required voltage is $\sim 600V_{\text{rms}}$. Our thin polymeric separators reduce the required operating voltage by nearly 15X.

4.5.6 Discussion

Theoretically, the phase difference between two arms of the Mach-Zehnder interferometer is:

$$\phi(V) = \kappa \cdot (n_{eff}(\theta, \psi) + n_{eff}(\theta, \frac{\pi}{2} + \psi) - 2) \cdot d + \delta, \quad (31)$$

where $\kappa = 2\pi / \lambda$, λ is the laser wavelength, d is the cell gap, and δ is the phase difference contributed by the two anisotropic polymer films, glass substrates, and optical path difference in the air. At $V=0$, the phase difference between the two arms is

$$\phi(0) = \kappa \cdot (n_e + n_o - 2) \cdot d + \delta, \quad (32)$$

At a very high voltage, all the LC directors are reoriented along the electric field direction except the boundary layers. Under such a circumstance, the effective refractive index becomes

$$n_{eff}(\theta, \psi) = n_{eff}(\theta, \frac{\pi}{2} + \psi) = n_o, \quad (33)$$

And the phase difference between two interferometer arms is as follows:

$$\phi(V \gg 0) = \kappa \cdot (2n_o - 2) \cdot d + \delta, \quad (34)$$

Therefore, the total phase shift is reduced to the well-known expression:

$$\Delta\phi = \phi(0) - \phi(V \gg 0) = (2\pi / \lambda) \cdot d \cdot (n_e - n_o), \quad (35)$$

The birefringence of E7 is $\Delta n = n_e - n_o \approx 0.21$ at $\lambda=633$ nm. The calculated total phase shift is $\sim 8\pi$, which is rather close to our measured value (8.1π) at $V=40$ V_{rms}.

The obtainable phase shift of our double-layered structure is much larger and the operating voltage is much lower than those of nano-PDLC, PDLC, and PSCT. To further lower the operating voltage of our double-layered structure, we can reduce the thickness of the anisotropic polymer films, but the tradeoff is that a thinner polymer film may degrade the uniformity of the cell.

The response time of our double-layered LC cell was measured to be ~ 300 ms at $T \sim 23^\circ\text{C}$. The slow response time originates from the thick LC layers ($d \sim 12 \mu\text{m}$) and high viscosity of the E7 LC employed. To reduce response time, a high Δn and low viscosity LC could be used⁵⁴. A high Δn LC enables a thinner cell gap to be used which is helpful for reducing response time.

4.5.7 Conclusion

In conclusion, we have demonstrated a polarization-independent LC phase modulator using a double-layered structure. The LC directors are orthogonal to each other. Two anisotropic polymer films are used as the cell separators and alignment layers. The total phase shift is $\sim 2\pi$ at $V=9 V_{\text{rms}}$ and $\sim 8.1\pi$ at $V=40 V_{\text{rms}}$ at $\lambda=633$ nm. Using a thinner cell gaps would simultaneously reduce the response time and operating voltage. The key technical challenge is to control the cell gap and uniformity of each LC layer, especially for a large aperture phase modulator. The uniformity of polymer film is relatively easy to obtain and the cell gap can be controlled by using post spacers. Finally, this approach opens a new door for achieving polarization-independent phase modulation.

4.6 Polarization Independent LC Phase Modulators Using Double-layered LC gels

In section 4.5, we have demonstrated polarization independent LC phase modulators using a thin polymer-separated double-layered structure. The phase is large, but the response time is slow. In order to shorten the response time based on the similar structure, we demonstrate a phase modulator using two thin stratified LC gels²² in this section. The two homogeneously aligned gel films are identical, but stacked in orthogonal directions. Because of high LC concentration and uniform molecular alignment, our LC gel possesses a large phase change ($>1\pi$). Meanwhile, because of the relatively high monomer concentration (28 wt%) the formed LC domains are in the submicron range. Therefore, the response time of the LC gel is around 0.5 ms.

4.6.1 Structure and Fabrication Process

In a LC gel, the homogeneously-aligned LC is stabilized by dense polymer networks, as shown in Figure 68(a). To obtain a double-layered structure, we cut the LC gel into half and stacked the films together at orthogonal direction and then covered with another top ITO substrate, as shown in Figure 68(b).

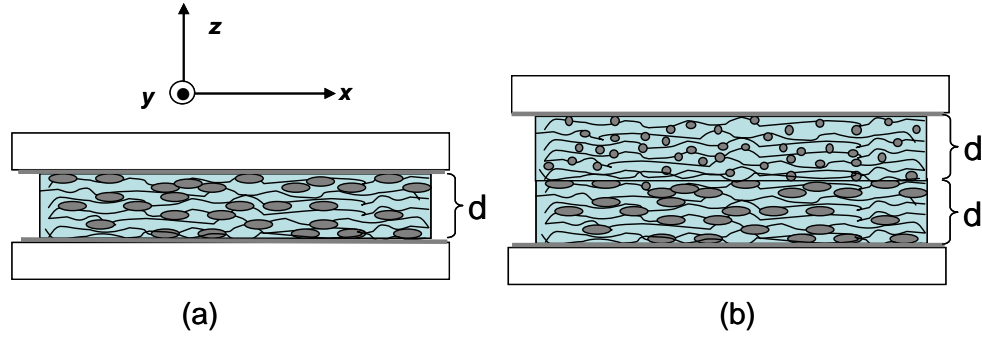


Figure 68: A homogeneous LC gel: (a) single layer and (b) double layers.

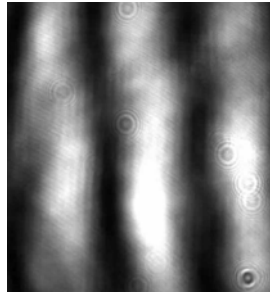
To prepare a LC gel, we mixed 28 wt% of photocurable rod-like LC diacrylate monomer (RM257) in a nematic LC (E48: $n_o=1.523$, $\Delta n=0.231$ at $\lambda=589$ nm). The mixture was injected into an empty cell in the nematic state. The inner surfaces of the indium-tin-oxide (ITO) glass substrates were coated with a thin polyimide layer and then rubbed in antiparallel directions. The filled cell was exposed to an ultraviolet light (UV) ($\lambda=365$ nm, $I\sim 10$ mW/cm²) for 30 min. The cell gap was controlled at 8 μm by spacer balls.

After UV exposure, the cell is highly transparent. To get a gel layer, we cleaved off the top glass substrate. The stratified gel remained on the bottom substrate surface without LC leakage. We first examined the LC alignment of the gel layer using a polarized optical microscope. The gel (on the bottom substrate) was placed between crossed polarizers. If the cell rubbing direction was along one of the polarizer's axis, a dark state was obtained. Rotating the gel film by 45°, the brightest state was obtained. These results imply that the LC gel is indeed aligned homogeneous without being damage during cell cleaving.

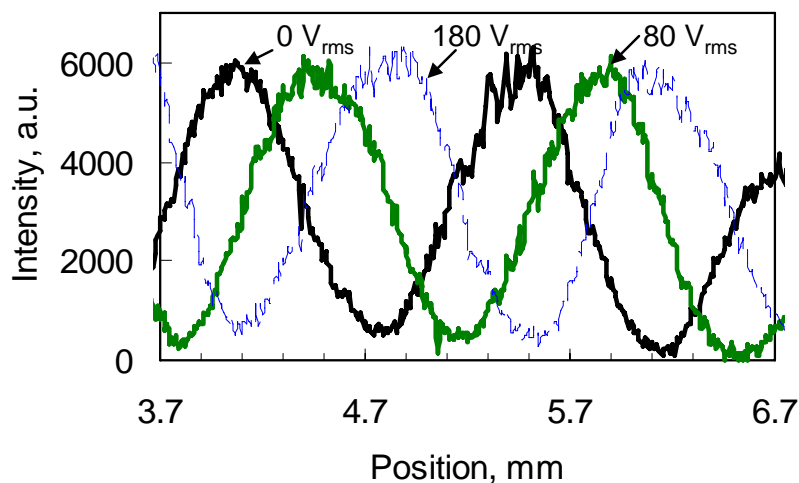
4.6.2 Phase Change

We used the Mach-Zehnder interferometer to measure the phase shift of the orthogonal gel cell. An unpolarized He-Ne laser ($\lambda=633$ nm) beam was split equally into two arms by a beam splitter. The two beams were then recombined again. In the beam overlapping region, several parallel interference fringes occur. The stacked gel was placed in one arm. When an ac voltage ($f=1$ kHz) was applied to the LC gel, the interference fringes moved as recorded by a digital CCD camera (SBIG Model ST-2000XM).

Figure 69(a) shows the recorded interference fringes at $V=0$. As the voltage increases, the fringes shift. Figure 69(b) shows the intensity profiles of the fringes at $V=0$ (black), $80 V_{\text{rms}}$ (green), and $180 V_{\text{rms}}$ (blue), respectively. More than 1π phase shift is observed between 0 and $180 V_{\text{rms}}$.



(a)



(b)

Figure 69: (a) Interference fringes of the LC gel and (b) intensity profile at different voltages.

The voltage-dependent phase shift of the 16- μm double-layered LC gel at $\lambda=633$ nm was plotted in Figure 70. The threshold voltage is ~ 30 V_{rms} . This high threshold originates from the dense polymer networks. Beyond this threshold, the phase change increases almost linearly with the applied voltage. The estimated total phase change from an 8- μm LC gel which contains ~ 80 wt% E48 should be $\sim 2\pi$ for a linearly polarized He-Ne laser ($\lambda=633$ nm). Therefore, our applied voltage has not reached the saturation regime. In comparison to a nano-PDLC, our LC gel possesses a much larger phase shift at a lower operating voltage because of the higher LC concentration and directional stratification.

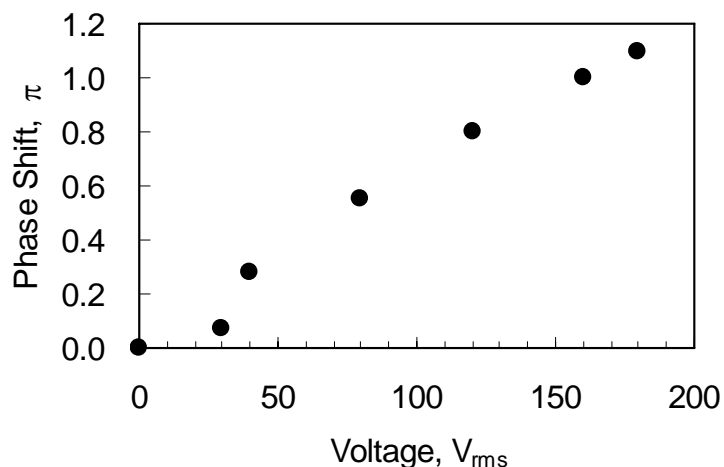
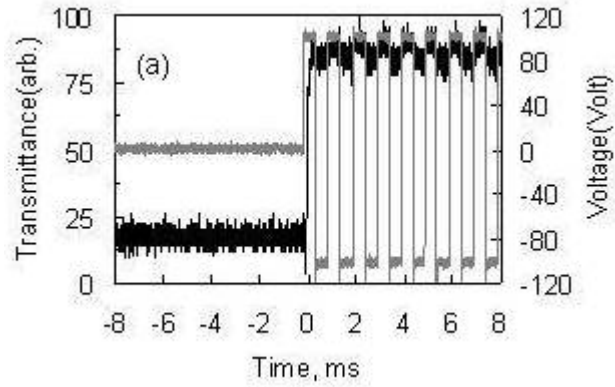


Figure 70: Measured phase shift of a 16- μm double-layered LC gel at different voltages.

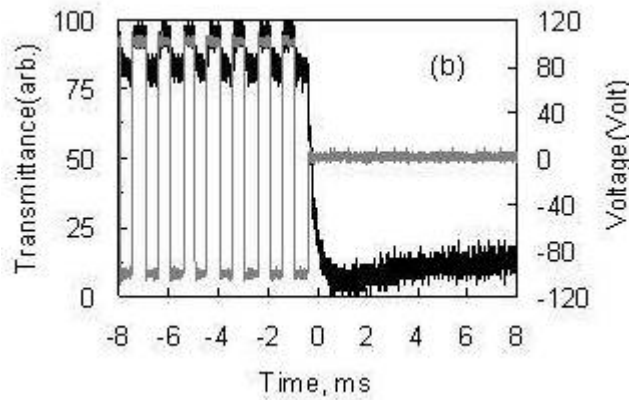
4.6.3 Response Time

Response time is another important parameter for a LC-based phase modulator. To measure the response time of the LC gel, we used a photodiode detector instead of CCD camera to receive the transmitted beam. A diaphragm was put right before the detector. At $V=0$, no light passes through the diaphragm. A square voltage $V=100 V_{\text{rms}}$ at 1 kHz was applied to the LC gel cell. Results are shown in Figure 71. The measured rise time is ~ 0.2 ms and decay time is ~ 0.5 ms at room temperature ($\sim 22^\circ\text{C}$). Such a fast response time results from the small LC domain sizes and polymer stabilization. Due to the relatively high monomer concentration (28 wt%), the formed polymer networks are quite dense so that the formed LC domains are in submicron size. Similar to a nano-PDLC, the contact interfaces between the polymer networks and the LC molecules are

large. As a result, the anchoring force of polymer networks exerting on the LC is very strong. This is the primary reason for the observed fast response time and high threshold voltage.



(a)



(b)

Figure 71: The measured response time of the 16- μm LC gel between 0 and 100 V_{rms} bursts ($f=1$ kHz). (a) Rise time ~ 0.2 ms and (b) decay time ~ 0.5 ms at $T \sim 22$ $^{\circ}\text{C}$. The gray lines in each figure represent the applied voltage and the black lines represent the optical signals.

4.6.4 Discussion

In Figure 68(a). The phase shift along x -axis can be expressed as

$$\Delta\delta_{Gel}(V) = \frac{2\pi dc[n_e - n_{eff}(V)]}{\lambda}, \quad (36)$$

where d is the cell gap, c is the LC concentration, λ is the incident wavelength, n_e and $n_{eff}(V)$ are the extraordinary and effective refractive index of the LC, respectively. At $V \rightarrow \infty$, $n_{eff} \rightarrow n_o$, where n_o is the ordinary refractive index of LC. From Figure 68(a), the homogeneous LC gel is polarization dependent. To make it polarization independent, we stack two identical homogeneous LC gels in the orthogonal directions, as shown in Figure 68(b).

It has been shown that two orthogonally oriented homogeneous LC layers are polarization independent for phase modulation if the two films are identical.²¹ As the voltage increases, the phase change occurs because of the electric field-induced LC director reorientation. At a very high voltage, the voltage-induced phase shift is reduced to:

$$\Delta\delta_{Gel}(V \rightarrow \infty) = \frac{2\pi dc\Delta n}{\lambda}, \quad (37)$$

where $\Delta n = n_e - n_o$ is the LC birefringence. In comparison, the LC droplets in a nano- or voltage-biased PDLC cell are almost randomly orientated. Thus, the phase shift is

$$\Delta\delta_{PDLC}(V) = \frac{2\pi d'c'[\bar{n} - n_{eff}(V)]}{\lambda}, \quad (38)$$

where $\bar{n} = (2n_o + n_e)/3$ is the average refractive index of the LC at $V=0$, d' and c' are the cell gap and LC concentration, respectively. At $V \rightarrow \infty$, $n_{eff} \rightarrow n_o$ and the phase shift is reduced to

$$\Delta\delta_{PDLC}(V \rightarrow \infty) = \frac{2\pi d' c' \Delta n}{3\lambda}, \quad (39)$$

To fairly compare the phase change of the orthogonal LC gel films with the nano-PDLC, let us use the same LC material. To achieve polarization independence, the LC gel needs two orthogonal layers, but nano-PDLC only needs one. Thus, $d'=2d$. However, the LC concentration in the gel is 2X higher than that in nano-PDLC, i.e., $c=2c'$. From Eq. (37) and Eq. (39), we find

$$\frac{\Delta\delta_{Gel}(V \rightarrow \infty)}{\Delta\delta_{PDLC}(V \rightarrow \infty)} = 3, \quad (40)$$

From Eq. (40), the phase shift of the LC gel is 3X higher than that of a nano-PDLC.

To get a 2π phase change for laser beam steering and other photonic applications, we could operate the LC gel in reflective mode without increasing the operating voltage. For practical applications, the operating voltage of our LC gel is still very high (11 $V_{rms}/\mu m$). To increase phase change, we could use a high Δn LC material while to reduce the operating voltage, we could use a high dielectric anisotropy ($\Delta\epsilon$) LC or optimize the LC and monomer concentration. A high Δn LC also enables a thinner gel to be used which, in turn, helps reduce the operating voltage. A high $\Delta\epsilon$ LC lowers the threshold and the operating voltages simultaneously. Increasing the LC concentration would boost the phase change and reduce the operating voltage; however, the gel may become too soft to stand alone. Moreover, its response time will increase.

4.6.5 Conclusion

In conclusion, we have developed a double-layered LC gel for polarization independent phase-only modulators. Its phase change at $\lambda=633$ nm reaches more than 1π at $V \sim 11$ $V_{\text{rms}}/\mu\text{m}$ and its response time is in the submillisecond range. Potential applications of this polarization independent LC gel for laser beam steering, microlens array, agile filter, and switchable 2D/3D liquid crystal displays are emphasized.

CHAPTER 5: ANISOTROPIC POLYMER FILM

In this chapter, we demonstrate a versatile anisotropic polymer film which can be used as an alignment layer, an alternative substrate and a compensation film. In section 5.2, the fabrication process and surface morphologies of the anisotropic polymer film are introduced. In section 5.3, we show a wide-view in-plane-switching LCD using an anisotropic film to replace a glass substrate.

5.1 Anisotropic Polymer Film

5.1.1 Film Fabrication

The materials we used for fabricating the aligned-polymer film are a Merck E7 nematic LC mixture, photo-initiator IRG184, and an LC monomer RM-257 (4-(3-Acryloyloxy-propyloxy)-benzoic acid 2-methyl-1,4-phenylene ester) mixture. The concentration of IRG184 is 1 wt%. The chemical structures of E7 and RM 257 is shown in Figure 72. Figure 73 plots the phase diagram of the LC/monomer mixture at various concentrations before UV curing. The LC/ monomer mixture was injected into a homogeneous cell with 23 μm gap and then the cell was exposed to a UV light with intensity $I = 10 \text{ mW/cm}^2$ for ~ 30 min at a constant temperature. After UV exposure, the two substrates of the homogeneous cell were peeled off and a stratified anisotropic film

with 12 μm thickness was obtained. The fabrication process is also illustrated in Figure 74. Based on our experiment, at a fixed curing temperature the anisotropic polymer film is more flexible if the monomer concentration is lower. When the monomer concentration is between 70 and 100 wt%, the anisotropic polymer film can align LC molecules as long as the UV curing temperature is within the nematic phase. In the isotropic phase, the film's alignment capability is rather weak. Curing temperature also influences film's flexibility.

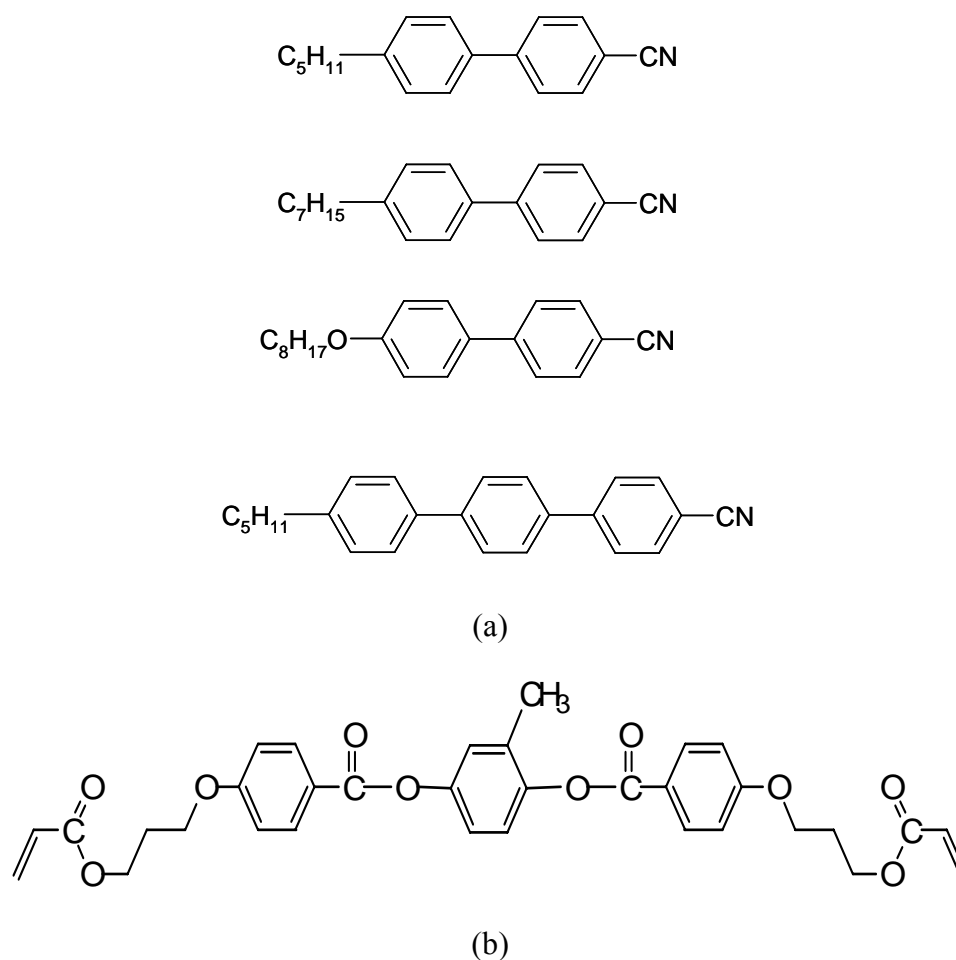


Figure 72: (a) The compositions of liquid crystal E7. (b) The chemical structure of monomer RM257.

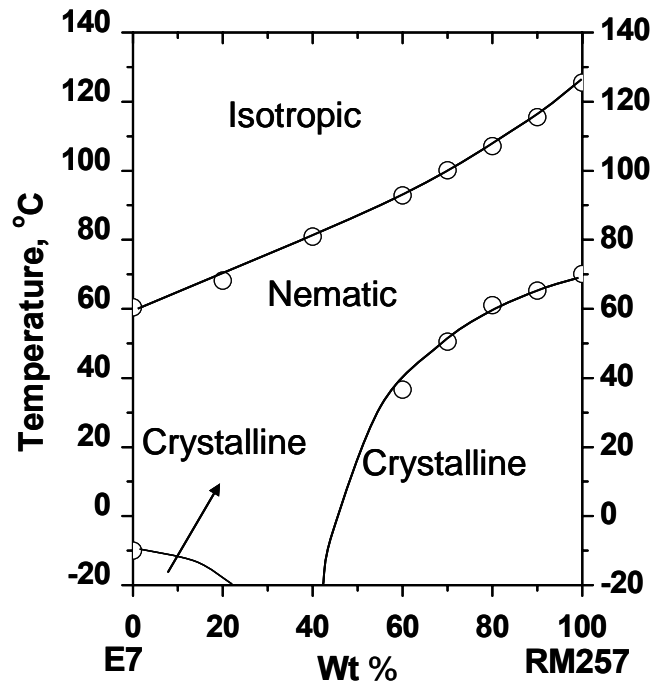


Figure 73: Phase diagram of the E7/RM257 mixtures. All the mixtures have 1wt% IRG184 photo-initiator

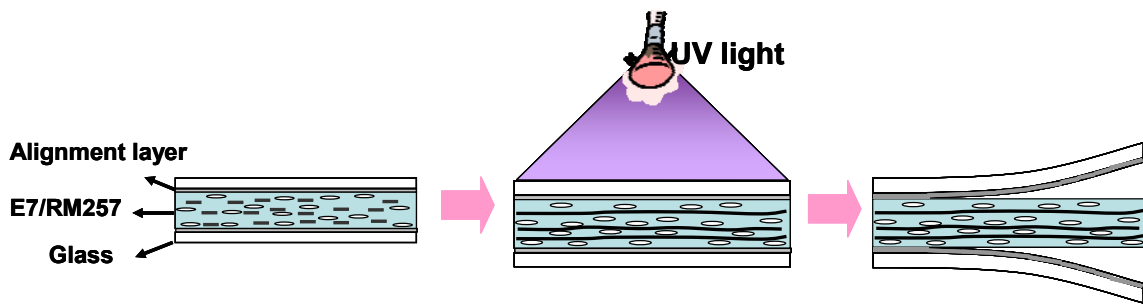


Figure 74: Fabrication process of the anisotropic polymer film.

5.1.2 Surface Morphologies

To further observe the surface morphologies of the anisotropic polymer film, an atomic force microscope (AFM) (Dimension 3100, Digital Instruments) was used to image the rubbed polyimide surface and anisotropic polymer film surface as shown in Figure 75. Silicon nitride cantilever with a normal spring constant of 30 N/m and an apical radius of 20 nm was used. The AFM measurements were performed in tapping mode at a scan rate of 1 Hz in air under ambient conditions. In Figure 75(a) and Figure 75(b), the anisotropic polymer film is rougher than the rubbed PI film whose thickness is ~100 nm. In Figure 75(b), the surface of the anisotropic polymer film shows elongated aggregation of polymer grains along the arrow direction. The root-mean-square (RMS) roughness of the surface can be defined as RMS average of height deviations taken from the mean data plane. Then, the RMS roughness of the surface of the anisotropic polymer film is 1.52 nm. The LC molecules tend to align along the direction of the elongated polymer grains in order to minimize free energy.

The physical mechanism of how the anisotropic film aligns the LC molecules is not yet completely understood. A speculated mechanism is due to the nano-structure of the elongated polymer grain. Before photo-polymerization, the LC molecules and LC monomers are aligned by the rubbed PI layers. After phase separation, the polymer grain of the polymeric film aggregates and elongates along the rubbing direction. During fabrication process, when we peel off the polymer film from the ITO glass substrates the LC molecules near the surface stay on the glass substrates which leave the anisotropic polymer film with valleys and polymer network structures. When the polymeric film is used as a top substrate, the injected LC tends to fill the valleys and follow the elongated

polymer grain direction. The film seems to have memory effect before it is peeled off from the PI cell. The size and the structure of the polymer grains depend on the fabrication conditions. These factors will undoubtedly affect the anchoring strength and the molecular alignment.

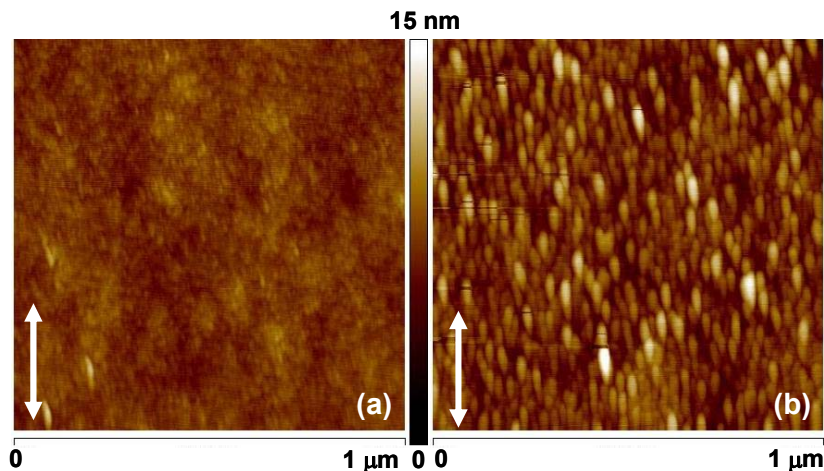


Figure 75: The AFM images of (a) the rubbed PI film surface and (b) the anisotropic polymer film surface. The LC directors are aligned along the arrow. The color bars indicate the height.

The AFM images at various monomer concentrations are shown in Figure 76. The curing temperature was 90°C. As the monomer concentration decreases, the elongated aggregation of polymer grains turns out less obvious. Based on our experiments, the alignment capability is weaker as monomer concentration decreases. In Figure 77, the RMS roughness is similar when the monomer concentration is larger than 70 wt%. The RMS roughness increases when the monomer concentration is below 70 wt%.

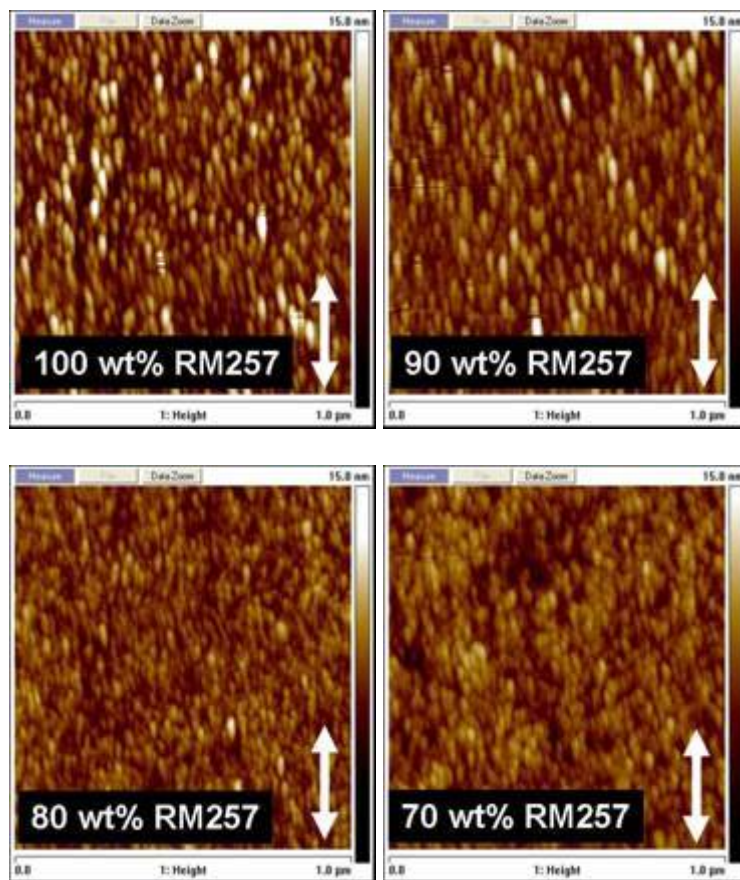


Figure 76: The AFM images of the anisotropic polymer film surface at different monomer concentrations. The curing temperature is 90°C. The LC directors are aligned along the arrow. The color bars indicate the height.

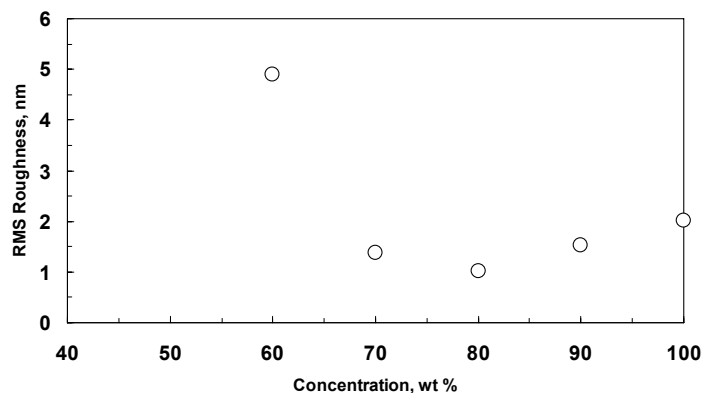
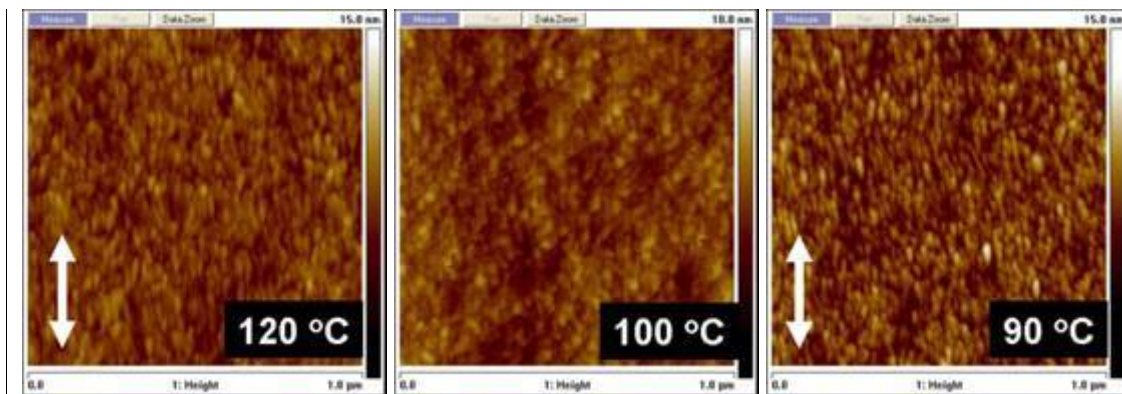


Figure 77: The RMS roughness of the surfaces of anisotropic polymer films as a function of monomer concentration. The curing temperature is 90°C.

The AFM images of the anisotropic polymer films at different curing temperature are shown in Figure 78. The monomer concentration was fixed at 80 wt%. All the polymer grains are elongated along one direction except the one at 100 °C, which is also the phase transition temperature for the 80 wt% monomer. Based on our experimental results, the alignment capability is stronger when the curing temperatures is in the nematic phase region, and is weaker when the curing temperature is larger than the phase transition temperature. Moreover, the film's birefringence disappears when the curing temperature is larger than the clearing temperature of the mixtures. When cured in the nematic phase, our polymer films are birefringent. The anisotropic polymer film we fabricated has birefringence $\Delta n \sim 0.1$ at $\lambda = 633$ nm.



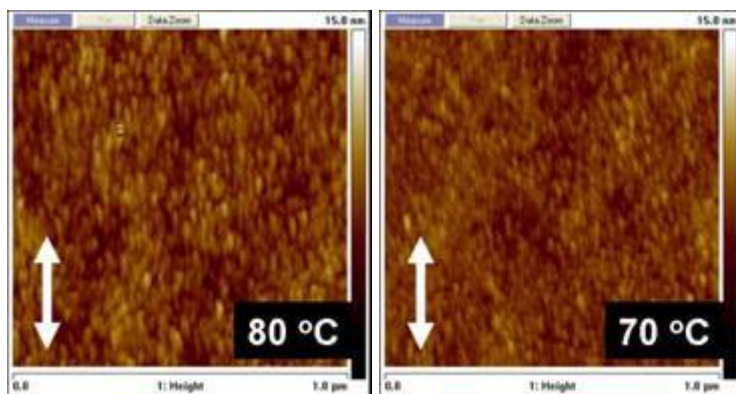


Figure 78: The AFM images of the anisotropic polymer film surface at different curing temperatures. The monomer concentration is 80 wt%. The LC directors are aligned along the arrows. The color bars indicate the height.

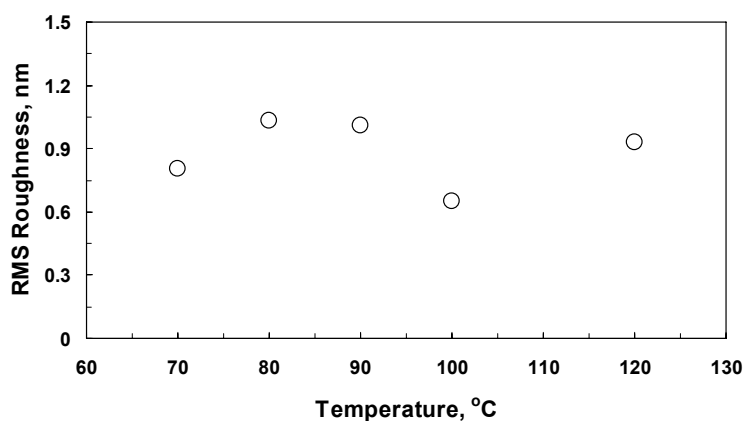


Figure 79: The RMS roughness of the surfaces of anisotropic polymer films as a function of curing temperature. The monomer concentration is 80 wt%.

5.2 Applications: IPS-LCD Using a Glass Substrate and an Anisotropic Polymer Film

Most liquid crystal display (LCD) devices use two glass substrates in order to confine the fluidic liquid crystal (LC). To align the LC molecules, the inner surfaces of

the substrates are usually coated with a thin polyimide (PI) layer. These PI layers are mechanically buffed to produce uniform pretilt angle. To reduce weight, the single glass or plastic substrate approach has been explored recently in which the LC device consists of a glass substrate and a thin polymer film. Although the polymer film does not have electrode, it can still be used in the in-plane-switching (IPS) mode where the striped electrodes are located on the bottom glass substrate.

IPS LCD is an important technology for achieving wide-viewing angle. Figure 80 depicts the device structure and operation mechanism of an IPS LCD. The typical IPS LCD consists of two glass substrate with rubbed polyimide. One of the substrates has electrode stripes in order to provide in-plane electric fields. In the voltage-off state, the LC directors are parallel to the striped electrodes. As the voltage exceeds a threshold, the LC directors are rotated by the in-plane electric field. In order to reduce the weight of an IPS LCD which has two glass substrates, several display manufacturers are using thinner glass substrates. However, to prevent the breaking of the thin glass substrates the cost and assembly processes are relatively complicated. By replacing a glass substrate with a polymer film, a single glass substrate IPS LCD is a promising approach for reducing the weight of LCDs.

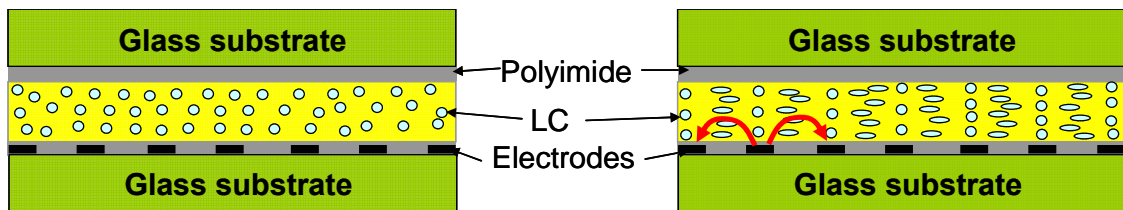


Figure 80: The device structure and operation mechanism of an IPS LCD. (a) Voltage-off, and (b) Voltage-on.

Several of such single-substrate IPS-LCDs have been demonstrated. Penterman et al ⁷⁰⁻⁷² proposed the photo- enforced stratification (PES) method where the polymer walls and a cover substrate are formed after photo-induced phase separation processes. Kim et al ⁷³ proposed single substrate devices by using phase separated composite film (PSCOF) as a cover substrate. But in both methods the top polymer film does not have capability to align the LC molecules and the polymer walls can cause light scattering. The polymeric film without alignment capability would reduce the device contrast ratio and lengthen the response time because of its weak anchoring strength. To overcome these drawbacks, some research groups proposed thin aligned-polymer film method. Sato et al ⁷⁴ developed a fluorinated polymer film for aligning LC on plastic substrates, however, it still requires rubbing process. Murashige et al ⁷⁵ demonstrated a molecule-aligned LC polymer film. The film was coated on the surface of a rubbed polyimide substrate. A partial photopolymerization process was required in order to achieve uniform alignment within the film. The anchoring strength of the film is about one order of magnitude weaker than that of the buffed polyimide. How to align the LC molecules near the top polymer film of the single-substrate LCD remains an urgent technical challenge.

To prove that our anisotropic polymer film can indeed align LC molecules, in this section, we demonstrate an IPS-LCD using a glass substrate and an anisotropic polymer film. The performances, such as contrast ratio, driving voltage, and response time, are comparable to the two-glass- substrate IPS LCDs. The function of this polymer film is versatile. It not only serves as a top substrate but also aligns the LC molecules without any rubbing treatment. Furthermore, by controlling the fabrication process the polymeric film can also function as a phase compensation film. This technology can be extended for

making high-contrast double-layered guest-host displays and flexible displays using IPS LCDs.

5.2.1 Structure and sample preparation

The fabrication process of the anisotropic polymer film has been mentioned in the previous section. The aligned-polymer film we used here consists of E7, IRG184, and RM257 at 9:1:90 wt % ratios and the UV curing temperature is 90 °C. The LC/monomer mixture has a nematic phase between 65.3 °C and 115.5 °C before UV curing. The detailed cell structure is depicted in Figure 81. Our LC cell consists of a top anisotropic polymer film and a bottom IPS glass substrate. An IPS glass substrate which was overcoated with a thin polyimide layer and then mechanically buffed was used as the bottom substrate. The electrode width is $W=4\ \mu\text{m}$ and the electrode gap is $G\sim 10\ \mu\text{m}$. The rubbing direction of the glass substrate is 10° with respect to the electrode stripes. The cell gap between the anisotropic polymeric film and the IPS substrate is $d=12\ \mu\text{m}$. The orientation of the LC directors within the anisotropic film was anti-parallel to the rubbing direction of the IPS substrate. The LC mixture employed for the IPS cell is also E7. The uniformity of the cell gap is not an issue because the film is laminated on a sheet polarizer. We used one-drop filling method to fill the LC cell. The sample size of the IPS cell is around 25 mm by 25 mm.

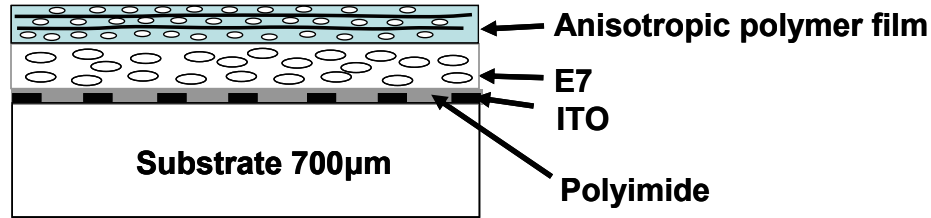


Figure 81: The device structure of an IPS LC cell consisting of a top anisotropic polymeric film and a bottom ITO-glass substrate. The thickness of the top anisotropic film is $12\ \mu\text{m}$, and the cell gap is also $12\ \mu\text{m}$.

5.2.2 Images under Optical Microscope

Figure 82(a) show the microscope photos of the single-substrate IPS cell covered by the top anisotropic polymer film under crossed-polarizers at $V=0$, 6, and $10\ V_{\text{rms}}$. A white light was used for taking the microscope photos. The optical axis of the bottom polarizer was oriented parallel to the LC rubbing direction. At $V=0$, a very good dark state is achieved indicating that the LC molecules are well aligned. The threshold voltage of the cell is $V_{\text{th}} \sim 2\ V_{\text{rms}}$ which corresponds to $E=0.2\ \text{V}/\mu\text{m}$ (note that $G=10\ \mu\text{m}$). As the voltage exceeds V_{th} , the transmittance increases gradually because the LC molecules begin to follow the external electric field. For comparison, a conventional IPS cell was also prepared, i.e., the bottom glass substrate has interdigitated ITO electrodes and the top substrate is a plane glass with rubbed polyimide. The rubbing direction of the top substrate is anti-parallel to the bottom IPS substrate. Figure 82(b) shows the microscopic textures of the conventional IPS cell. Compared with Figure 82(a) and Figure 82(b), our single-substrate IPS cell has very similar dark and bright states to the conventional IPS

cell. This indicates that our anisotropic polymer film exhibits an excellent alignment capability

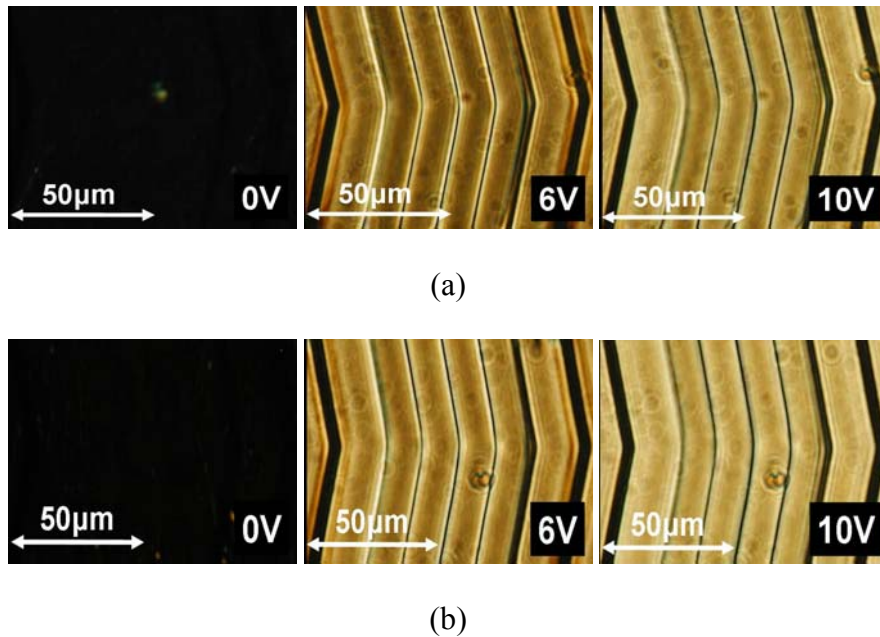


Figure 82: Microscopic photos taken from a polarizing microscope at different voltages with crossed polarizers. (a) Our anisotropic film-glass IPS cell, and (b) the conventional IPS cell. The two black zigzags in the photos are TFT source lines.

5.2.2 Experimental Setup

Figure 82 depicts the experimental set up for measuring the voltage-dependent transmittance. To measure the voltage-dependent transmittance of our cell, we placed the cells between two crossed polarizers. Our light source is a standard white light. The white light is collimated by an iris and a lens. A photodiode detector was placed behind the sample. A computer controlled LabVIEW data acquisition system was used for driving the sample and recording the light transmittance.

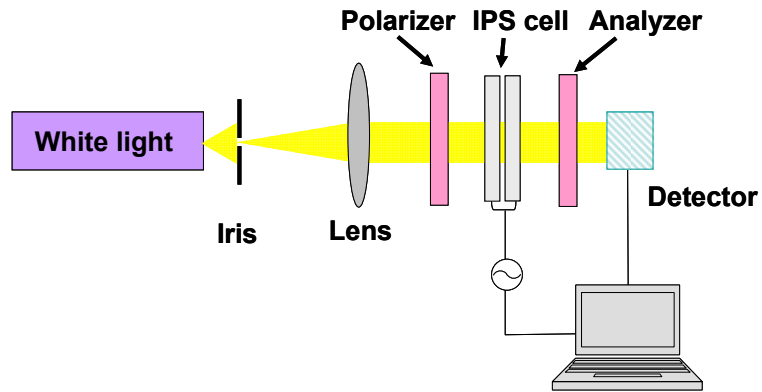


Figure 83: Experimental setup for EO properties measurement of an IPS-LCD using a glass substrate and an anisotropic polymer film.

5.2.3 Electro-optical properties

Figure 84 compares the voltage-dependent transmittance (VT) of the single-substrate IPS cell (black line) with the conventional IPS cell (gray line). To measure the VT curves, the cells were sitting between two crossed polarizers. A standard white light was used in this experiment. The transmittance of these two curves overlaps quite well. The saturation voltage is $\sim 20 V_{\text{rms}}$ for both cells. The contrast ratio (CR) is defined as the ratio of the maximum transmittance to the minimum transmittance. The contrast ratio of our single-glass-substrate IPS cell was measured to be 514:1 which is comparable to the conventional IPS cell. Our single-substrate IPS cell exhibits a much higher contrast ratio than all previously reported structures in the same category⁷⁰⁻⁷³ because the anisotropic film we developed, indeed, has a very good alignment capability.

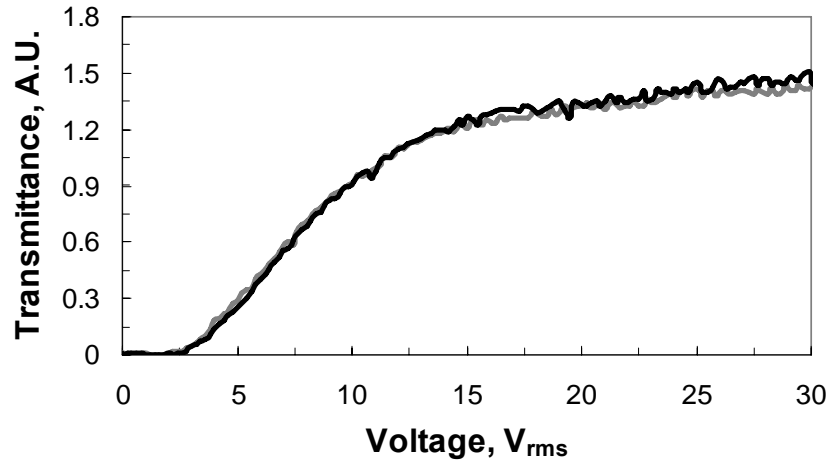


Figure 84: The voltage-dependent transmittance of our anisotropic-film-glass IPS cell (black line) and the conventional IPS cell (gray line).

5.2.4 Response Time

In addition to enhancing contrast ratio, the anisotropic film also contributes to the fast response time because of its strong anchoring energy (similar to that of the buffed PI film). We measured the rise and decay times of our single-glass-substrate IPS cell and compared results with the conventional IPS cell. Results are shown in Figure 85. At $V = 20 V_{rms}$, the measured rise time and decay time are 8 and 63 ms for our glass-film IPS cell and 7 and 69 ms for the conventional IPS cell. The comparable response times of both cells indicates that our anisotropic film has a similar anchoring strength as the buffed PI alignment layer. The observed slow decay time in both cells is due to 1) the thick LC layer ($d \sim 12 \mu m$) employed, and 2) the relatively high viscosity of the E7 LC mixture. For a practical IPS LCD, the cell gap is $\sim 5 \mu m$ and the LC viscosity is low. Under such a circumstance, the decay time should be reduced to ~ 12 ms and

voltage dropped to ~ 5 V_{rms}. It is known that E7 is not a TFT-grade LC. The reason we used E7 is simply because it is available in our laboratory.

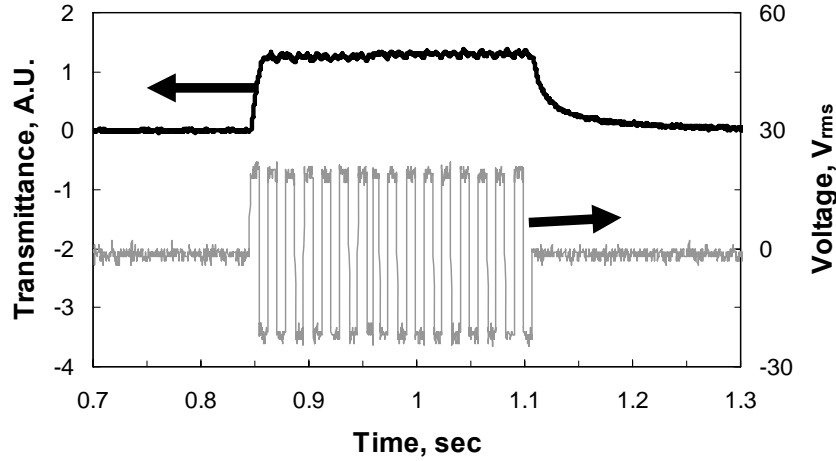


Figure 85: The measured response time of our film-glass IPS cell. The rise time is ~ 8 ms and decay time ~ 63 ms. Cell gap $d \sim 12$ μm .

5.2.5 Discussion and Conclusion

The anisotropic polymer film we fabricated has birefringence $\Delta n \sim 0.1$ at $\lambda = 633$ nm. Since the device is operated in IPS mode and the polarizer is parallel to the anisotropic direction of the film, the Δn of the film does not affect the EO properties. For a practical display, the birefringence of the anisotropic film can be an advantage for compensating the light leakage of the crossed-polarizers in the IPS mode⁷⁶. By controlling the fabrication process, such as the UV curing temperature, the polymer film can be made either anisotropic or isotropic depending on the applications. Thus, this type of film can be used as a phase compensation film besides the IPS LCD. In general, the birefringence of a LC or LC polymer decreases as the temperature increases^{48,77}. As

shown in Figure 73, the E7/RM257 mixture exhibits a nematic phase between 65.3 and 115.5 °C. Thus, within this range if the UV curing temperature increases, then the film's birefringence would decrease. If the UV curing temperature is higher than 115.5°C (the clearing temperature of LC/RM257), the polymer film would become isotropic. Moreover, the flexibility of the film can be controlled by changing the concentration of RM257. The film is more flexible as the concentration of RM257 decreases. Substrate flexibility is one of the critical issues for flexible displays.

The ambient temperature can affect the LC alignment because of the thermal expansion of the elongated polymer film. However, our LC device is operated at room temperature, so the film still has good alignment capability.

With molecular alignment capability, the anisotropic film enables other LC operation modes to be considered for display applications. For example, the twist type IPS cell can be considered by using an IPS glass substrate and our anisotropic film whose alignment direction is orthogonal to the bottom substrate. Such as an anisotropic polymer film can also be used for a double-layered guest-host (GH) display⁵ or a double-layered LC phase modulator²¹. Although some research groups⁶⁻⁸ proposed crossed-stacked GH LCD using either PI-coated glass substrate or a mylar film as a cell separator. The parallax problem is unavoidable because of the extra glass substrate. The mylar film cannot align LC molecules because its glassy temperature is lower than the baking temperature of polyimide. Without alignment, the contrast ratio is greatly sacrificed. The middle cell separator of the double-cell GH LCD can be replaced by our anisotropic polymer film which not only reduces the parallax but also increases the contrast ratio. A

tradeoff is the increased driving voltage because the polymer film shields the applied voltage.

We have demonstrated a lightweight single-glass-substrate IPS LCD using an anisotropic polymer film. The anisotropic polymer film has the comparable alignment capability to the rubbed PI film. As a result, similar contrast ratio, response time, and voltage-dependent transmittance to a conventional IPS cell employing two glass substrates are obtained. The LC molecules are aligned by the elongated polymer grains. Besides, the polymeric film is birefringent which can be also used as a phase compensation film for improving the viewing angle of the IPS LCD. Although there are some technical difficulties for making large-sized and uniform anisotropic polymer film, potential applications of such an anisotropic film for a double-layered guest-host display and flexible display are still foreseeable.

5.3 Hydrophobic Properties of Anisotropic Polymer Film

To further understand hydrophobic properties of the anisotropic polymer film, we carried out water contact angle measurements. The measurement schematic is shown in Figure 86. The fabrication process of the film is similar to previous one. After we peel off the top glass substrate, we leave one anisotropic polymer film with LC concentration 60 wt% on the top of an IPS glass substrate. The thickness of the film is around 10 μm . The IPS glass substrate was coated with a thin polyimide layer and then mechanically buffed. The electrode width is 4 μm and the electrode gap is 10 μm . A small drop of water is placed on the top of the anisotropic polymer film. When we apply large enough in-plane electric field, the surface tension of liquid-solid can be changed. A CCD camera is used to record the water contact angles which are tuned by the electric field.

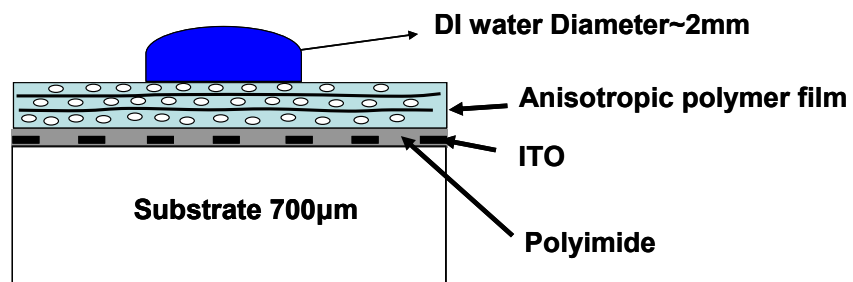
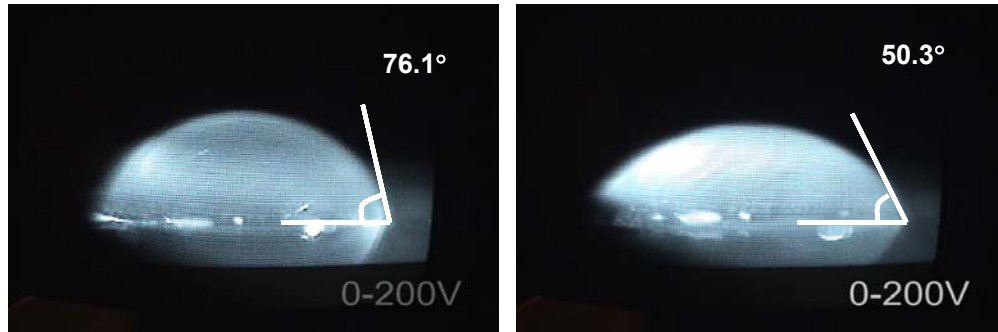


Figure 86: The structure of contact angle measurement.

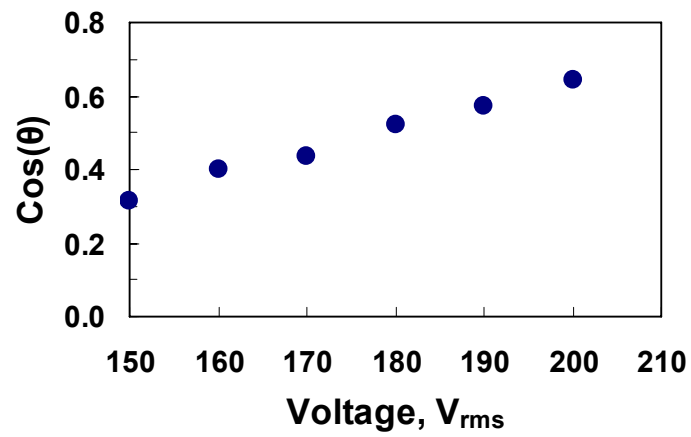
The images of the contact angle change are shown in Figure 87. We apply the square voltage bursts at $f=1$ kHz between 0 and 200 V_{rms} . The time duration is 500 ms. In Figure 87, the contact angle is 76.1 $^\circ$ at 0 V_{rms} and 50.3 $^\circ$ at 200 V_{rms} . The surface is more wetting at a higher voltage.



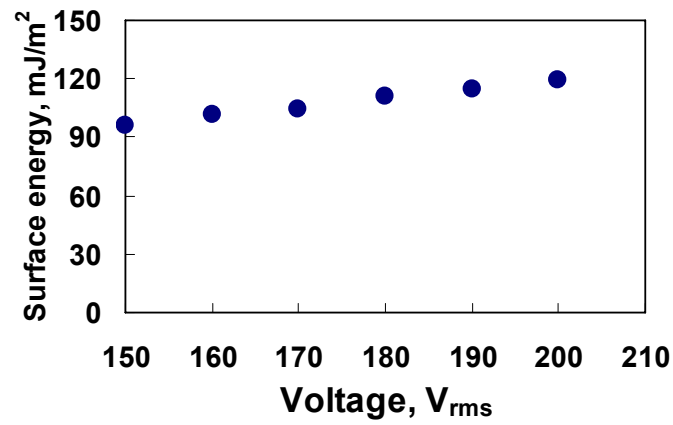
(a)

(b)

Figure 87: Contact angle measurement (a) 0 and (b) 200 V_{rms} . $f=1$ kHz. The duration between 0 and 200 V_{rms} is 500 ms.



(a)



(b)

Figure 88: (a) The cosine of contact angle as a function of applied voltage. (b) The voltage dependent surface energy.

The cosine of contact angle as a function of applied voltage is shown in Figure 88(a). The contact angle decreases as the voltage increases. That means the wetting properties is electronically controllable. The surface energy can be estimated by using Eq.(41).

$$W_{surface} = 72.8 \cdot \cos(\theta), \quad (41)$$

where θ is the contact angle. The surface energy of DI water is 72.8 mJ/m^2 . The surface energy of the anisotropic polymer film with 60 wt% LC as a function of voltage is plotted in Figure 88(b). The surface energy increases with the voltage.

The mechanism of the contact angle change is not yet well understood. The speculated mechanism is the LC directors near interface between water droplet and the anisotropic polymer film are aligned perpendicularly when the electric field is not present. The in-plane electric field reorients the LC directors near the surface of the anisotropic polymer film to align parallel to the electric field. Because it occurs at interface area, the orientation variation of LC directors near interface can not well support the water droplet. Changing the LC orientation periodically results in the variation of the hydrophobic properties and then causes a pulsed force to change the contact angle of water droplet periodically. That is why we observed the contact angle change only when we apply the square voltage bursts at certain length of duration.

5.4 Twisted Nematic Polymeric Film

We have demonstrated two applications using an anisotropic polymer film in section 4.5 and section 5.2. In this section, we use a twisted nematic (TN) polymeric film as a cell separator in order to increase the phase..

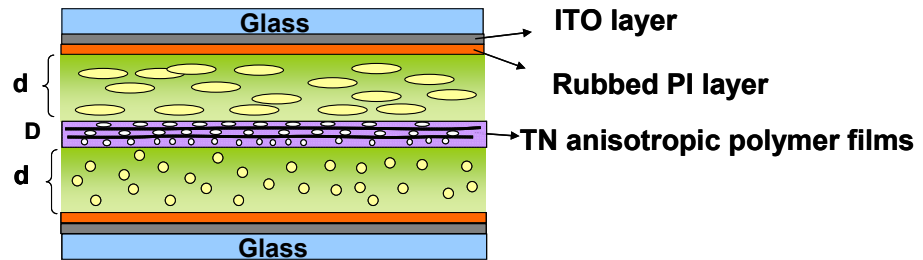
The preparation process of a TN polymeric film is similar to that of an anisotropic polymer film. The major difference is that the film is prepared using a TN cell. Hence, the TN polymeric film is similar to a TN LC cell with polarization rotation effect. The concentration of LC is ~20% and the concentration of RM257 is ~80%. We construct a double-layered LC cell with TN polymeric film as a cell separator. The directions of LC directors between the top LC layer and the bottom LC layer are orthogonal as Figure 89(a) shows. The thickness of each LC layer (d) is ~11 μm and the film thickness (D) is ~23 μm .

The voltage-dependent transmission is measured as shown in Figure 89(b). The polarizers are crossed and the optic axis of the top polarizer is parallel to the front LC rubbing direction. The experimental results show the total phase change is as large as 15π . That is because TN polymeric film not only aligns the LC directors but also rotates the polarization state of the top layer so that the total phase is accumulated. The non-zero transmission obtained in Figure 89(b) could result from misalignment between the polymer film and the pure LC layers so that the polarization rotation effect is imperfect. Another factor contributing to the baseline shift is cell and film uniformity.

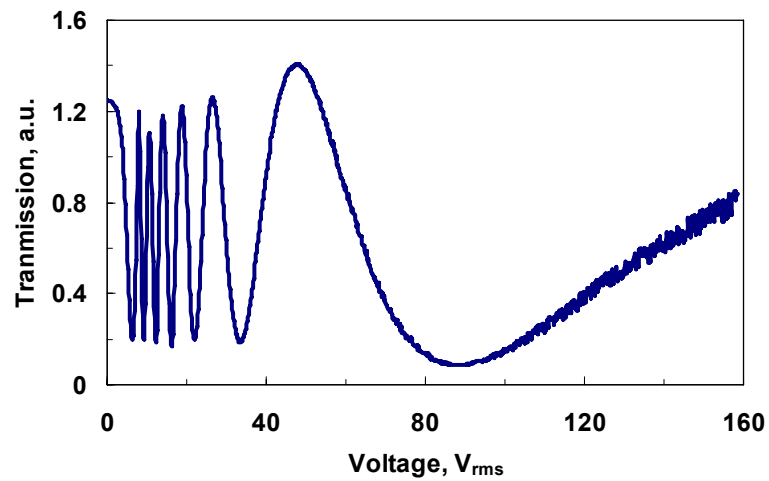
Theoretically, in an ideal condition the total phase change should be

$$\Delta\delta = \frac{2\pi}{\lambda} \cdot \Delta n \cdot 2d, \quad (42)$$

where $\lambda=633\text{nm}$, LC birefringence $\Delta n\sim 0.21$, and $d\sim 11\ \mu\text{m}$. After calculation, $\Delta\delta$ is $\sim 14.6\pi$ which is very close to the experimental result of 15π . The error may come from the imperfect alignment.



(a)



(b)

Figure 89: (a) The double layered structure using a TN anisotropic polymer film. (b) The voltage-dependent transmission. Wavelength=633nm.

In conclusion, in this chapter we have introduced the anisotropic polymer films and demonstrate their applications. Generally speaking, the anisotropic polymer film has

several advantages. It can be used as alternative substrates, an alignment layer with good alignment capability, and a compensation film. By changing the film design, the polymer film can be used as polarization rotator, such as a TN polymeric film. Potential application in photonics using the anisotropic polymer films is foreseeable.

CHAPTER 6: CONCLUSIONS

We have introduced the general principles to achieve polarization independent LC amplitude modulators and phase modulators. In chapter 3 and 4, we have demonstrated eight polarization independent LC devices.

In a T-PDLC, the scattering efficiency is better than the conventional PDLC because of the surface pinning effect. By controlling the thermal-induced phase separation process of T-PDLC, the size of LC droplets is adjustable. Therefore, T-PDLC can be used as a narrow band light shutter due to the uniform LC droplets. Moreover, the central wavelength of the scattered light is also controllable. In the dye-doped T-PDLC, several problems occur as discussed in chapter 3 resulting in a poor contrast ratio. The dye-doped DFLC gels exhibit a good contrast ratio, but the driving voltage is high and the dielectric heating effect is unavoidable. Even though the dye-doped NLC gels have a lower driving voltage and fast response, the long term stability of dye molecules could be a concern. In addition, the dye molecules seem to interact with the employed monomer. As a result, the dye's absorption band is altered.

In polarization independent LC phase modulation, the residual phase type phase modulators, such as PDLC, PSCT, have fast response, but their phase change is small and driving voltage too high. The homeotropic LC gel has a lower driving voltage and fast response; however, the phase shift is still too small for IR application. Nevertheless, the residual phase type LC phase modulators are still attractive for micro-photonics applications. The double-layered structure using a thin anisotropic polymer film as a cell

separator exhibits a large phase change, but the response time is too slow. The doubled-layered LC gels have fast response; however, the phase shift is still too small for mid-wave IR applications.

Polarizer-free LC device is an inevitable trend for all the amplitude modulators and phase modulators. We just start our first step in doing polarization independent LC devices. Besides polarization independence, color dispersion and phase difference at off-angles will be the next issues to overcome in order to achieve a broadband phase modulator with a large off-angle tolerance. Better dye materials should be developed for display applications. More new polarization independent mechanisms should be explored. This dissertation is just a beginning in the polarization independent LC devices. Finally, we expect this work can inspire more researchers to delve into this area and develop more promising approaches.

LIST OF REFERENCES

1. P. J. Collings and M. Hird, *Introduction to Liquid Crystals* (Taylor & Francis, London, 1997)
2. P. Yeh and C. Gu, *Optics of Liquid Crystal Displays* (Wiley, New York, 1999).
3. I. C. Khoo and S. T. Wu, *Optics and Nonlinear Optics of Liquid Crystals* (World Scientific, Singapore, 1993)
4. P. S. Drzaic, *Liquid Crystals Dispersions* (World Scientific, Singapore, 1995).
5. S. T. Wu and D. K. Yang: *Reflective Liquid Crystal Displays* (Wiley, New York, 2001).
6. T. Uchida, H. Seki, C. Shishido, and M. Wada, "Bright dichroic guest-host LCDs without a polarizer," *Proc. SID*, **22**, 41-46 (1981).
7. M. Hasegawa, K. Takeda, Y. Sakaguchi, J. Egelhaaf, E. Lueder, Y. Taira, and A. C. Lowe, "320-dpi 4-inch reflective stacked crossed guest-host display," *SID Symposium Digest*, **30**, 962-965 (1999).
8. M. Hasegawa, C. Hellermark, A. Nishikai, Y. Taira, and A. C. Lowe, "Reflective stacked crossed guest-host display with a planarized inner diffuser," *SID Symposium Digest*, **31**, 128-131 (2000).
9. A. Magnaldo, J. Nourry, and P. Sixou, "High memory effects in polymer dispersed chiral liquid crystal crystals with negative dielectric anisotropy," *J. Appl. Phys.* **79**, 8193-8196 (1996)
10. A. Magnaldo, J. Nourry, and P. Sixou, "Annealing and memory effects in polymer-dispersed chiral liquid crystals," *J. Appl. Phys.* **80**, 2586-2588 (1996)
11. Y. H. Lin, H. Ren and S. T. Wu, "High Contrast Polymer-Dispersed Liquid Crystal in a 90° twisted cell," *Appl. Phys. Lett.* **84**, 4083-4085 (2004).
12. Y. H. Lin, H. Ren, Y. H. Wu, X. Liang and S. T. Wu, "Pinning effect on the phase separation dynamics of thin polymer-dispersed liquid crystals," *Optics Express* **13**, 468-474 (2005).
13. Y. H. Lin, H. Ren, S. Gauza, Y. H. Wu, X. Liang, and S. T. Wu, "Reflective direct-view display using a dye-doped dual-frequency liquid crystal gel," *J. Display Technology* **1**, 230-233 (2005).

14. Y. H. Lin, H. Ren, S. Gauza, Y. H. Wu, Y. Zhou, and S. T. Wu, "High contrast and fast response polarization-independent reflective display using a dye-doped dual-frequency liquid crystal gel," *Mol. Cryst. Liq. Cryst.* (Accepted, 2006).
15. Y. H. Lin, H. Ren, Y. H. Wu, W. Y. Li, X. Liang and S. T. Wu, "High performance reflective and transmissive displays using guest-host liquid crystal gels", *SID Symposium Digest* (Accepted 2006)
16. P. F. McManamon, T. A. Dorschner, D. L. Corkum, L. J. Friedman, D. S. Hobbs, M. Holz, S. Liberman, H. Q. Nguyen, D. P. Resler, R. C. Sharp, and E. A. Watson, "Optical phased arrays technology," *Proc. IEEE* **84**, 268-298 (1996).
17. L. Vicari, *Optical Applications of Liquid Crystals* (IOP Publishing, UK, 2003)
18. H. Ren, Y. H. Lin, Y. H. Fan, and S. T. Wu, "Polarization-independent phase modulation using a polymer-dispersed liquid crystal," *Appl. Phys. Lett.* **86**, 141110 (2005).
19. Y. H. Lin, H. Ren, Y. H. Fan, Y. H. Wu, and S. T. Wu, "Polarization-independent and fast-response phase modulation using a normal-mode polymer-stabilized cholesteric texture," *J. Appl. Phys.* **98**, 043112 (2005).
20. H. Ren, Y. H. Lin, C. H. Wen, and S. T. Wu, "Polarization-independent phase modulation of a homeotropic liquid crystal gel," *Appl. Phys. Lett.* **87**, 191106 (2005).
21. Y. H. Lin, H. Ren, Y. H. Wu, Y. Zhao, J. Fang, Z. Ge and S. T. Wu, "Polarization-independent phase modulator using a thin polymer-separated double-layered structure", *Opt. Express* **13**, 8746-8752 (2005).
22. H. Ren, Y. H. Lin, and S. T. Wu, "Polarization independent phase modulators using double-layered liquid crystal gels", *Appl. Phys. Lett.* **88**, 061123 (2006).
23. E. Hecht, *Optics* (Addison Wesley, San Francisco, 2002)
24. B. E. A. Saleh and M. C. Teich, *Fundamentals of Photonics* (Wiley, New York, 1991).
25. J. L. Ferguson, US Patent 4,435,047 (1984).
26. J. W. Doane, N. A. Vaz, B. G. Wu and S. Zumer, "Field controlled light scattering from nematic microdroplets," *Appl. Phys. Lett.* **48**, 269-271 (1986).
27. N. A. Vaz, G. W. Smith and G. P. Montgomery, "A light control film composed of liquid-crystal droplets dispersed in an epoxy matrix," *Mol. Cryst. Liq. Cryst.* **146**, 17-34 (1987).
28. R. Sutherland, L.V. Natarajan, V.P. Tondiglia and T. J. Bunning, "Bragg gratings in an acrylate polymer consisting of periodic polymer-dispersed liquid crystal planes," *Chem. Mater.* **5**, 1533-1538 (1993).

29. F. Basile, F. Bloisi, L. Vicari and F. Simoni, "Optical phase shift of polymer-dispersed liquid crystals," *Phys. Rev. E*, **48**, 432-438 (1993).
30. L. Vicari, "Electro-optic phase modulation by polymer dispersed liquid crystals" *J. Appl. Phys.* **81**, 6612-6615 (1997).
31. S. Matsumoto, M. Houlibert, T. Hayashi and K. Kubodera, "Fine droplets of liquid crystals in a transparent polymer and their response to an electric field," *Appl. Phys. Lett.*, **69**, 1044-1046 (1996).
32. S. X. Cheng, R. K. Bai, Y. F. Zou, and C. Y. Pan, "Electro-optical properties of polymer dispersed liquid crystal materials," *J. Appl. Phys.*, **80**, 1991-1995 (1996).
33. H. Ren and S. T. Wu, "Inhomogeneous nanoscale polymer-dispersed liquid crystals with gradient refractive index," *Appl. Phys. Lett.* **81**, 3537-3539 (2002).
34. F. Du and S. T. Wu, "Curing temperature effects on liquid crystal gels," *Appl. Phys. Lett.* **83**, 1310 (2003).
35. B. G. Wu, J. H. Erdmann, and J. W. Doane, "Response-times and voltages for PDLC light shutters," *Liq. Cryst.* **5**, 1453-1465 (1989).
36. H. Ren and S. T. Wu, "Reflective reversed-mode polymer stabilized cholesteric texture light switches," *J. Appl. Phys.* **92**, 797-800 (2002)
37. S. T. Wu and C. S. Wu, "Mixed-mode twisted nematic liquid crystal cells for reflective displays," *Appl. Phys. Lett.* **68**, 1455-1457 (1996).
38. W. J. Chen and S. H. Chen, "Addition polymerization in a nematic medium-effects of an anisotropic solvent in a kinetic gelation model," *Phys. Rev. E* **52**, 4549-4552 (1995).
39. P. I. C. Teixeira and B. M. Mulder, "Cell dynamics model of droplet formation in polymer-dispersed liquid crystals," *Phys. Rev. E* **53**, 1805-1815 (1996).
40. D. Nwabunma, H. Chiu, and T. Kyu, "Theoretical investigation on dynamics of photopolymerization-induced phase separation and morphology development in nematic liquid crystal/polymer mixtures," *J. Chem. Phys.* **113**, 6429-6436 (2000).
41. T. Kyu and H. Chiu, "Morphology development during polymerization-induced phase separation in a polymer dispersed liquid crystals," *Polymer* **42**, 9173-9185 (2001).
42. A. Mertelj, L. Spindler, and M. Copic, "Dynamic light scattering in polymer-dispersed liquid crystals," *Phys. Rev. E* **56**, 549-553 (1997).
43. J. B. Nephew, T. C. Nihei, and S. A. Carter, "Reaction-induced phase separation dynamics: a polymer in a liquid crystal solvent," *Phys. Rev. Lett.* **80**, 3276-3279 (1998).

44. H. M. J. Boot, J. G. Kloosterboer, C. Serbutoviez, and F. J. Touwslager, "Polymerization-induced phase separation .1. Conversion-phase diagrams," *Macromolecules* **29**, 7683-7689 (1996).
45. J. Cognard, "Alignment of nematic liquid crystals and their mixtures," *Mol. Cryst. Liq. Cryst. Suppl.* **1**, 1-77 (1982).
46. Y. H. Lin, H. Ren, Y. H. Wu, X. Liang and S. T. Wu, "Surface anchoring effect on the morphology and performance of PDLC", *Proc. SPIE, "Emerging LC Technology"*, **5741**, 74-82 (2005).
47. H. Yokoyama and H. A. van Sprang, "A novel method for determining the anchoring energy function at a nematic liquid crystal-wall interface from director distortions at high fields," *J. Appl. Phys.* **57**, 4520-4526 (1985).
48. S. T. Wu, "Birefringence dispersions of liquid crystals," *Phys. Rev. A* **33**, 1270-1274 (1986)
49. Y. H. Fan, H. Ren, X. Liang, Y. H. Lin and S. T. Wu, "Dual-frequency liquid crystal gels with submillisecond response time," *Appl. Phys. Lett.*, **85** 2451-2453 (2004).
50. V. Freedericksz and V. Zolina, "Forces causing the orientation of an anisotropic liquid," *Trans. Faraday Soc.* **29**, 919-930 (1933).
51. N. Konforti, E. Marom, and S. T. Wu, "Phase-only modulation with twisted nematic liquid-crystal spatial light modulators," *Opt. Lett.* **13**, 251-253 (1988).
52. J. S. Patel , "Polarization insensitive tunable liquid-crystal etalon filter," *Appl. Phys. Lett.* **59**, 1314-1316 (1991)
53. Y. Huang, T. X. Wu, and S. T. Wu, "Simulations of liquid-crystal Fabry-Perot etalons by an improved 4x4 matrix method," *J. Appl. Phys.* **93**, , 2490-2495 (2003)
54. S. Gauza, H. Wang, C. H. Wen, S. T. Wu, A. Seed, and R. Dabrowski, "High birefringence isothiocyanato tolane liquid crystals," *Jpn. J. Appl. Phys.* **42**, 3463-3466 (2003).
55. T. J. Bunning, L. V. Natarajan, V. P. Tondiglia, G. Dougherty, and R. L. Sutherland, "Morphology of anisotropic polymer-dispersed liquid crystals and the effect of monomer functionality," *J. Polym. Sci.* **35**, 2825 (1997).
56. D. E. Lucchetta, R. Karapinar, A. Manni, and F. Simoni, "Phase-only modulation by nanosized polymer-dispersed liquid crystals," *J. Appl. Phys.* **91**, 6060-6065 (2002).
57. R. L. Sutherland, V. P. Tondiglia, L. V. Natarajan, T. J. Bunning, and W. W. Adams, "Electrically switchable volume gratings in polymer-dispersed liquid crystals," *Appl. Phys. Lett.* **64**, 1074-1076 (1994).
58. S. T. Wu, U. Efron, and L. D. Hess, "Birefringence measurements of liquid crystals," *Appl. Opt.* **23**, 3911-3915 (1984).

59. H. Ren, Y. H. Fan, S. T. Wu, "Liquid-crystal microlens arrays using patterned polymer networks," *Opt. Lett.* **29**, 1608-1610 (2004).
60. D. K. Yang, L. C. Chien and Y. K. Fung, *Liquid Crystals in Complex Geometries Formed by Polymer and Porous Networks* (Taylor & Francis, London, 1996).
61. D. K. Yang, L. C. Chien and J. W. Doane, "Cholesteric liquid crystal/polymer dispersion for haze-free light shutters," *Appl. Phys. Lett.* **60**, 3102-3104 (1992).
62. J. L. West, R. B. Akins, J. Francl and J. W. Doane, "Cholesteric/polymer dispersed light shutters," *Appl. Phys. Lett.* **63**, 1471-1473 (1993).
63. I. Dierking, L. L. Kosbar, A. Afzali-Ardakani, A. C. Lowe and G. A. Held, "Two-stage switching behavior of polymer stabilized cholesteric textures," *J. Appl. Phys.* **81**, 3007-3014 (1997).
64. I. Dierking, L. L. Kosbar, A. C. Lowe and G. A. Held, "Polymer network structure and electro-optic performance of polymer stabilized cholesteric textures - I. The influence of curing temperature," *Liq. Cryst.* **24**, 387-395 (1998).
65. I. Dierking, L. L. Kosbar, A. C. Lowe and G. A. Held, "Polymer network structure and electro-optic performance of polymer stabilized cholesteric textures - II. The effect of UV curing conditions" *Liq. Cryst.* **24**, 397-406 (1998).
66. R. A. M. Hikmet, "Electrically induced light scattering from anisotropic gels with negative dielectric anisotropy," *Mol. Cryst. Liq. Cryst.* **213**, 117-118(1992).
67. C. H. Wen, S. Gauza, J. Li, H. Wang, and S. T. Wu, "High-contrast homeotropic alignment of difluoro-tolane liquid crystals," *Liq. Cryst.* **32**, 643-649 (2005).
68. B. Bahadur, *Liquid Crystals Applications and Uses*, (World Scientific, Singapore, 1992), Vol. 3, Chap. 11.
69. Y. H. Lin, H. Ren, S. Gauza, Y. H. Wu, and S. T. Wu, "Single-substrate IPS-LCD using an anisotropic polymer film," *Proc. SPIE*, **5936**, 59360O (2005).
70. R. Penterman, S. I. Klink, H. D. Koning, G. Nisato and D. J. Broer, "Single-substrate liquid crystal displays by photo-enforced stratification", *Nature* **417**, 55-58 (2002).
71. P. Raynes, "Liquid crystal painting", *Nature* **417**, 28-29 (2002).
72. J. P.A. Vogels, S. I. Klink, R. Penterman, H. D. Koning, E. E. A. Huitema and D. J. Broer, "Robust flexible LCDs with paintable technology", *Soc. Inform. Display Tech. Digest*, **35**, 767-769,(2004).
73. Il Kim, J. H. Kim, D. Kang, D. M. Agra-Kooijman and S. Kumar, "Fabrication of electro-optic devices using liquid crystals with a single glass substrate", *J. Appl. Phys.* **92**, 7699-7701 (2002)

74. H. Sato, H. Fujikake, H. Kikuchi, Y. Iino, M. Kawakita and Y. Tsuchiya, "Fluorinated polymer alignment layers formed at low temperature for plastic-substrate based liquid crystal devices", *Jpn. J. Appl. Phys.* **40**, L53-L55 (2001).
75. T. Murashige, H. Fujikake, S. Ikehata and F. Sato, "Anchoring strength of thin aligned-polymer films formed by liquid crystalline monomer" *Jpn. J. Appl. Phys.* **42**, 1614-1617 (2003).
76. R. Lu, X. Zhu, Q. Hong, and S. T. Wu, "Ultrawide-view liquid crystal displays," *J. Display Technol.* **1**, 1-14 (2005).
77. J. Li, C. H. Wen, S. Gauza, R. Lu, and S. T. Wu, "Refractive indices of liquid crystals for display applications," *J. Display Technol.* **1**, 51-61 (2005).